Universitá "Federico II" - Napoli

Dottorato
in Fisica Fondamentale e Applicata

PhD Thesis

Defended by

Eugenio SCHISANO

Characterizing circumstellar disks around young stars

Thesis Advisor: Luigi SMALDONE

prepared at Ossevatorio Astronomico di Capodimonte

Supervisors :   Luigi SMALDONE   -   Universitá "Federico II"
               Juan Manuel ALCALÁ   -   OAC - INAF
               Elvira COVINO   -   OAC - INAF

Abstract

The circumstellar disks play a fundamental role in star and planet formation process. Studies on circumstellar disks are generally carried on following two viable approaches: Òstatistical Ó studies, where a large samples of sources are measured to determine mean disk common properties, detailed study on individual objects can shed the light on processes, like mass accretion, central star irradiation or photoevaporation, that compete in defining the shape and the lifetime of the disks, improving the theoretical models or, hopefully, to directly catch a planet in the process of forming. Although both approaches converge toward a general scenario, they are sensitive only the disk dust component, while recently there is a strong interest on the gas, since it constitutes most of the mass of the circumstellar disks, determining the dust dynamic and the settling process, and its dispersal timescales limit the formation of gas giant planets.

In this work I present a synoptic study carried on the young stellar object T Cha, belonging to the class of "transition" disks, peculiar systems where very rapid evolution is ongoing. Such transitional disks are rare and, due to their classification based on the shape of the spectral energy distribution, do not represent an homogeneous class. For such reasons the characterization of any further object is extremely important to understand if we are dealing with a planetary system in formation.

On the other side, I carried on a systematic study on recent discovered diagnostic for the gaseous disk component. The fine structure infrared emission line of [Ne II] at 12.8 μm has been discovered in more than ~ 70 object. This line is thought to be produced by X-ray irradiation of the warm protoplanetary disk atmospheres, however the observational correlation between [Ne II] luminosities and measured X-ray luminosities shows a large scatter. Such spread limits the utility of this line as a probe of the gaseous phase of disks, as several authors have suggested pollution by outflows as a probable cause of the observed scatter. For the first time with this work it has been explored the possibility that the large variations in the observed [Ne II] luminosity may be caused instead by different star-disk parameters.

Contents

Chapter 1

Introduction

The mid-20th century advances in the theoretical and observational fields connected to the astronomy have led to a description of how the stars and the planets form. The accepted paradigma is that planets form in circumstellar disks[1] composed by small dust particles and and gas, leftover of the process of star formation. The planet formation is almost concomitant to the star formation and the circumstellar disk plays a fundamental role for both cases. Hence, they have become the subject of much study since their prediction and discovery.

The circumstellar disks around young stars have been observed by the direct imaging of their later evolutionary phases. There is overwhelming observational evidence that young circumstellar disks exist. Optical/infrared imaging of the scatter light and the thermal emission from disks has been obtained by HST (Grady et al., 2001; Schneider et al., 1999, 2004) and ground observation with adaptive optic (Close et al., 1998; Menard et al., 1999). Interferometric studies have also revealed their resolved structures around plenty of systems (Akeson et al., 2000; Tuthill et al., 2001). Such observations have contributed to draw the basic scheme where the disk acts as a mean to channel the matter from the infalling envelope to the central object and as a huge reserve of raw material where planets can form. Despite this, the physical properties of the disks are often not well determined due detection limits, selection effects and uncertains in the modelling. Moreover, it is still poorly constrained the disk influence on the young star, the details of disk evolution, including the relevant timescales. If, where and how planets form within the disk strickly depends on how the disk are.

This work focus on the disks and their role in the star/planet formation, aiming to contribute to such wide field in diffent way. For one side I carry new

---

[1]Often shortened to disk in the text. In this work whenever is found the term disk it is implied a circumstellar disk around a young star

observational evidence on a critical evolutionary phase, where, as explained
in the following, rapid changes set up in the disk. The fast timescales of
such changes implies that few systems are observed in "transition", then any
study characterizing a new discovered object in such phase is fundamental to
understand how disk evolves. In chapter 2 I descrive my work on one of such
systems, focused on the study, too often understimated, of its variability.
On the otherside, progress in techniques gives access to a pletora of new ob-
servational tools able to probe the dynamic, the chemistry and the structure
of the disk. In such field, huge advances have been accomplished by the
observations of several atomic lines emitted by the disk. Nevertheless, to be
successfully used as probe of physical properties of the disks, it is needed to
fully understand how and where they forms. Such work is still in progress
in the case of the mid-infrared fine structure lines observed by the recent
Spitzer space mission. In chapter 3 I report the theoretical work I have
perfomed to characterize the neon atomic lines as useful diagnostic. In the
following I briefly introduce more in detail to the topic of circumstellar disk
in the framework of the star and planet formation.

1.1   The star and planet formation sequence

The accepted star formation scenario is shown schematically in Figure 1.1.
The cold (T$\sim$ 10-20 K) interstellar matter organizes itself on large scale
structures (from few 10 up to few 100 of pc with masses $\geq 10^4$-10^5 M$_\odot$)
into clouds, sheets and filaments. Such structures can become gravitational
unstable on smaller scales ($\leq 0.1 - 1\,\mathrm{pc}$), triggering a free-fall collapse of
matter and leading, on relatively short timescales ($10^5\,\mathrm{yr}$) to the formation of
an hydrostatic protostar surrounded by an infalling envelope. However, any
initial angular momentum hold by the matter (typically $\Omega \sim 10^{-13}\,\mathrm{s}^{-1}$) can
not be dissipated to the external enviroment, hence, the infalling material
form a centrifugally supported circumstellar disk around the young protostar
(sizes $\sim 1000\,\mathrm{AU}$ and masses up to $\sim$ few 10 of M$_\odot$). The matter infalls on
the circumstellar disk and, from there, it is accreted on the central protostar.
During such collapse the central object is heavily obscured (A$_V \geq 10^3\,\mathrm{mag}$)
to become visible at near-infrared and optical wavelengths when most of its
final mass is already accreted on the protostar.
The system, then, evolves through the final stages of infall and disk accretion,
while the pre-main sequence star contracts on Kelvin-Helmotz timescales
(lasting $\sim 10^7$ yr for a low mass star) until the triggering of hydrogen burning
in its center. In such later phase the disk inward accretion and the outflows
along the magnetic axis affects either the mass and the angular momentum
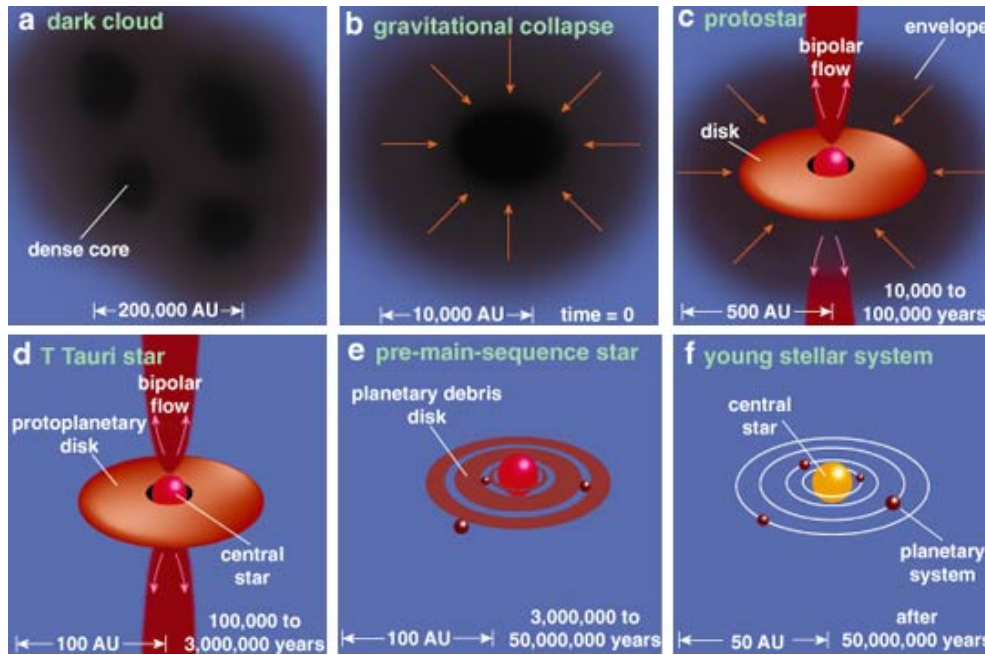
Figure 1.1: A schematic diagram of the principal stages of the star (and planet) formation. Figure from Greene (2001).

of the forming star and the amount of material left in the disk. The disk in such middle stages, surrounding T-Tauri (low-mass, of the order of solar mass) or Herbig Ae/Be (mid-mass, in the range of 3-8 $M_\odot$) stars, are the targets of this work. Any planet formation activity is believed to take place during these stages, once the accretion is reduced.

Indipendently from the eventual formation of a planet, the accretion onto the central star and the sweeping by the star radiation field or wind lead to the dissipation of the disk. Observations suggest disk lifetimes of the order of $10^6 - 10^7$ yr. Leftover of these primordial disk are the so called debris disk, generally very low-massive (≤ 0.01 $M_\oplus$) gas poor ($\leq 10\%$) and composed by second generation dust produced by planetesimal collisions.

The descrived evolutionary phases are linked to different observational classes (Lada, 1987), generally identified by the shape of their spectral energy distribution (SED). Such classification scheme divides the objects in four classes, from 0 to III, from younger objects to more evolved one. A scheme of the infrared classification generally adoped is reported in Figure 1.2.

So far, the analysis of the SED is the strongest diagnostic to determine the evolutionary stage of an object. In this work I am focusing on disk around Class II-III objects, or as expressed before the T-Tauri/Herbig Ae/Be stars.

Despite the recent increase of observations at high spatial resolution able to solve the structure of the disk, much of our knowledge is still derived from SED modelling.

1.2   Circumstellar disks structure

Circumstellar disks are composed by dust and gas in orbits around the central object[2]. Kinematic models of the spatial resolved CO emission suggest Keplerian rotation (Mannings et al., 1997). It is worth noticing that the measured emission at wavelengths $\geq 1\mu$m is due manly to the reemission of the dust in thermal equilibrium, while at shorter wavelengths a substantial contribution is given by the scattering of the stellar light by dust grains. Hence, different wavelengths probe different location of the disk, due to radial and vertical temperature gradients, as shown in Figure 1.3. For example, the disk inner regions very close to the star ($\sim 0.1\,$AU) are hot enough ($\sim$1000-1500 K) to emit mostly in the near infrared ($\sim 1\mu$m), while disk radii 1-5 AU corresponds to mid-infrared emission ($\sim 10 - 100\mu$m).

Global disk properties can be inferred then from the modelling of the SED, but the results are strongly model dependent and there is usually no unique solution. The models represent the density and temperature steady state solutions to the dynamical and radiative transfer equations, sometimes parametrized by analytical approximations. Time dependent models are possible in few simplified cases, but they are computational intensive and often oversimply the problem to make it tractable (Fromang et al., 2004; Yorke and Bodenheimer, 1999).
The shape of the SED basically depends from the temperature stratification setted by the heating processes active within the disk. For dusty disk the heating is given or by the incident stellar light from the central object (*passive* heating) (Hartmann et al., 1998) or by the viscous dissipation of the accretion process active within the disk (*active* heating) (D'Alessio et al., 1998; Pringle, 1981). Both models do not predict any vertical motion, as consequence the disk, in hydrostatic equilibrium, is geometrically thin with its scaleheigh much smaller than the size ($H \ll R$). Observations confirm the existence of such flat structure, however, many objects required a flaring geometry for the disk surface (Kenyon and Hartmann, 1987) (as shown in Figure 1.3) to be compatible with their strong far-infrared emission shallow SED slopes). The impinging stellar radiation produce a warm dust surface

---

[2]In this paragraph I restrict the description to dust component of the disk. I report a detailed discussion on the gaseous component in the chapter 3.
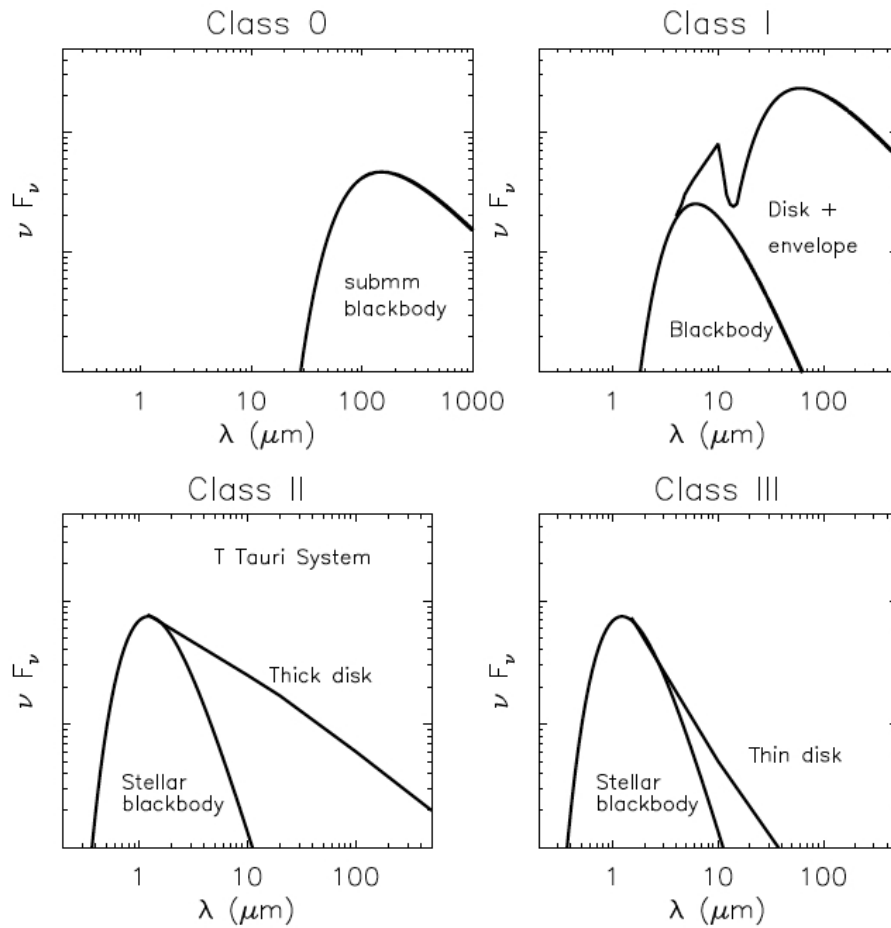
Figure 1.2: Lada infrared classes linked to the stages of the star formation. The upper left panel represent the typical SED of a young protostar. Evolving the object, the stronger contribution to the emission shift towards shorter wavelengths.
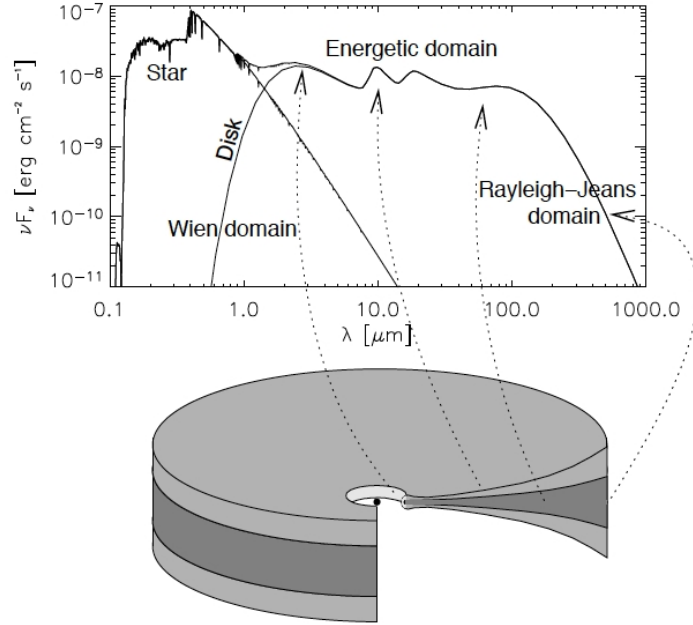
Figure 1.3: Contribution to the SED from various component of the protoplanetary disk. Near infrared emission comes from the inner rim, mid infrared dust feature from the warm surface layer and the overall continuum emission from the cold midplane. Typically the shorter wavelength emission comes from the small radii, while the far infrared from outer regions. Submillimeter emision comes from the whole disk (dust optically thin at those wavelength). Figure from Dullemond et al. (2007).

layer, a sort of disk atmosphere, then forms above the midplane where the disk is optically thick to the radiation (Chiang and Goldreich, 1997). Dust grains in such region are hotter than the one residing inside the disk, with temperature difference typically of a factor of $2-4$ for weakly accreting disks[3].

Finally the dusty disks do not extend until the star surface, as it was stated in early models (Lynden-Bell and Pringle, 1974), but they have a

---

[3]In the case of accreting disks, the viscous dissipation heats the disk interior, so the temperature minima is between the hot layer and the midplane. However, since it is know in detail how the accretion works (see chapter 3), it could be possible that the deep interior, into the so called "dead zone" where accretion is not acting, is still at very low temperature.
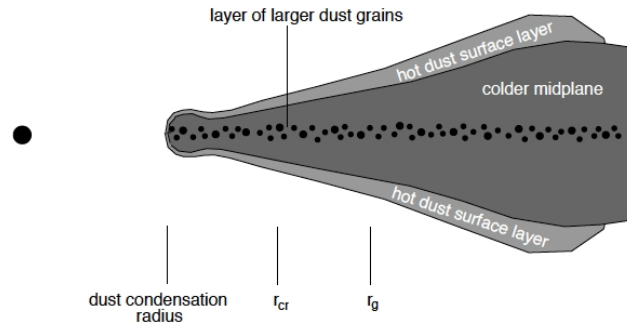
Figure 1.4: Rappresentation of the main structures of a typical dusty disk. An hot layer (T *leq* 1000 K) is overimposed to a cold interior (T10 − −100 K where most of the matter reside. The puffed inner rim is present at the dust destruction radius ($T_{dust} \sim 1100 − 1800$ K). Image from Dullemond et al. (2007).

relative abrupt inner edge (called "rim") at ∼ 0.01 AU for a 1 $L_\odot$ star (and scaling roughtly with $L_\star^2$, where the dust reach its sublimation temperature, T_{dust}. Gas can still be present inside the rim and influence the amount of radiation heating it. Despite this, the radiation hits the inner rim to a high inclination angle, hence dust is hotter (T∼1500 K) than the rest of the disk irradiated to a much shallower angle. Due to the high temperature the rim is believed to be puffed-up (Dullemond et al., 2001; Natta et al., 2001), with rounded shape due to the dependence of T_{dust} from the density (Isella et al., 2006).

1.3 The disk evolution

A shallow analysis of a sample of young stars reveals that not all objects show the descrived excess emission typical from a dusty disk. Only half of the young star population with age ∼ 1 Myr exhibt optically thick emission and it decrease to around 10% for 10 Myr stars. Figure 1.5 shows the fraction of objects with a near-infrared excess infrared emission, thus hosting a circum-stellar disk, in function of the age of the stellar group, indicating that inner disks disappear after a timescale 1 − 10 Myr. Such effect obviously reflects
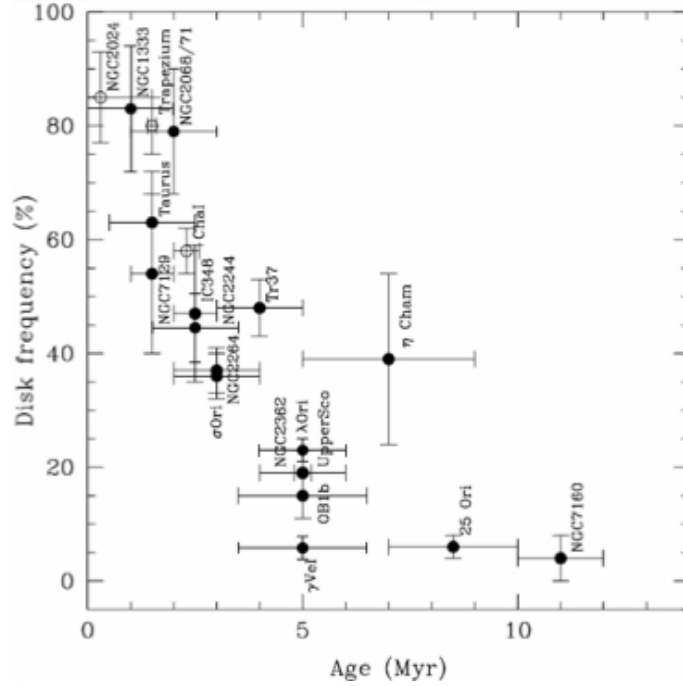
Figure 1.5: Fraction of disk hosting star in the star forming cluster in function of its age. It is clear the steady decline. Image from Haisch et al. (2001).

on the SED shape, so it is expected an evolutionary sequence (like the one of figure 1.1. In a relatively young region ~ 3 Myr it has been found (from the analysis of the SED slope between $3-8$ μm) that most of the objects exhibt excess compatible with an optically thick flared disk, with few objects with weak excess, and a large population of objects compatible with stellar photo-sphere (Hernández et al., 2007). Of the objects with weak excess in the near infrared, some are still compatible with optically thick disk, but with flat geometry, but few others show a strong emission at longer wavelength (the so called transition disks see below). The relative fraction of such systems reveal that the timescale for the inner disk dissipation is short, of the order of few 10^5 yr (Wolk et al., 1996). If the only the accretion of the dusty and gaseous material onto the central star is involved in the disk evolution, their changes would be slow on time ($\mathrm{M}_{disk} \propto t^{-\frac{1}{2}}$ for typical viscosity) (Hartmann, 2009). Hence, two timescales should exists: a slow decline of accretion with a rapid clearing.

But if the circumstellar disks is not dispersed by accretion, how the mate-rial is depleted ? The enviroment where the young star should not be ignored; disks can be disrupted by the tidal action of one or more companion, even

by massive protoplanets. High massive stars in the proximity also accelerate the evolution. However, other mechanisms have been proposed to explain the disk dissipation, and mostly the two-timescale problems. Between those, the most promising are the sweeping of the material from the high-energetic radiation field produced by the star (photoevaporation) (Alexander and Armitage, 2007; Clarke et al., 2001; Hollenbach et al., 2000) and the dust sedimentation toward the midplane, flattering the disk and growing up in size by collision up to rocky planetesimals. Thus, the reduction of the dust opacity justifies the less excess emission in the infrared. Last but not least the formation of a massive planet within the disk can open a gap at its orbital radius, Hence the planet will act as the combined effect of a dam for the inner regions, dragged out by the accretion, and a sink, due to the accretion on itself. Gaps opened by planets are no more wide than two three times the radius, however they show a precise SED shape (see also sec 1.4.2).

1.4 Dust Evolution: Mechanisms of planet formation

Dust grains in the disk are believed to evolve toward larger size, with small grain abundances decreasin with time. During its growth the dust settle vertically and drift radial. Such smooth evolution of dust in sizes and positions can reduce and in the end eliminate the infrared excess. Furlan et al. (2005) founded that to fit mid infrared spectra it is required a significant amount of dust settling, with depletion of the order of 10^{-2}-10^{-3} from the interstellar value. Vague indications of disk flattering with the increasing age come from Hernández et al. (2007), however data are still uncertain.

What about planets? The discovery of hundreds of extrasolar planets around the main sequence stars suggests that the formation of planets is not a rare process. Nevertheless how it happens and its timescales are still under debate (for a extensive review on this topic see Armitage (2009)). Two basic theories of planet formation[4] are widely accepted : the core accretion (Bo-

---

[4]Strictly true for giant gaseous planets. Terrestrial planets are formed by the agglomeration of dust to form planetesimal. Such objects grown further through direct collision triggering a runaway growth. The largest bodies become enough massive to stir up their near planetesimal, isolating itself from the surrounding and forming the protoplanetary cores that will evolve in the planets. Most of the uncertains are due to the formation of planetesimal. Actual theories could not predict the coagulation of the dust from mm-size to m one objects with timescales compatible with the disk lifetime and the dust drift into

denheimer and Pollack, 1986; Pollack et al., 1996) and the disk instability model (Boss, 1998). In the first case, similar to the terrestrial planet formation, dust settles toward the midplane of the disk, sticking into larger grain at start slowly and then extremely fast with a runaway process (timescales 1-10 Myr). Gas is then accumulated, eventually building up a thick atmosphere (timescales of 10-100 Myr). In the gravitational instability model, by contrast, the disk become unstable, collapse and directly form a massive planets. Even if there are strong indication most of the detected planets formed by core-accretion processes (Matsuo et al., 2007), gravitational instability can not be completely ruled out, mostly due to the lack of clear definition for the disk properties, still biased by detection limits and selection effects. In the framework of the same model the occurrence of the planet formation depends on the disk structure, in particular on its surface density. Thus, to further progress on the the planet formation is fundamental to explore how the disk are.

1.4.1   Photoevaporation

The term ÒphotoevaporationÓ refers to mass-loss from a circumstellar disc due to radiative heating of the disc material, either from the central star or by an external heat source. Such process triggers when the thermal energy of the ionized gas is larger than its gravitational potential energy, hence the ionized gas is free to flow away from the disk surface as a thermal driven disc wind. The radii at which such wind can set up depends on the sound velocity speed c_s in the disk as:

$$\frac{R_g \sim GM_\star}{c_s^2} \tag{1.1}$$

However, it has been shown that even inside the gravitational radius, at distance $\sim 0.1 R_g$ there could be an intense photoevaporative flow. To be effective, the flowing gas has to have a temperature of ? 10^4 K, much higher than the typical temperature of a star irradiated or accretion disk.

But in presence of an high-energy radiation field, composed by EUV and X-rays, the gas in the upper disk atmosphere has an high probabilty to reach such temperature[5]. More energetic field are generally more penetrative, thus reach higher density regions. Since the mass flux rate of the photoevaporative flow depends on the density at the base of the flow, it is expected that energetic photons are more effective for the disk dispersal.

---

the central star.

[5]See also chapter 3
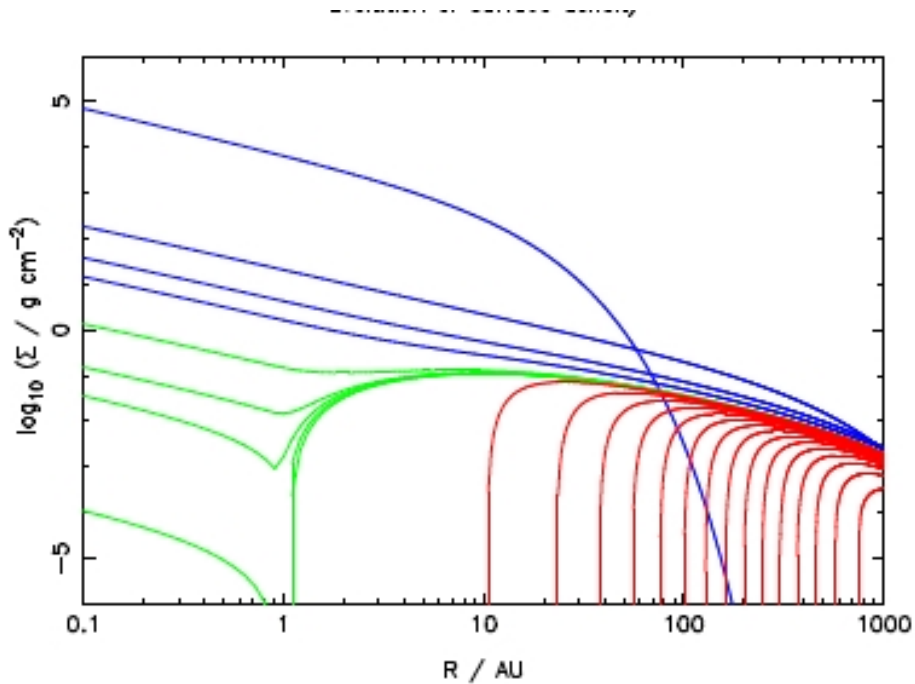
Figure 1.6: Evolution of the surface density for a typical accretion disk irradiated by an EUV photon flux, $\Phi \sim 10^{41}$. Three distint stages are identified by different color. In blue the early stages until 6 Myr with the slowly accreting evolution. In yellow the inner regions of the disk drop in density on a timescale of $\sim$ few 10^4 yrs, then in red in $\sim 10^5$ the inner region is rapidly evacuated.

However, this is still an highly debated issue (Ercolano et al., 2009; Gorti and Hollenbach, 2009).

The strong point of the photoevaporation is that it easily explains the two-timescale problem of the disk evolution. Detailed calculation conducted by Alexander et al. (2006) indicate that it triggers only once the accretion has dropped out to $\sim M_\odot^{-9}$ yr. However once setted it is extremely effective in the dispersal of the disk as shown in figure 1.6.

1.4.2 Transition disks

Transition disks are young system showing indeed a deficit of flux in near/mid infrared that suggest the lack of dust near the star. At the same time the far-IR fluxes are still intense, compatible with the typical emission
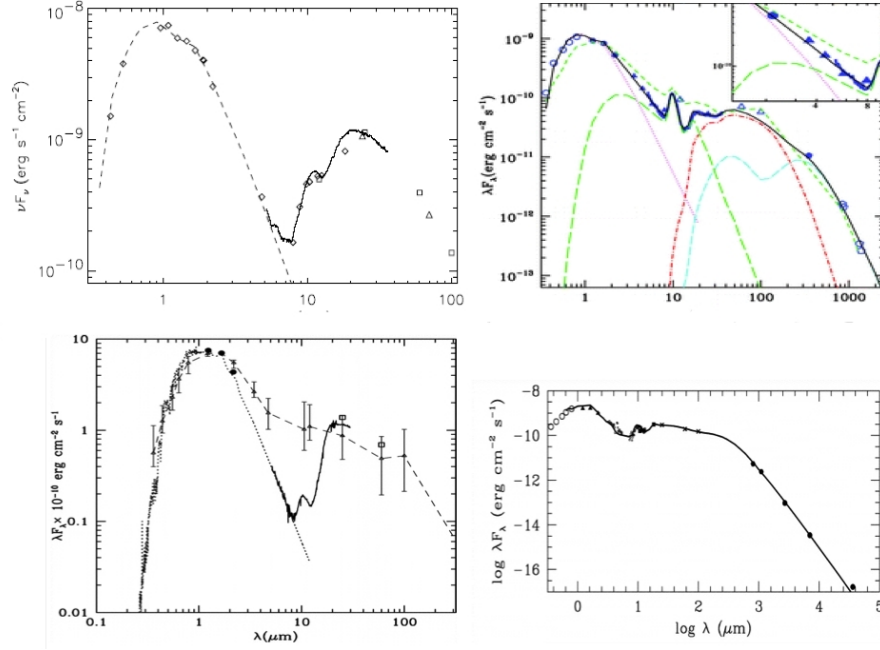
Figure 1.7: SED of transitional disks. Even if the observational features are similar in all the displayed objects, different causes produces the lack of dust in the inner regions. Upper left, the case of HD98800 (Furlan et al., 2007) appears to be a tidal truncated disk, LkCa15 in the upper right is a gap opened disk with signature of gas (Espaillat et al., 2007). In the lower left, once adopted as progenitor of the class CoKu Tau/4 revealed only recently its real nature of a circumbinary disk (Ireland and Kraus, 2008). In the lower right is show the best studied transition disk so TW Hya

of class II objects, indicating that the outer disk is still massive (Najita et al., 2007b). These disks are though to be in a transitional phase between the classical circumstellar disks and relic debris disks. The transitional disks are widely considered as the best candidates to be planet-forming systems.

While ideally with the definition of transitional disk one would identify systems with an evolutionary characteristic, they are characterized by a SED particular shape (see figure 1.7. The lack of emission at near/mid infrared wavelengths means that the disk material has been removed from the inner region, but the simple SED analysis do not determine what is the cause did it. The photoevaporative flows at example has the effect to open a gap in the disk and the inner disk not refunded anymore from the outer material is simply accreted into the star (Alexander and Armitage, 2007). Despite

this the presence of a substantial outer disk with weak inner dust emission suggests that at least a portion of the transitional disk sample represent an early stage of clearing.

However, the presence of a stellar companion, even within the disk, also produce a dynamical clearing of the regions closest to the star citepCalvet:2002we, Ireland:2008ch Few objects shows that a significant quantity of gas (like in the case of TW Hya, Najita et al. (2003)) and dust (like in the case LkCa 15 Espaillat et al. (2008) is still present in the inner region. There are plenty observation proof that transition disks do not represent an homogeneous class in term of physical properties, but they show a whole range of other parameters. Just as example, the accretion rate goes from undetectable (in the case of CoKu Tau/4) to like one of a classical T-Tauri (in the case of GM Aur), as well as disk masses being small disk, $M_{disk} \sim 10^{-4}\,\mathrm{M_\odot}$ (CoKu Tau/4) up to $10^{-2}\,\mathrm{M_\odot}$ (DM Tau). Even if the variety of transitional disks reflects varied physical processes active or stages of evolution, their characterization is still fundamental to shred light on the disk evolution, in attempt to find system where planets are actually forming or at the early stages of their evolution.

Chapter 2

Variability of the T Chamaelontis transitional disk

In order to understand how stars and planets forms it is necessary to perform studies on individual objects as well as statistical estimate of the global properties and the evolutionary trends on samples of young stellar objects. However, when one wants to focus on the fast evolving phases, the samples are still extremely limited. This is the case for the case of the transitional disks, whose dispersion act on scales of 10^5 yr. As more data is being acquired with mid/far infrared surveys, the number of transitional disk is slowly increasing, but, so far, only few tens of objects are well identified. Even if preliminary statistical analysis can be carried on, detailed studies of single objects are still strictly necessary to characterize the transition disk phase. For example, the deep study of CoKu Tau/4, previously identify as a typical transitional disk-like object for the appearance of the spectral energy distribution, revealed that the system is a circumbinary disk (Ireland and Kraus, 2008). Hence, the contaminations of the transitional disk class by such objects can prevent the drawing of robust conclusions. Unfortunately only few transitional disks were object of detailed studies.

In this chapter I am descriving the study of the transitional disk T Chamaelontis (hereafter T Cha), focusing in particular on its photometric and spectroscopic varialibity. Such chapter with minimal differences was published on E. Schisano, E. Covino, J. M. Alcalá, M. Esposito and others, *Astronomy & Astrophysics*, Volume 501, Issue 3, 2009, pp.1013.

2.1   Introduction

T Tauri stars (TTS) are low-mass (M≤2 M$_\odot$) pre-main sequence (PMS) stars (Appenzeller and Mundt, 1989). They are commonly classified into two sub-groups, the classical TTS (cTTSs), which are surrounded by an optically thick disc from which they accrete material, and the weak TTS (wTTSs), presumably representing the final stages of accretion and disc-clearing processes (Bertout et al., 2007). Hence, the cTTS-wTTS dichotomy is ascribed to different physical processes associated with the evolution of these young solar-type stars and their circumstellar environment. The equivalent width of the Hα emission is commonly used as an empirical criterion to distinguish between cTTS and wTTS (White and Basri, 2003). However, due to possible variability, no clean distinction can be made between the two subgroups based on the Hα emission alone.

Besides the traditional cTTS versus wTTS scheme, Herbst et al. (1994) introduced an additional class, the early-type T Tauri stars (eTTSs), from simple analysis of the photometric variability. ETTSs are earlier than K0 and have large-amplitude irregular variations (up to $\sim$3 mag in V) with no sign of continuum veiling. Within this class, those authors also included some Herbig Ae/Be stars (HAEBEs) of the UX Ori type (Herbst and Shevchenko, 1999). Studying this kind of variability along with stellar mass, Bertout (2000) concluded that T Tauri stars can display a similar phenomenology. Well-studied cases such as RY Lup (Gahm et al., 1989) and AA Tau (Bouvier et al., 2003) support this hypothesis.

How can all these observations be interpreted coherently in a scenario of star and circumstellar environment evolution is still questioned. Grinin (1988) modelled this kind of variability with dusty clumps in Keplerian orbits that temporarily obscure the central star. The rapid temporal evolution of such events indicates that the dust clouds usually appear in the disc close to the dust sublimation radius, probably in the inner rim region (Dullemond et al., 2003; Natta et al., 2001). This model implies a high inclination angle, while imaging and near-infrared interferometry of some of those stars are inconsistent with it (see the review by Millan-Gabet et al., 2007, and references therein). Another scenario was proposed by Vinković and Jurkić (2007), in which a dusty outflow creates a halo in the inner-disc region, where clumps of dust occasionally intercept the line of sight and mask the stellar photosphere.

T Tauri discs evolve on a timescale of a few million years and the circumstellar raw material from which planets are constructed is affected different processes. In the inner part of the disc ($\lesssim$10 AU), the gas is accreted onto the star or expelled by bipolar jets, while the outer part of the disc may be dissipated by photoevaporation (Alexander and Armitage, 2007; Clarke

et al., 2001). On the other hand, dust grains settle in the midplane, grow in size, and form planetesimals (Dullemond and Dominik, 2005; Sicilia-Aguilar et al., 2007). As the disc becomes progressively optically thin, solid particles migrate inward or outward, depending on their size, due to the combined action of different perturbing forces (photophoresis, gravity, radiation pressure, and gas drag), until they reach a stability distance from the star. It remains unclear how planetesimals are formed in circumstellar discs and whether the hypothetical dusty clumps in highly variable TTS are related or not to the evolution of circumstellar dust until the formation of planetesimals. Detailed studies of the observed properties of objects with intermediate characteristics, in-between those of cTTS and wTTS, are expected to provide key constraints on star and planet formation scenarios.

Observations in the infrared (IR) with the Spitzer satellite have provided a wealth of information for interpretating the spectral energy distribution (SED) of young stars (see Cieza et al., 2007; II et al., 2009; Lada et al., 2006, and references therein), allowing the development of new classification schemes and scenarios of disc evolution (e.g., Cieza, 2008; Merín et al., 2008). In particular, young stellar objects with no IR excess shortward of $10\,\mu$m, but with significant excess emission at wavelengths longer than $\sim24\,\mu$m, are interpreted as being in an evolutionary phase of disc clearing and are hence classified as transitional objects (Furlan et al., 2006; Najita et al., 2007b). Evidence for gaps in the disc of transitional objects have also been reported (Brown et al., 2007; Espaillat et al., 2008). In one of these, LkCa 15, the most likely mechanism for gap-opening in the disc seems to be planet formation (Espaillat et al., 2008). Disc clearing may also be due to the presence of a companion, as in the case of CoKu Tau/4 (Ireland and Kraus, 2008).

Here I present a synoptic study of the spectroscopic variability of T Cha, a transitional T Tauri star (Brown et al., 2007) displaying a UX Ori-like behaviour. T Cha was observed in the course of a project aiming to reveal and monitor young spectroscopic binary systems (Esposito et al., 2007; Guenther et al., 2007).

The scheme of the chapter is the following. In Sect. 2.2 I summarise the main observed properties of T Cha as known from previous studies. In Sect. 2.3 I present the observations and data reduction, while in Sect. 2.4 I describe the radial velocity and vsin i determinations. In Sects. 2.5 and 2.6, I report the analysis performed on the spectrum of the object, focusing on the non-photospheric contribution and, in particular, on the variability of the most prominent emission features (e.g., Hα, Hβ, and the [OI] 6300 Å lines). In Sect. 2.8 I analyse the spectral energy distribution of T Cha, while in Sect. 2.9 I discuss the results and present the interpretation of the object.

2.2 Observed properties of T Cha

T Cha shows strong photometric variability (up to 3 magnitudes in the V-band) mainly characterised by erratic changes (Covino et al., 1992; Hoffmeister, 1958; Mauder and Sosna, 1975), and by a UX Ori-like behaviour (i.e., the star becomes redder as it fades), with a tight correlation between brightness and colour (Alcalá et al., 1993; Covino et al., 1996). A periodicity of $3^{\mathrm{d}}.2$ was found by Mauder and Sosna (1975). Spectroscopic variability in the most prominent emission lines was reported by Gregorio-Hetem et al. (1992) and Alcalá et al. (1993).

The PMS nature of T Cha was established by Alcalá et al. (1993) on the basis of the lithium criterion combined with the Hα emission strength and the presence of strong IR excess emission, while the spectral type G8 V (Alcalá et al., 1993) is earlier than that of a typical T Tauri star. From the strength of the Hα emission in former spectra, T Cha had been initially regarded as a wTTS (Alcalá et al., 1993), but later this classification turned out to be inconsistent with the strong variability of the star (Alcalá et al., 1995; Geers et al., 2006; Gras-Velazques and Ray, 2005). Moreover, besides the IR excess indicating the presence of circumstellar material, the object occasionally exhibits forbidden neutral oxygen lines that are not seen in wTTS spectra. Brown et al. (2007) modelled the SED and interpreted it in terms of a transitional disc.

T Cha is located near the edge of the small cloud G300.2-16.9, also known as the *Blue Cloud*, in the direction of the Chamaeleon dark cloud complex (Nehme et al. 2008). In the Hipparcos Catalogue, a distance of 66^{+19}_{-12} pc is reported, although the error in the parallax is probably far higher because of the strong variability of the star (reported to vary between 10.4 and 13.4 mag in the H_P-band during the period of observation). More reliable estimates of the distance were obtained from proper motion studies by Frink et al. (1998) and by Terranegra et al. (1999), suggesting that T Cha is part of an association of stars at nearly 100 pc. Here I adopt the latter value.

2.3 Observations and data reduction

2.3.1 High-resolution spectroscopy

Data were acquired at the ESO-La Silla Observatory using the echelle spectrograph FEROS (Fiber-fed Extended Range Optical Spectrograph), first installed at the 1.5m and, since October 2002, then mounted at the 2.2m telescope. The high resolving power (R~48000) and the wide useful

Table 2.1: Journal of FEROS observations and radial velocity measurements.

Date	HJD $-2400000.$	RV_g (km/s)	σ_{RV} (km/s)	Date	HJD $-240000.$	RV_g (km/s)	σ_{RV} (km/s)
27 Mar 1999	51265.537	14.27	0.27	22 May 2000	51687.648	22.97	1.77
27 Mar 1999	51265.576	16.89	0.68	23 May 2000	51688.640	9.82	0.31
28 Mar 1999	51265.662	15.09	1.63	04 Jan 2001	51913.860	13.86	2.13
28 Mar 1999	51266.573	18.21	0.73	09 Jan 2001	51918.775	15.65	2.15
29 Mar 1999	51266.636	21.39	0.68	14 Jan 2001	51923.824	14.89	0.56
29 Mar 1999	51266.672	21.30	0.90	19 Apr 2001	52019.578	16.00	1.81
30 Mar 1999	51267.692	14.09	0.25	26 Apr 2001	52026.586	14.48	1.12
30 Mar 1999	51267.801	17.88	0.47	26 Apr 2001	52031.573	14.43	0.28
30 Mar 1999	51267.874	18.01	1.38	14 Feb 2002	52319.745	12.63	0.36
31 Mar 1999	51268.624	11.32	0.87	17 Feb 2002	52322.742	27.48	2.56
31 Mar 1999	51268.727	16.21	0.86	08 Apr 2002	52372.606	14.70	-
31 Mar 1999	51268.850	6.43	2.01	21 Apr 2002	52385.529	16.44	0.87
31 Mar 1999	51268.900	12.20	1.44	01 May 2002	52395.617	4.33	1.22
01 Apr 1999	51269.657	12.05	1.15	02 May 2002	52396.614	9.93	-
01 Apr 1999	51269.771	13.09	1.00	12 Mar 2003	52710.601	21.73	0.30
01 Apr 1999	51269.857	15.80	1.56	12 Mar 2003	52717.620	14.13	1.51
16 May 1999	51315.622	18.17	0.76	25 Mar 2003	52723.588	15.96	2.33
17 May 1999	51316.612	6.43	0.82	02 Apr 2004	53097.541	15.57	0.87
18 May 1999	51317.627	16.67	1.77	09 Apr 2004	53104.652	11.28	1.18
19 May 1999	51318.591	13.50	1.72	26 Apr 2004	53122.685	15.93	0.48
21 May 1999	51320.591	17.78	0.52	10 May 2004	53137.672	22.23	0.66
22 May 1999	51321.580	12.72	2.92	10 May 2005	53501.652	29.06	0.87
09 May 2000	51674.670	18.52	0.46	02 Jun 2005	53524.597	6.63	1.35
19 May 2000	51684.617	9.90	0.52	30 Jun 2005	53552.546	14.31	1.09
21 May 2000	51686.632	21.19	2.59	19 Aug 2005	53602.488	29.51	1.95

spectral range ($3600 - 9200\,\text{Å}$) make FEROS particularly suitable for radial-velocity (RV) monitoring and spectral-line variability studies. FEROS was operated in the $Object + Sky$ configuration, in which a sky spectrum is acquired simultaneously with the object through an adjacent fiber.

From 1999 to 2006, 50 FEROS spectra were acquired with quite different signal-to-noise ratios (S/N), due not only to the change of telescope or different observing conditions but also to the strong variability of the star. The observation were carried on within a project on young spectroscopic binary systems. For such reason, the time coverage of the data is rather uneven, with some spectra acquired on daily temporal base and others separated by several months.

The data reduction was performed using the specific FEROS Data Reduction Software (DRS) implemented in the ESO-MIDAS[1] environment. The reduction steps were the following: bias subtraction and bad-column masking; definition of the echelle orders on flat-field frames; subtraction of the background diffuse light; order extraction; order by order flat-fielding; determination of wavelength-dispersion solution by means of ThAr calibration-lamp exposures; rebinning to a linear wavelength-scale ($\Delta\lambda = 0.03$ Å) with barycentric correction; and merging of the echelle orders. All the spectra were then normalized to the continuum.

More details about the data reduction procedure and technical specifications of the instrument can be found at the FEROS Web site[2]. We emphasise that the high stability of the instrument allows an internal accuracy in the wavelength calibration of approximately $200\,\text{m}\,\text{s}^{-1}$ (average residual $r.m.s. \sim 3.5 \times 10^{-3}\,\text{Å}$). A log of the FEROS observations is provided in Table 2.1.

Apart from the FEROS data, I include measurements from an older set of high-resolution CASPEC spectra. To date such data are the only one acquired simultaneously to optical broad-band photometry on two consecutive nights, 1994 January 31 and February 1 (Covino et al., 1996). Details about the instrumental set-up and data reduction can be found in Covino et al. (1997)

2.3.2   Low-resolution spectroscopy

In addition to the high-resolution spectroscopy, I analyzed unpublished low-resolution (R∼2000) spectra gathered during various observing runs conducted between 1993 and 1995 using the Boller & Chivens spectrograph at

---

[1]Munich Image Data Analysis System
[2]http://www.ls.eso.org/lasilla/sciops/2p2/E2p2M/FEROS
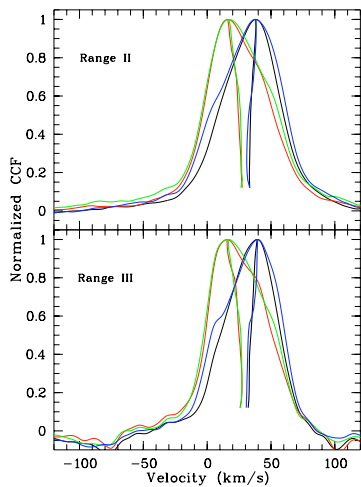
Figure 2.1: Changes in the CCF in the period 19-23 May 2000, in two different wavelength ranges. The different colours refer to the following dates: 19 May (*black*), 21 May (*red*) 22 May, (*green*), 23 May (*blue*). The corresponding bisectors are also traced. Velocity is relative to the template star HD 152391.
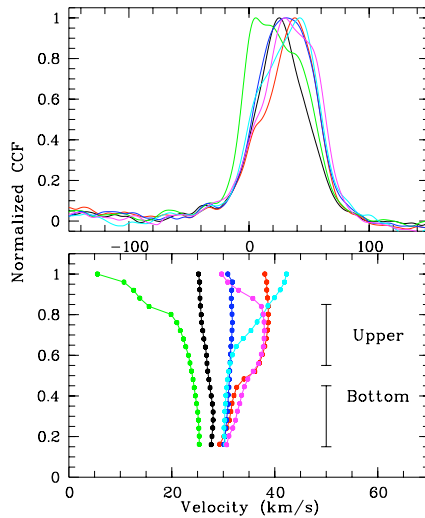
Figure 2.2: CCF peaks between 16 and 22 May 1999 (upper panel). Velocity is relative to the template star. The different colours refer to the following dates: 16 May (*black*), 17 May (*red*), 18 May (*green*), 19 May (*blue*), 21 May (*yellow*), 22 May (*pink*). The lower panel shows, on expanded scale, the corresponding CCF bisectors.

the ESO 1.5m telescope at La Silla, Chile. The reduction of these data was performed as described in Alcalá et al. (1995). These spectra were calibrated in relative fluxes using a standard star.

2.4 Cross-correlation function analysis

2.4.1 Radial velocity determinations

We used the cross-correlation technique to determine the radial velocity of T Cha from the FEROS spectra. As a template, I chose a spectrum of the G8.5 V star HD152391 (RV=44.8 km s^{-1} and $v \sin i = 3$ km s^{-1}) (Nordström et al., 2004), observed with the same instrumental set-up.
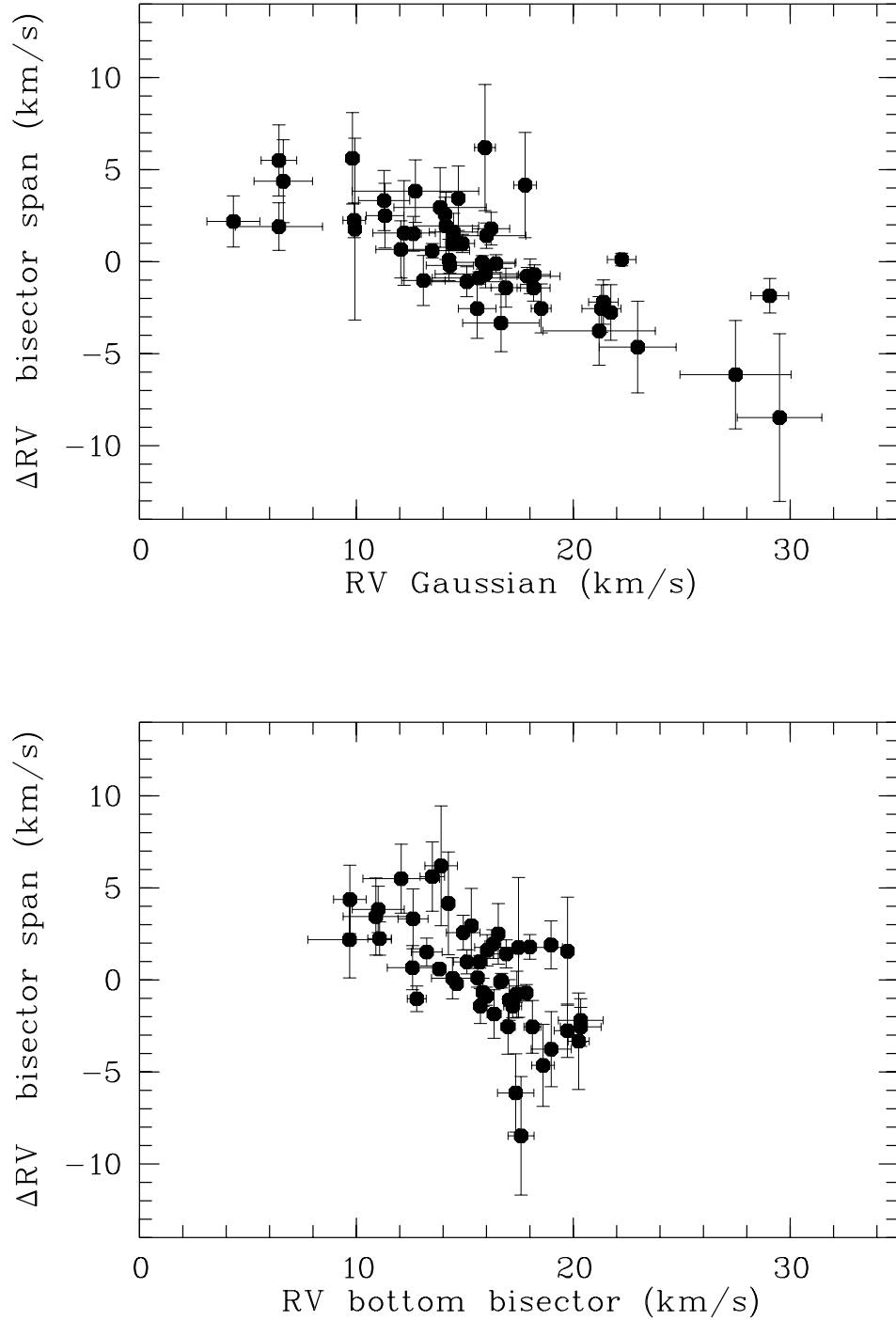
Figure 2.3: The radial velocity measurements from Gaussian-fit method versus the "bisector velocity span" (i.e. the difference between the upper and bottom bisector mean velocities) are plotted in the *left* panel. The *right* panel shows, instead, the mean radial velocity of the CCF bisector bottom versus the "bisector velocity span".

I followed the prescription by Esposito et al. (2007), i.e., a Gaussian was fitted to the peak of the cross-correlation function (CCF), computed in six distinct spectral ranges. In some cases, the Gaussian fit failed, and in such cases I calculated the moments of the CCF profile and took the first-order moment as an RV estimator. In the end, I adopted as RV value and associated error, the average of the RV determined in the different ranges and their r.m.s. dispersion, respectively. All RV measurements are reported in Table 2.1. The RV values vary with time ranging between 6 and $30 \, \mathrm{km \, s^{-1}}$. A period search was performed on these data, but no clear indication of periodicity was found.

2.4.2 CCF bisector analysis

The Gaussian fit may sometimes appear inadequate due to asymmetries in the CCF peak. Asymmetries in stellar absorption lines can arise for several reasons and may be conveniently represented by line bisectors. In some cases, variations in the bisector shape may arise due to photospheric spots crossing the stellar disc as the star rotates, whereas uncorrelated variations in both bisector position and shape may indicate an unresolved spectroscopic system (Dall et al., 2006; Santos et al., 2002).

From the correlation between RV changes and bisector orientation, Queloz et al. (2001), in the case of HD 166435, stated that the periodicity in their RV data was not due to an unseen secondary object orbiting the star, but to stellar activity. We adopted the same tool to verify whether RV shifts measured by a Gaussian fit are purely due to changes in the CCF peak shape, or reflect true changes in the radial velocity of the star.

An example of the variability of the CCF peak (and corresponding bisector) of T Cha on daily timescales is shown in Figs. 2.1 and 2.2. For each of the six spectral ranges considered in Sect. 2.4.1, I divided the corresponding CCF bisector into two intervals as in Queloz et al. (2001): an upper part, where the strongest changes occur, and a lower one, where the bisector position appears more stable (see in Fig. 2.2). The RV difference between the top and bottom bisector's mean velocities yields information about the bisector orientation. This quantity, called "bisector velocity span" (Dall et al., 2006; Queloz et al., 2001; Toner and Gray, 1988), is a good measure of the changes in bisector orientation, and hence of the asymmetry of the peak. The variations in the central part of the CCF, which reflect the higher stability of the wings compared to the peak can be easily discerned.
The comparison between the RV values obtained from a Gaussian-fit and by a bisector analysis is shown in Fig. 2.3.

The left panel shows how the RV values from a Gaussian-fit are well

correlated with the bisector velocity span. The Gaussian function reproduces well only one of the two sides of an asymmetric CCF peak, leading to a systematic shift in the measured RV. On the other hand, the bisector values, at the bottom part of the profile, versus the bisector span show a weaker correlation than the Gaussian-fit values (Fig. 2.3 right panel).

The RV determinations derived from the bisector method, although of lower amplitude than the values derived from the Gaussian-fit method, confirm that RV is indeed variable, considering the average uncertainty of $1.7\,\mathrm{km\,s^{-1}}$. We performed Fourier analysis, using the formulation of the periodogram given by Scargle (1982), to search for possible periodicities in the radial velocity data, although no clear values were identified. This might in part be due to the extremely uneven temporal sampling. We had only one relatively long run of six consecutive nights, but when analysing this run alone, no hint of periodicity was found on a timescale of a few days.

Although the presence of blended spectroscopic components cannot be excluded, the lack of a clear periodicity prevents the drawing of robust conclusions about the possible binarity or multiple-nature of T Cha. As in Queloz et al. (2001), the correlations between the RV values from the Gaussian-fit method and the "velocity span" indicate as most plausible explanation the presence of inhomogeneities of variable extent moving across the photospheric disc, either intrinsic to the star (e.g., cool spots), or external to it (e.g., clustered orbiting material). Hence, in the following, T Cha will be treated as a single star. For the purposes of photospheric spectrum subtraction (see Sect. 2.5.2), I used the bottom bisector's mean RV value.

Table 2.2: Radial velocity determinations, both from gaussian fit and bisector method, and equivalent widths of Hα and [O I] 6300Å measured on FEROS spectra.

HJD −2450000	RV$_b$ (km/s)	ΔRV$_b$ (km/s)	W$_{\mathrm{H}\alpha}$ (Å)	$\sigma_{\mathrm{H}\alpha}$ (Å)	W$_{\mathrm{H}\beta}$ (Å)	$\sigma_{\mathrm{H}\beta}$ (Å)	W$_{6300}$ (Å)	σ_{6300} (Å)
51265.537	14.64	1.07	−6.26	1.06	−1.37	0.78	−0.81	0.05
51265.576	16.54	1.14	−6.56	0.50	−0.34	0.29	−1.00	0.14
51265.662	17.21	0.61	−7.50	0.30	−0.56	0.24	−1.01	0.11
51266.573	17.81	0.54	−10.64	0.42	−2.00	0.29	−1.34	0.01
51266.636	20.57	1.81	−12.46	0.37	−2.02	0.38	−1.48	0.15
continued on next page								

				continued from previous page				
HJD −2450000	RV$_b$ (km/s)	ΔRV$_b$ (km/s)	W$_{H\alpha}$ (Å)	$\sigma_{H\alpha}$ (Å)	W$_{H\beta}$ (Å)	$\sigma_{H\beta}$ (Å)	W$_{6300}$ (Å)	σ_{6300} (Å)
51266.672	20.70	1.98	−12.36	0.80	−2.89	0.32	−1.56	0.11
51267.692	14.35	2.16	−2.89	0.39	−0.01	0.21	−0.58	0.12
51267.801	17.58	0.48	−2.72	0.26	0.03	0.23	−0.43	0.06
51267.874	17.81	0.82	−2.55	0.29	0.03	0.22	−0.34	0.03
51268.624	15.40	1.88	−2.83	0.36	0.32	0.23	−0.40	0.03
51268.727	17.10	1.16	−5.32	0.35	−0.41	0.20	−0.39	0.05
51268.850	18.39	1.29	−5.05	0.41	0.07	0.25	−0.35	0.04
51268.900	18.75	2.07	−3.96	0.35	0.10	0.36	−0.39	0.03
51269.657	12.76	1.46	−6.18	0.47	−0.31	0.28	−0.78	0.05
51269.771	13.42	0.91	−5.19	0.63	−0.76	0.40	−0.77	0.11
51269.857	16.56	0.29	−4.23	0.55	−0.95	0.44	−0.80	0.17
51315.622	17.65	0.83	−22.68	0.39	−2.88	0.51	−1.88	0.25
51316.612	10.54	3.80	−23.93	0.95	−5.89	0.70	−2.06	0.22
51317.627	20.90	1.78	−20.20	1.03	−4.30	0.39	−0.88	0.06
51318.591†	13.42	0.49	−20.65	0.28	−3.03	0.32	−1.22	0.07
51320.591	12.61	2.59	−1.42	0.30	1.08	0.17	−0.28	0.03
51321.580	9.64	2.72	−7.56	0.55	−0.07	0.29	−0.64	0.04
51674.670	17.39	1.38	−0.75	0.38	0.87	0.67	−0.35	0.03
51684.617	10.45	1.69	−2.39	0.34	0.43	0.25	−0.69	0.03
51686.632	19.51	2.50	−1.13	0.22	0.59	0.39	−0.52	0.04
51687.648	19.71	2.94	−0.88	0.21	0.86	0.29	−0.39	0.03
51688.640	11.37	3.17	−2.34	0.35	−0.06	0.43	−0.48	0.07
51913.860	13.69	1.88	−1.46	0.41	0.55	0.19	−0.23	0.04
51918.775	15.90	0.43	−1.86	0.29	0.15	0.23	−0.22	0.04
51923.824	14.91	0.54	−1.12	0.40	−0.20	0.17	−0.14	0.01
52019.578	16.07	0.97	−23.82	0.45	−4.06	1.09	−1.83	0.02
52026.586	15.03	1.05	−3.80	0.40	−0.26	0.26	−0.55	0.05
52031.573	14.64	0.95	−9.18	0.68	−1.45	0.30	−0.64	0.04
52319.745	12.66	1.40	0.26	0.31	1.22	0.12	−0.26	0.04
52322.742†	19.18	3.41	−8.56	0.40	−1.23	0.75	−1.02	0.06
52372.606	9.92	2.40	−29.09	0.95	−5.60	0.55	−2.33	0.18
52385.529	16.54	0.62	−3.82	0.32	−0.60	0.31	−0.49	0.02
52395.617	9.46	2.23	−20.92	1.11	−5.22	0.71	−1.97	0.11
52396.614	16.20	3.49	−11.51	1.29	−0.50	0.50	−1.78	0.23
52710.601	20.00	1.93	−0.93	0.22	0.57	0.16	−0.31	0.03
52717.620	15.79	1.78	−13.51	0.45	−2.06	0.50	−1.16	0.07
				continued on next page				

			continued from previous page					
HJD	RV_b	ΔRV_b	$W_{H\alpha}$	$\sigma_{H\alpha}$	$W_{H\beta}$	$\sigma_{H\beta}$	W_{6300}	σ_{6300}
-2450000	(km/s)	(km/s)	(Å)	(Å)	(Å)	(Å)	(Å)	(Å)
52723.588	15.80	0.51	-2.09	0.31	0.62	0.47	-0.35	0.01
53097.541	19.17	1.55	-6.14	0.34	-0.18	0.25	-0.72	0.02
53104.652	11.38	2.22	-0.93	0.21	0.77	0.15	-0.20	0.10
53122.685	11.70	3.40	-22.39	0.50	-3.59	1.23	-2.00	0.27
53137.672	15.42	0.86	-4.21	0.21	0.40	0.29	-0.23	0.11
53501.652	16.43	1.11	-8.22	0.34	-1.23	0.67	-0.59	0.06
53524.597	7.95	2.57	-5.55	0.27	-0.18	0.41	-0.51	0.02
53552.546	14.36	0.37	-1.06	0.25	-0.04	0.23	-0.22	0.04
53602.488	20.32	4.58	-8.66	0.34	-0.77	0.60	-0.68	0.05

† He I 5876 Å detected

2.4.3   Projected rotational velocity

I evaluated the projected rotational velocity, $v \sin i$, of T Cha by measuring the full width at half maximum (FWHM) of the CCF peak for the spectra with higher signal-to-noise ratio. We first established a relation between the FWHM and $v \sin i$, as described in Covino et al. (1997), using the template spectrum of HD 152391 broadened artificially by various $v \sin i$ values. The $v \sin i$ value determined in this way was $37 \pm 2 \, \mathrm{km \, s^{-1}}$. The same measurement was repeated on an average spectrum obtained by combining a total of 34 spectra with $\mathrm{S/N} \gtrsim 50$ around 6000 Å. The $v \sin i$ determined in the average spectrum is consistent with the previous value. However, when extending the measurements to all spectra, I identified a few with narrower spectral lines, yielding a $v \sin i$ of nearly $30 \, \mathrm{km \, s^{-1}}$. Hence, I checked the $v \sin i$ determinations by directly fitting each spectrum with an artificially broadened template, which confirmed that some spectra had smaller line widths.

In Fig. 2.4, I report the $v \sin i$ values obtained from CCF Gaussian-fit FWHM calibration versus the width at half maximum of the CCF peak measured directly. In this case, it is obvious that the width of the lines does not provide a reliable measure of the rotational velocity. A variable line-width is indicative of either blended spectroscopic components or the presence of inhomogeneities moving across the stellar disc that alter the shape of photospheric lines. However, no correlation is found between the RV (either from a Gaussian-fit or bisector method) and the $v \sin i$ measurements.

From a periodogram analysis based on data points from the spectra of higher signal-to-noise ratio, I found a peak at about $0.25 \, \mathrm{cycles \, day^{-1}}$, or a period close to 4 days. This period does not differ dramatically from that found by Mauder and Sosna (1975) and might reflect a rotational modulation
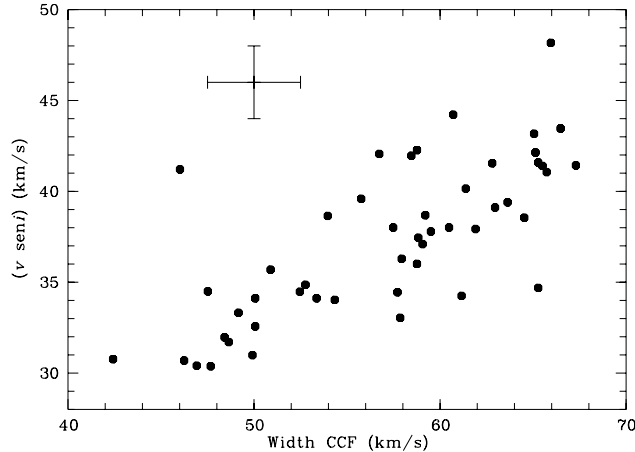
Figure 2.4: Projected rotational velocity from CCF Gaussian-fit calibration versus FWHM of the CCF peak. Only the data of the highest S/N are considered here.

induced by photospheric spots or other types of inhomogeneities transiting over the stellar disc.

2.5 The spectrum of T Cha

2.5.1 Photospheric spectrum and lithium abundance

The spectrum of T Cha is that of a G8 V star with strong absorption in the Li I resonance line at λ 6708 Å and a few emission lines typical of TTS. The spectral type does not change from one spectrum to the other, as also demonstrated in Sect. 2.7. Figure 2.5 shows the good match between the photospheric spectrum of T Cha and that of the template. The equivalent width (EW) of the lithium line was measured in each spectrum of the FEROS data-set. The measurements were found to be internally consistent, within the errors, yielding a mean value of $EW_{Li} = 360 \pm 30$ mÅ. Using the calibration of Pavlenko and Magazzú (1996) and adopting the temperature of 5000 K, I derived a lithium abundance compatible with the cosmic value ($\log N_{Li} = 3.2$), with an uncertainty of 0.2 dex. It is important to recall that this determination is strictly dependent on the effective temperature. At a temperature of 5500 K, as adopted by Kenyon and Hartmann (1995) for a
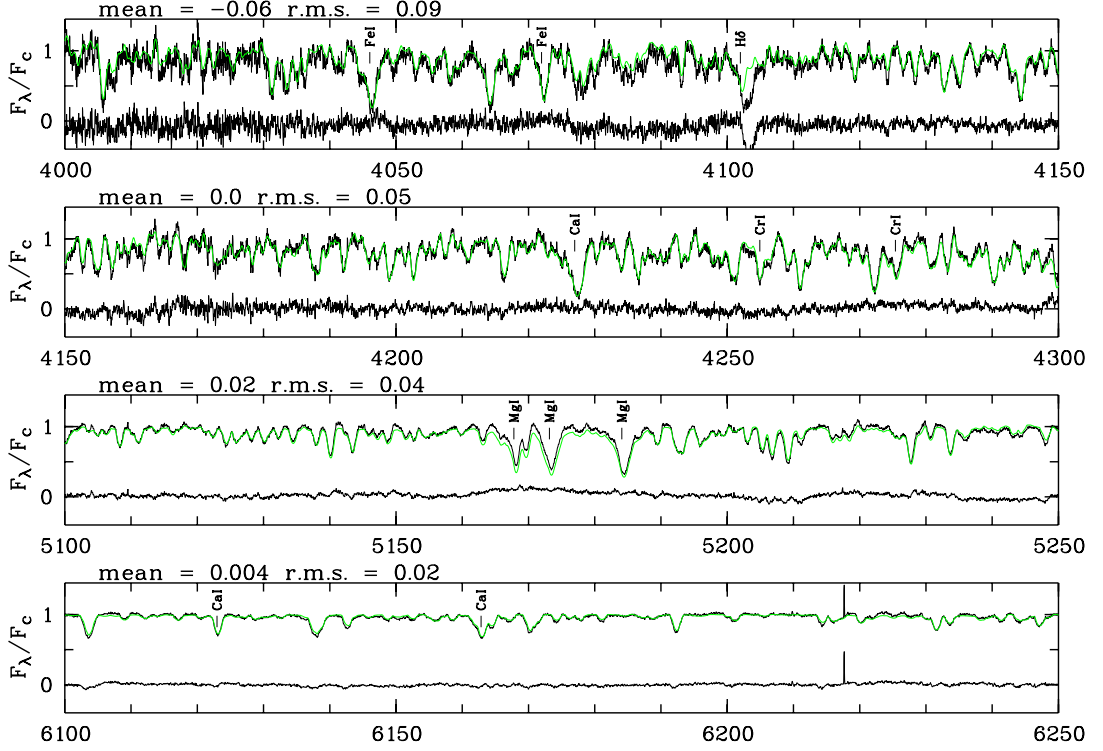
Figure 2.5: Spectrum of T Cha obtained on 14 Feb 2002. The green line represents the spectrum of the template (HD152391 G8.5V) artificially broadened for rotation. In each panel is also shown the residual spectrum after subtraction. Slight residuals in strong spectral features are mainly due to uncertainties in the normalization to the continuum. The spectrum, with a good S/N, shows a redshifted absorption component at Hδ.

G8 V star, the abundance would increase to 3.6 dex, implying some lithium enrichment with respect to the interstellar value.

2.5.2 Photospheric spectrum subtraction

One of the main goals of this work was to analyse the variability in the emission lines and hence probe the circumstellar environment of T Cha. For this purpose, it is useful to remove the photospheric contribution. We subtracted the photospheric-line spectrum from the FEROS spectra of T Cha using the same template spectrum of HD152391 used in the cross-correlation analysis presented in Sect. 2.4.

All spectra were rebinned to the rest-wavelength frame to take account

of their different RV shifts, derived from the CCF analysis described in Sect. 2.4.1. The template spectrum was broadened artificially by the $v \sin i$ value of $37 \, \mathrm{km \, s^{-1}}$ and then subtracted from each of the T Cha spectra. We assumed that the photospheric spectrum of a TTS resembles that of a main-sequence star of the same spectral type. The photospheric subtraction method allows to determine the possible presence of "veiling". No sign of continuum excess emission was found in T Cha (see Fig. 2.19), confirming the absence of UV-excess in the broad-band photometry (see Sect. 2.8 and Covino et al., 1996).

Examples of the residual profiles of the main emission lines at different dates are shown in Fig. 2.6. Some lines show absorption components shifted toward shorter and/or longer wavelengths. The Hα line is the most variable in both intensity and shape. The residuals of the Na I D lines show either redshifted or blue-shifted absorption components (that are easily distinguishable from the sharp, undisplaced, interstellar component), apparently linked to the presence of a correspondent feature in Hα and Hβ. The sharp interstellar absorption components of the D lines from the associated cloud are also distinguishable, when not suppressed by the sky emission.

2.5.3   Emission line spectrum

Gregorio-Hetem et al. (1992), Alcalá et al. (1993) and Covino et al. (1996) already pointed out some outstanding properties of the variability in the emission lines, but here I exploit the wide spectral coverage of FEROS to analyse more lines simultaneously and identify the line profile changes at higher resolution than in previous works.

The Hα line

The most prominent emission line in the spectrum of T Cha is Hα, which also exhibits impressive variability. The observed equivalent width of the line measured in the FEROS spectra, ranges from about $0.3 \, \text{Å}$ (on 14 Feb 2002) to about $-30 \, \text{Å}$ (on 8 Apr 2002)[3]. Besides the variations in strength, from pure emission to absorption, the line profile is also highly variable in its structure. However, there are no sign of correlation between the profile of the line and its EW. The line extends approximately from -300 to $+300 \, \mathrm{km \, s^{-1}}$. However, much of the emission is concentrated in an interval of almost $400 \, \mathrm{km \, s^{-1}}$ in width centred on zero velocity. In most of the spectra, the Hα line exhibits

---

[3]conventionally, a negative EW indicates line in emission.
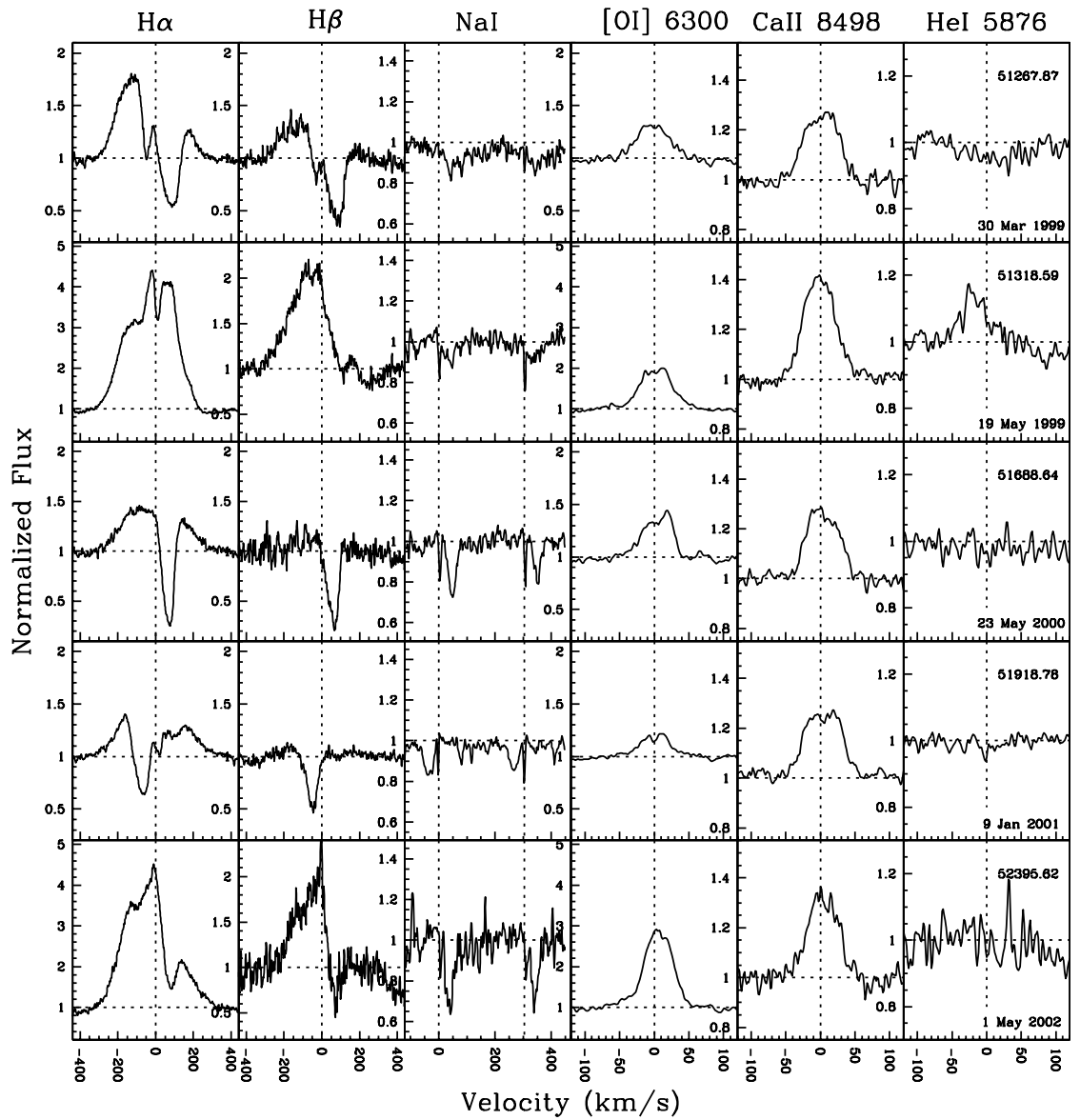
Figure 2.6: Examples of residual line profiles of T Cha in velocity scale. The vertical dotted line marks the rest position in the star frame.

both blue-shifted and redshifted absorption components superimposed on a nearly centred symmetric broad emission. The blue absorption is usually weaker than the red one, although in three spectra of January 2001 it appears stronger (e.g., date 51918 in Fig. 2.6). During five different epochs, the blue absorption reached below the continuum producing a P Cygni profile. In most cases, when the emission component was not so strong, the red absorption was below the continuum, producing a typical inverse-P Cygni profile.

The red absorption is almost always present but with different velocity displacements relative to the rest wavelength, whereas the blue absorption sometimes becomes barely visible or disappears completely. In contrast, the emission on the blue side is generally more intense than the red one. This suggests that the red wing of the line is affected by significant absorption that causes the emission to appear weaker than in the blue wing. No clear regularity appears to exist in the line changes, but some profiles reappear after some time.

The lack of both detectable veiling and UV excess indicates that the accretion rate is rather low. Assuming that the Hα emission is entirely due to accretion, I estimated the mass accretion rate, $\dot{M}_{accr}$, by adopting the relationship found by Natta et al. (2004) between $\dot{M}_{accr}$ and the width of the Hα line at 10% intensity. We emphasise that this quantity does not represent an accurate mass-accretion estimator for two main reasons: *i)* it is not easy to measure, mainly due to the difficulty in defining the continuum level, and *ii)* because the relationship, derived for the substellar mass regime, shows a larger dispersion at higher masses. We determined the width at 10% intensity of the Hα emission only in spectra for which I could perform a Gaussian decomposition of the line profile into an emission component with overlapping absorptions. From those, I derived a mean value of $\dot{M}_{accr} = 4 \times 10^{-9} \, \mathrm{M}_\odot \, \mathrm{yr}^{-1}$.

The Hβ line and higher Balmer lines

The strength of Hβ is also variable and its EW correlates well with that of Hα, as shown in Fig. 2.7. The range of variation is between about 1.2 Å (on 14 Feb 2002) and about -6 Å (on 8 Apr 2002). In most cases, the Hβ line presents typical double-peak emission with higher emission in the blue peak than in the red one. Apart from when emission is stronger, the Hβ profile resembles the Hα one. However, the inverse P Cygni profile appears more frequently than in Hα.

Even if Hα and Hβ have different optical thicknesses and formation regions, their EWs are strongly correlated with each other (Fig. 2.7 lower panel).

Because of the lower efficiency of FEROS at shorter wavelengths and the high variability of T Cha in the U and B bands, little can be said about the behaviour of the higher members of the Balmer series, since Hγ and Hδ are discernible only in a few spectra. Almost no emission is apparent in the residual spectrum, except in one or two cases, but the low S/N still prevents the drawing any robust conclusion. The most intense absorptions, either blue- or redshifted, depending on epoch, can also be identified in the higher Balmer lines (cf. Hδ in Fig. 2.5).

Forbidden Oxygen lines

The forbidden [O I] 6300 and 6363 Å emission lines are observed in the spectrum of T Cha. The contribution of the sky emission lines to the FEROS spectra was subtracted after scaling the sky spectrum by a factor to account for the different efficiencies of the object and sky fibers, determined from the ratio of the flat-field intensities in the corresponding fibers. Figure 2.6 shows the sky-subtracted line at 6300 Å. The width of $\sim 100\,\mathrm{km\,s^{-1}}$ places the line just on the edge between low- and high-velocity components for T Tauri stars (Hartigan et al., 1995).

As in the case of the Balmer lines, the forbidden oxygen lines are of variable intensity, but their profiles remain about the same. The most frequently observed profile is a symmetrical and well-centred emission, but sometimes the line is slightly redshifted by about 10-20 $\mathrm{km\,s^{-1}}$ (see Fig. 2.6). The symmetrical profile suggests that both the approaching and receding parts of the flow contribute to the observed line, i.e., the star-disc system is viewed at relatively high inclination. Redshifted [O I] 6300 Å profiles have also been observed in BP Tau and RW Aur (Hartigan et al., 1995), but are rather unusual for T Tauri stars. Some authors explain the redshifted component in terms of asymmetric outflows (e.g., Hartigan et al., 1995; Hirth et al., 1994).

Remarkably, the equivalent width of the [O I] 6300 Å is correlated with that of the Hα emission (see Fig. 2.7 upper panel). As discussed in the following sections, this correlation indicates that the variations must be related to changes in the intensity of the underlying stellar continuum due to variable circumstellar extinction.

To verify the hypothesis of variable obscuration, I used the only simultaneous spectroscopy and photometry data available (Covino et al., 1996) to evaluate the luminosity in the [O I] line,

$$L_{[\mathrm{O\,I}]} = W_{[\mathrm{O\,I}]} \cdot f_R \cdot 4\pi d^2$$

$$= W_{[\mathrm{O\,I}]} \cdot 10^{-0.4 \cdot R} \cdot 2.69 \times 10^{33} \mathrm{erg\ s^{-1}},$$
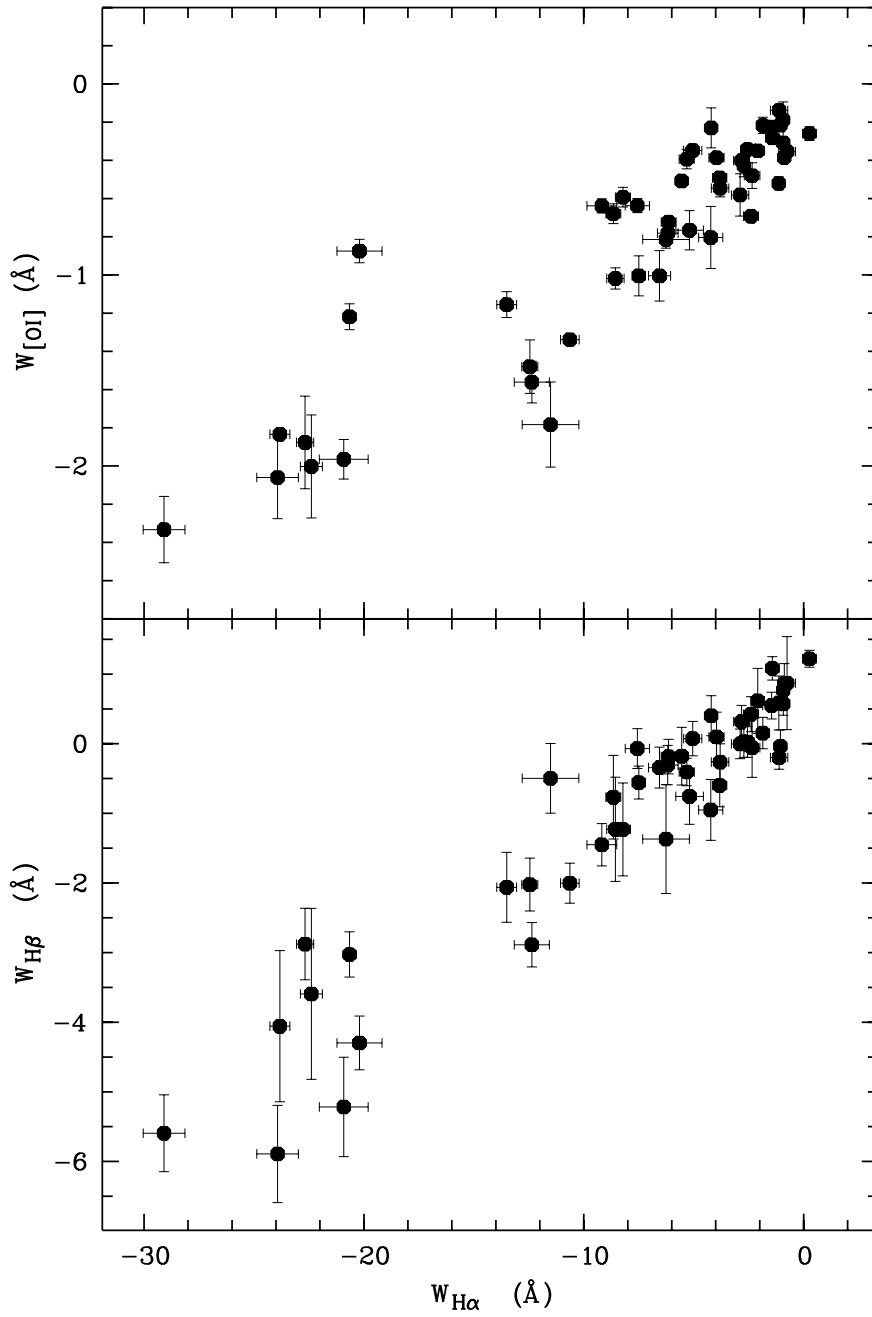
Figure 2.7: Correlations between intensities of the most prominent emission lines measured in the FEROS spectra.

Table 2.3: Equivalent widths of [OI] 6300Å measured in CASPEC spectra (Covino et al., 1996) and line luminosity derived using simultaneous R-band photometry.

JD -2440000	R mag	$W_{[OI]}$ (Å)	$L_{[OI]}$ (10^{28}erg s^{-1})
9384.62	11.47	-0.78±0.06	5.4±0.4
9384.70	11.70	-0.91±0.08	5.1±0.4
9384.87	11.88	-1.24±0.16	5.9±0.8
9385.62	10.56	-0.32±0.03	5.1±0.5
9385.76	10.41	-0.25±0.03	4.6±0.5
9385.87	10.39	-0.24±0.03	4.5±0.6

where $W_{[\text{O\,I}]}$ is the measured equivalent width of [OI], d is the distance of 100 pc, and f_R is the observed flux of the star in the R-band. The latter is given by $f_R = F_0^R \cdot 10^{-0.4 \cdot R}$, where $F_0^R = 2.26 \times 10^{-9}$erg s^{-1}cm^{-2-1} is the R-band flux of a zero-magnitude star (Bessel, 1979). The measured EWs and relative luminosities are reported in Table 2.3.

The luminosity (or the flux) in the [OI] line remains relatively constant with time, as in the case of the UXOR star RR Tauri (Rodgers et al., 2002). Therefore, the strong variability in the emission-line intensity is caused by changes in the stellar continuum flux level rather than the intrinsic variability of the line-emitting region. This explains the correlation between Hα and [OI] discussed in Sect. 2.5.3, justifying the fact that the intensities of the two lines, originating in distinct regions, respond simultaneously to the brightness variations of the star. As the analysis of flux-calibrated low-resolution spectra presented in Sect. 2.7 shows, the intensities of the Hα and [OI] lines are also found to be related directly to the amount of circumstellar extinction affecting the photospheric continuum.

Other emission lines

Franchini et al. (1992) detected a weak variable emission component in the core of the Na I D lines. In the spectral subtraction analysis, I found no sign of this emission, but instead, were able to identify strong redshifted absorption in many residual spectra. that is visible only when the redshifted absorption in Hα is also present (although the reverse is untrue), independently of the equivalent width of the Hα line. On three dates, namely 9 Jan 2001, 21 Apr 2002, and 9 Apr 2005, when the blue-shifted absorption component in Hα was at least as strong as the red one, the feature appeared blue-shifted, but there was no sign of absorption on 14 Jan 2001, when Hα showed a clear

P Cygni profile.

The [NII] 6583 Å forbidden emission line is occasionally observed in the low-resolution spectra when the star reaches its faintest state (see Sect. 2.7).

The He I emission line at 5876 Å was seen on only two dates (19 May 1999 and 17 Feb 2002), while missing in other spectra close to those dates. This line is probably caused by episodic, short-lived flare activity, common in young solar-type stars. As shown in Fig. 2.6, the line appears blue-shifted by about $-30\,\mathrm{km\,s^{-1}}$.

Finally, the emission cores of the two lines 8498 and 8662 Å of the CaII IR triplet are clearly visible. The other line, at 8541 Å, falls in a wavelength gap in-between the echelle orders of FEROS. The equivalent widths of the two measurable lines remain almost constant, with small variations presumably related to chromospheric activity. No correlation is found with other emission lines. The profiles appear always symmetrical and well centred on the star velocity, indicating presumably a chromospheric origin, typical of young stars.

As for higher Balmer lines, the low S/N prevents from analysing the CaII H and K lines, but in some spectra of sufficiently high S/N, a strong emission core, indicative of intense chromospheric activity, is observed.

2.6 Line profile variability on short timescale

The large variety of Hα profiles shown by T Cha appear to occur rather erratically, although this may be caused at least partly by the quite uneven temporal sampling of the spectra.

We used three different series of spectra acquired with a time sampling shorter than one day to investigate variations on short timescales. We analysed separately each of the following three runs: 1) from 27 March 1999 to 1 April 1999 (total of 16 spectra in 5 nights); 2) from 16 to 22 May 1999 (total of 6 spectra in 6 nights); and 3) from 9 to 23 May 2000 (total of 5 spectra in 5 nights). Figure 2.8 shows in each panel the overlap of Hα (top-left box) and Hβ (bottom-left box) line profiles for each of the three runs. The average normalized profile $\langle I_n(\lambda)\rangle$ is also superposed, and is represented by a thicker line. The profiles, and their behaviour, appear to differ in each run, being more erratic in the second period than in the other two. The Hα and Hβ line intensities and profiles change on a daily timescale, with only minor changes occurring during the night. We report in Fig. 2.10, the variability in the positions of the central peak and the two absorption components in Hα during the first run.

To quantify the variability in each line, I examined the variance, σ, and
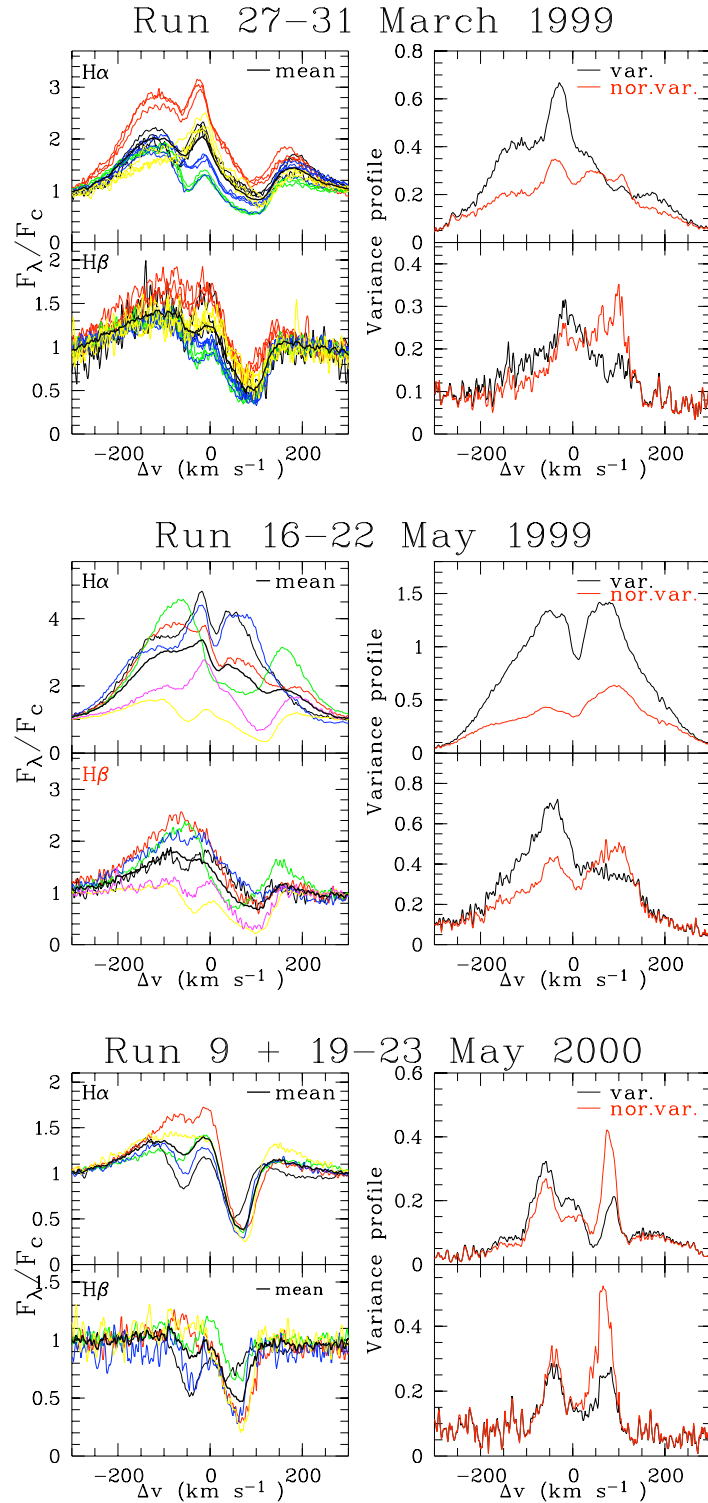
Figure 2.8: Line profiles (*left panels*) and corresponding variance and normalized variance profiles (*right panels*) for Hα and Hβ in three different runs.
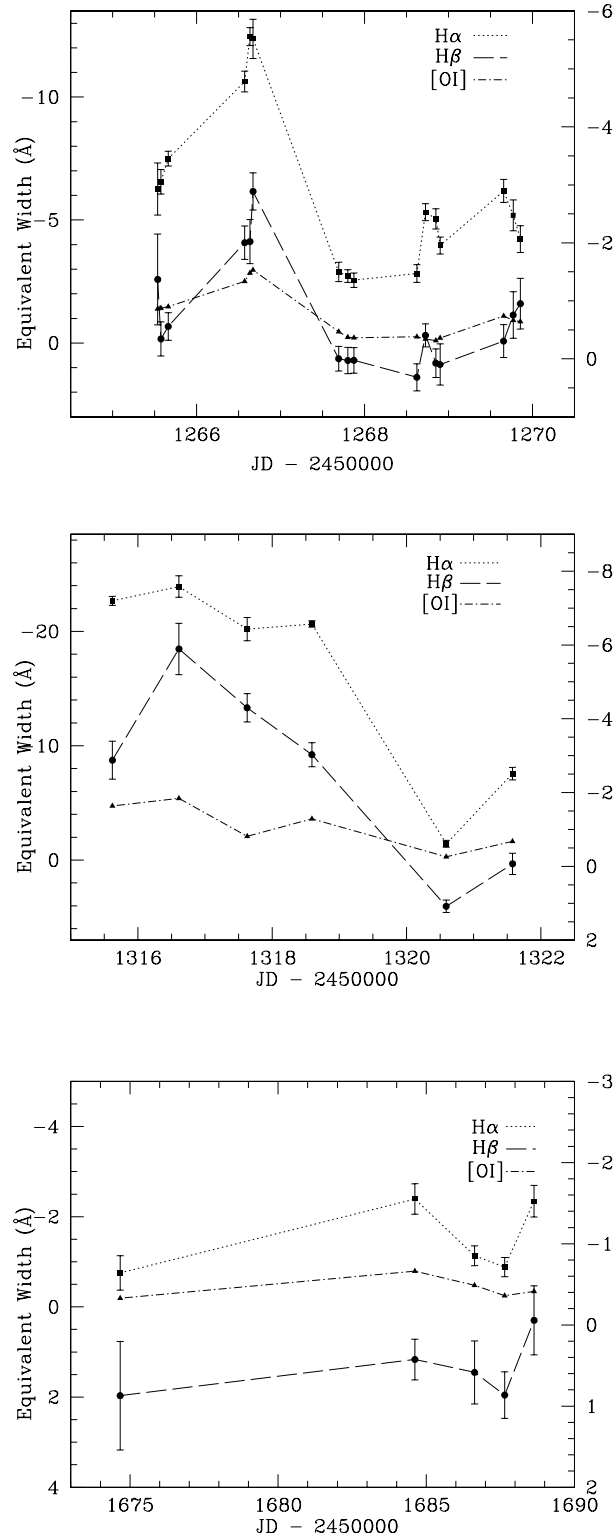
Figure 2.9: Equivalent widths of the main emission lines during the runs displayed in Fig. 2.8. The left scale refers to Hα, while the right one is for Hβ and [OI] lines.
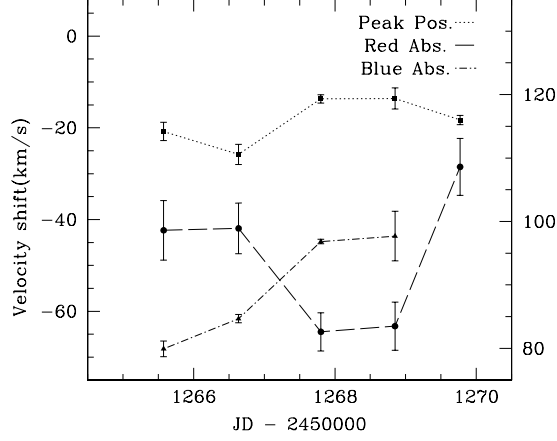
Figure 2.10: Variations in position of the central peak emission and the two absorptions of Hα line during the period from 27 to 30 March 1999. The scale on the right refers to the red absorption, while the one on left refers to the central emission and the blue-shifted absorption.

the normalized variance, σ_n, in the different runs, defined respectively as:

$$\sigma^2 = \Sigma_{i=1}^{N}[I_{n,i}(\lambda) - \langle I_n(\lambda)\rangle]^2/(N-1) \tag{2.1}$$

and

$$\sigma_n^2(\lambda) = \sigma^2(\lambda)/\langle I_n(\lambda)\rangle \tag{2.2}$$

where $I_{n,i}(\lambda)$ is the i-th spectrum. These quantities are plotted in the right panels of Fig. 2.8. If variability were merely caused by the brightening or fading of the stellar continuum flux, the shape of normalized variance profiles would be the same as the average line profile (Johns and Basri, 1995). This is generally not the case, suggesting that some other changes in the Hα forming region also occur.

Figure 2.9 shows the trends of the equivalent widths of the main emission lines with time. Hα and Hβ mainly vary in similar ways. On two dates, their behaviour is different, i.e., the last day of the first run, when the Hα intensity increased as the Hβ intensity decreased, and the third day of the second run, when an increase in Hα intensity did not correspond to an increase in that of Hβ. The [OI] line trend is similar to that of Hα except for during the fourth night of the first run and the last night of the third run, when the

emission intensities of both Balmer lines strengthened, while the [O I] lines did not change. The similarities in the variability of these lines indicate that the processes producing the observed changes must affect contemporaneously circumstellar zones located at different distances from the star, i.e., on length scales of between a few tenths of AU for Hα and a few AUs for [O I].

2.6.1 Correlation Matrices

To test whether the variations across the emission line profiles have a common origin, I computed their correlation matrices (CMs). CMs indicate the linear correlation coefficient between the variation in each velocity bin of the spectral line profile and variations in all other bins for the same or for two different lines. A strong correlation between different velocity bins is indicative of a common origin, or emitting region. If the variability in the emission line is linked to variability in the continuum, then the line profile is highly correlated over a wide range of velocity, producing a typical squarish shape in the CM (Alencar and Batalha, 2002; Johns and Basri, 1995).

We computed the CMs of Hα and Hβ with respect to themselves and to each other. Two-dimensional plots of these matrices for Hα and Hβ in three different runs are shown in Fig. 2.11. No anticorrelation is evident in the matrices. In each run, there are regions that correlate well with themselves, but do not correlate with the remainder of the line. No significant correlation is seen between the red ($\geq 200\,\mathrm{km\,s^{-1}}$) and the blue ($\leq -200\,\mathrm{km\,s^{-1}}$) wings of the profile. However, in the second run, the Hα line exhibits a correlation over a wide velocity range, its squarish form extending from about -300 to nearly $150\,\mathrm{km\,s^{-1}}$. The correlation is disrupted by the blue-shifted absorption, from -150 to $-50\,\mathrm{km\,s^{-1}}$, and the redshifted component, up to about $-100\,\mathrm{km\,s^{-1}}$, which do not correlate with the remainder of the line profile but with the redshifted emission peak, around $130\,\mathrm{km\,s^{-1}}$. This behaviour is not observed in the other epochs. Similarly, in the first run, the broad red absorption from -20 to $150\,\mathrm{km\,s^{-1}}$ breaks the correlation with the blue emission wing, which still correlates weakly with the red emission wing. Interestingly, the square regions in the CMs correspond to some of the highest peaks in the variance profiles, i.e., the blue emission wing, the central peak and the red absorption, respectively.

The Hβ CMs are more affected by noise due to lower S/N at those wavelengths, but again traces of a squarish form can be seen in particular in data from the second run. We also computed the CM between Hα and Hβ, but, although the profiles of the two lines appear to be similar, the corresponding correlation matrices are affected too significantly by noise and no useful information can be extracted from them.
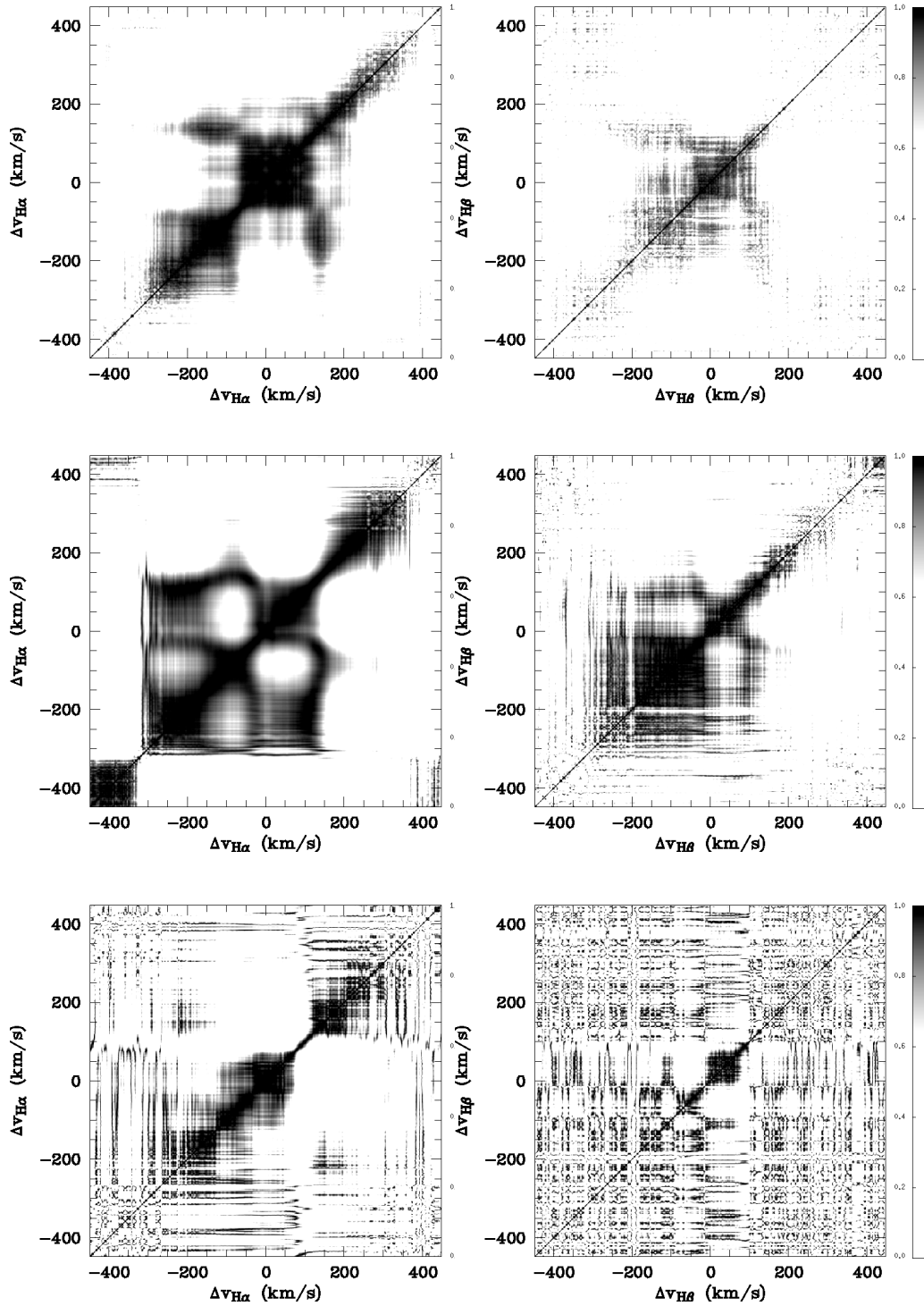
Figure 2.11: Two-dimensional maps of the correlation matrices of Hα (panels on left) and Hβ (panels on right) with themselves, for the three runs of Figs. 2.8. Different squarish regions are distinguishable in the first two runs, indicating a coherence in the variations of Hα intensity in the velocity interval from -300 to $120\,\mathrm{km\,s^{-1}}$.

In conclusion, coherent changes in the velocity interval between -300 and $120\,\mathrm{km\,s^{-1}}$ appear consistent with variations dominated by variable circumstellar obscuration of the stellar photosphere, giving rise, due to a contrast effect, to changes in the relative intensity of emission lines. In the case of magnetospheric accretion, parts of the $H\alpha$ profile, i.e., the redshifted component, are expected to originate in regions close to the star and eventually to be affected by direct obscuration. These may be identified kinematically with the intervals where the correlation breaks down whereas the differences from one epoch to the other possibly reflect changes in the geometry of the emitting region.
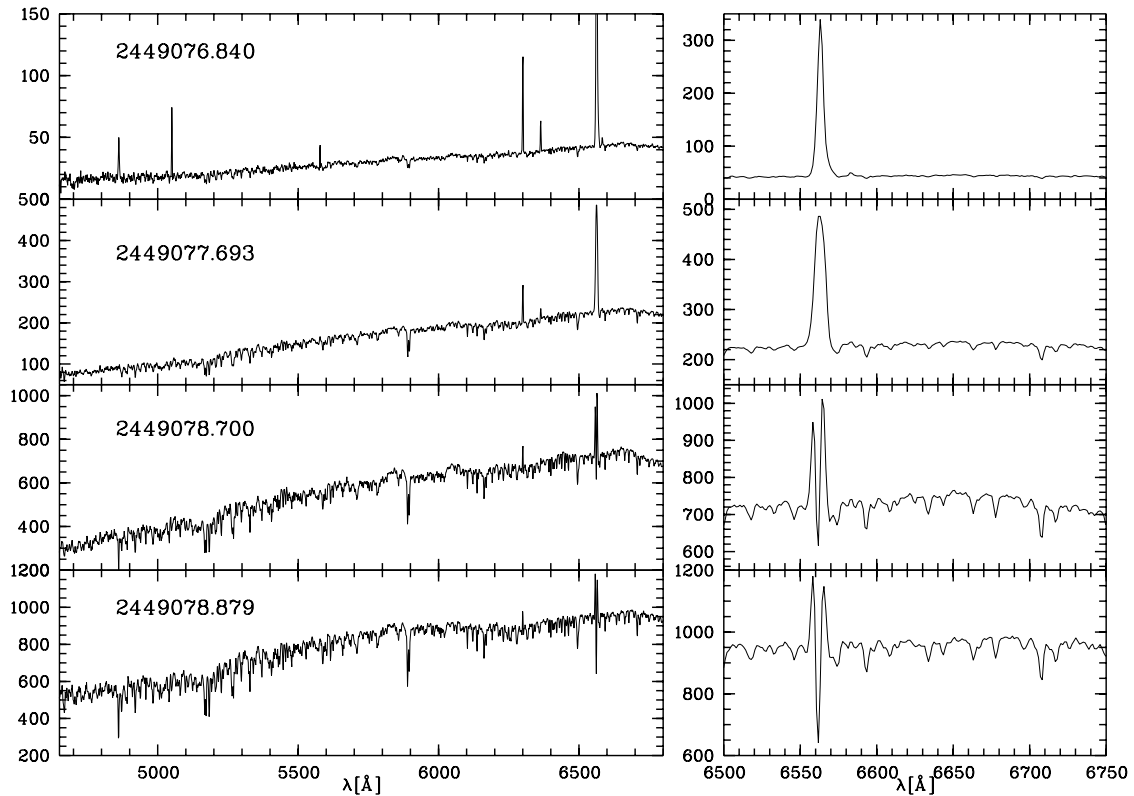
Figure 2.12: Low-resolution spectra of T Cha. The panels on the left side display the whole range, those on the right show the interval containing $H\alpha$ and the Lithium line.

Table 2.4: Equivalent widths of Hα and [O I] 6300Å measured on the low-resolution spectra and corresponding total extinction, A$_V$, obtained as described in Sect. 2.8.

Date	JD -2440000	W$_{H\alpha}$ (Å)	$\sigma_{H\alpha}$ (Å)	W$_{[OI]}$ (Å)	$\sigma_{[Oi]}$ (Å)	A$_V$ (mag)
07 May 92	8749.668	-4.58	0.30	-0.33	0.05	2.2
08 May 92	8750.606	-3.63	0.40	-0.35	0.05	2.4
10 May 92	8752.628	0.40	0.10	-0.13	0.03	1.8
11 May 92	8753.634	-4.87	0.70	-0.22	0.05	2.0
12 May 92	8754.600	-6.42	0.80	-0.87	0.10	2.8
27 Mar 93	9073.698	-1.09	0.20	-0.23	0.05	1.7
27 Mar 93	9073.847	-0.51	0.20	-0.19	0.03	1.4
28 Mar 93	9074.689	1.80	0.20	-	-	1.5
28 Mar 93	9074.843	2.08	0.20	-0.06	0.05	1.5
29 Mar 93	9075.680	0.28	0.20	-0.25	0.05	1.7
29 Mar 93	9075.873	-0.14	0.10	-0.11	0.03	1.7
30 Mar 93	9076.758	-23.70	2.00	-4.16	0.50	3.3
30 Mar 93	9076.840	-34.00	4.00	-6.29	0.55	3.6
31 Mar 93	9077.693	-9.20	1.00	-1.27	0.15	2.6
01 Apr 93	9078.700	-1.80	0.10	-0.26	0.05	1.9
01 Apr 93	9078.879	-0.32	0.10	-0.14	0.05	1.3
02 Apr 93	9079.687	1.90	0.10	-0.06	0.05	1.5
02 Apr 93	9079.879	1.64	0.10	-	-	1.2
30 May 93	9137.531	1.40	0.10	-	-	1.2
31 May 93	9138.515	0.26	0.10	-0.26	0.05	2.0
31 May 93	9138.738	-0.25	0.10	-0.35	0.05	2.4
01 Jun 93	9139.545	-44.60	5.00	-9.20	0.55	4.6
03 Jun 93	9142.495	0.16	0.10	-0.36	0.05	1.5
04 Jun 93	9143.494	-0.23	0.10	-0.48	0.05	2.3
05 Jun 93	9143.736	0.66	0.10	-0.23	0.05	2.2
05 Jun 93	9144.496	-6.20	0.50	-0.57	0.05	2.8
06 Jun 93	9144.718	-5.81	0.60	-0.68	0.05	3.2
28 Jun 93	9167.463	-2.40	0.30	-0.35	0.05	1.8
29 Jun 93	9168.478	-19.3	2.00	-4.18	0.50	3.1
02 Jul 93	9170.519	-7.21	0.60	-0.93	0.10	2.1
03 Jul 93	9172.467	-57.0	5.50	-9.00	0.60	‡
24 Mar 94	9435.745	1.73	0.10	-0.09	0.05	1.8
24 Mar 94	9435.887	2.20	0.20	-0.10	0.03	2.1
25 Mar 94	9436.698	0.55	0.10	-0.23	0.05	1.5
25 Mar 94	9436.900	-1.03	0.10	-0.36	0.05	1.6
26 Mar 94	9437.532	0.96	0.10	-0.24	0.05	1.7
26 Mar 94	9437.672	0.21	0.10	-0.36	0.05	1.5
27 Mar 94	9438.519	-1.10	0.10	-0.30	0.05	1.8

‡ A$_V$ not determined due to very faint continuum

Date	JD -2440000	$W_{H\alpha}$ (Å)	$\sigma_{H\alpha}$ (Å)	$W_{[OI]}$ (Å)	$\sigma_{[Oi]}$ (Å)	A_V (mag)
27 Mar 94	9438.662	-0.95	0.10	-0.27	0.12	1.6
28 Mar 94	9439.520	1.61	0.20	-	-	1.3
28 Mar 94	9439.661	0.95	0.10	-	-	1.7
29 Mar 94	9440.518	0.25	0.10	-0.03	0.05	1.2
29 Mar 94	9440.661	1.05	0.20	-0.03	0.05	1.6
09 Apr 95	9816.807	-0.19	0.10	-0.04	0.05	1.6
10 Apr 95	9817.789	-38.70	3.50	-4.31	0.45	3.4
11 Apr 95	9818.805	0.70	0.10	-0.05	0.05	1.5
12 Apr 95	9819.788	1.05	0.10	-0.14	0.05	1.8

2.7 Variability in the low-resolution spectra

Strong variability was also detected in the low-resolution spectroscopy. We refer in particular to Table 2.4, where I report the equivalent widths of the $H\alpha$ and [OI]$\lambda6300$ Å lines, and to Fig. 2.12, where a sample of low-resolution spectra is shown.

We note that during the May-June 1993 run, the star exhibited spectacular changes between one night and the next. For instance, $H\alpha$ was observed to vary between weak absorption (EW≈ 0) on May 31, to a very strong emission line (EW≈ -50Å) on June 1. The latter spectrum was also characterised by strong [OI] lines, and the [NII] line was also present, while no emission lines were detected in data acquired the two nights before.

The spectacular variability of these lines is illustrated in Fig. 2.13, where two low-resolution spectra, corresponding to close to the maximum and minimum brightness of the star, just two nights apart, are compared after normalising each of them to the flux at $\lambda = 5880$ Å. We recall that these spectra are calibrated in relative flux (see Sect. 2.3.2). The variation in the continuum slope between the two dates is also remarkable, in addition to the emission features appearing prominent when the photospheric continuum looks fainter and heavily reddened.

However, no change in the spectral type of the star is observed. To verify this, I used low-resolution spectra calibrated in relative flux, and applied the methods described in Alcalá et al. (2006) and Gandolfi et al. (2008) to determine simultaneously the spectral type and the visual extinction at the phases of minimum and maximum brightness, respectively. The result, shown in Fig. 2.14, is that the spectral type did not vary to within about half a sub-class, while the visual extinction changed from 1.2 mag in the bright phase to about 4.6 mag in the faint state, respectively. This corresponds to an
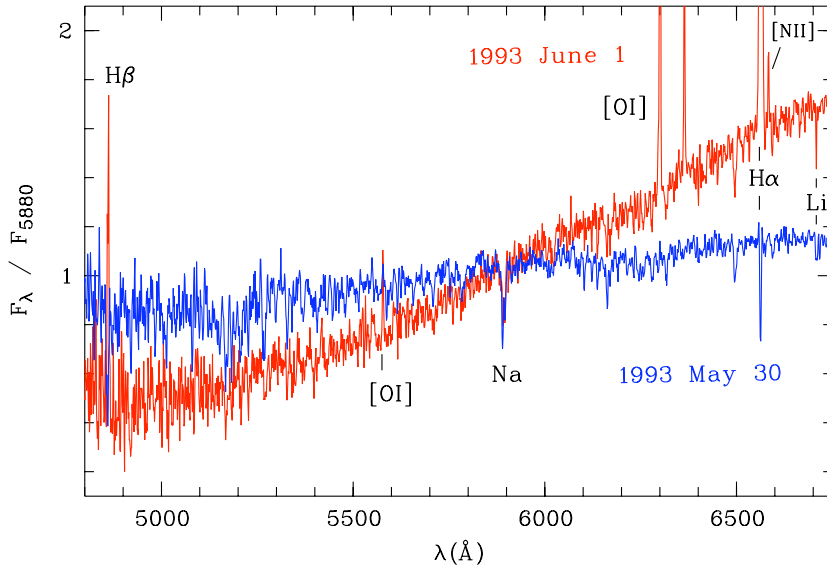
Figure 2.13: Low-resolution spectra of T Cha near minimum (June 1, in red) and maximum brightness (May 30, in blue). The spectra are calibrated in relative flux and normalised to the flux at $\lambda = 5880\,\text{Å}$. Emission features, only visible in the spectrum corresponding to the fainter level, are marked.

extinction increase of at least $3.4\,\text{mag}$ between the bright and faint states. By instead using the spectrum corresponding to the bright level as a template, an extinction of 3.3 mag is needed to reproduce the faint spectrum, and, apart from emission lines, the residual is indeed quite low (residual mean value is 0.001 ± 0.03).

We applied the same procedure to each of the low-resolution spectra and determined the corresponding value of A_V (see Table 2.4), with estimated errors of about 10%. This takes account of the uncertainty in the fit, as well as the relative flux calibration, but not systematic effects caused by deviation of the circumstellar extinction from the normal interstellar law, as shown in Sect. 2.8. The two panels of Fig. 2.15 show that a clear trend exists between the amount of visual extinction and the intensity of the Hα and [OI] 6300Å emission lines. This indicates that the observed variations do not reflect intrinsic changes in the stellar photosphere, but arise presumably from variable circumstellar extinction, as can be inferred in Fig. 2.13 from the different continuum slopes of two spectra taken near maximum (on 30 May 1993) and minimum (on 1 Jun 1993) brightness. The histogram in Fig. 2.16 indicates that the highest extinction events are relatively rare, while events
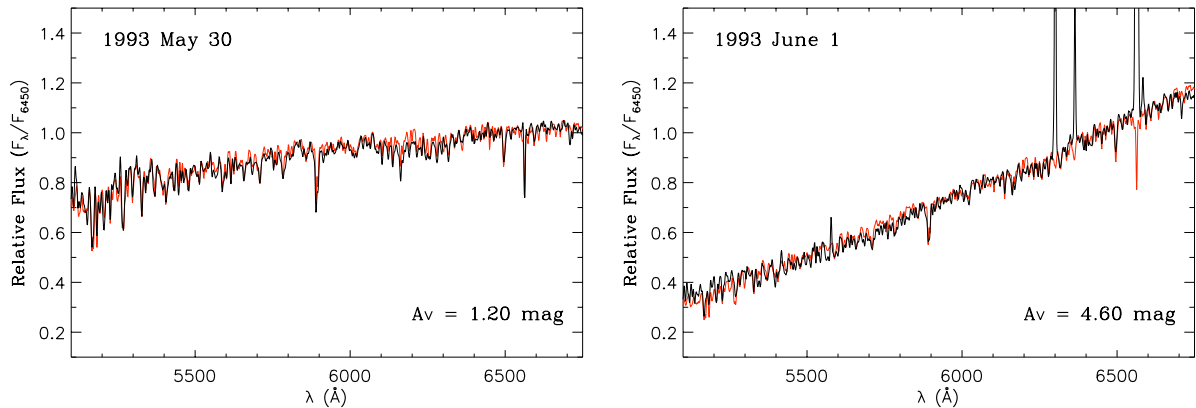
Figure 2.14: Best-fit of spectral-type templates to the spectra shown in Fig. 2.13. The spectra of T Cha are shown as thin (black) lines, while the templates are shown as thick (red) lines. The corresponding values of total visual extinction, as derived from the two-parameter fit adopting a normal interstellar extinction law with $R_V = 3.1$, are also indicated for both the faint and bright stage, respectively.

with differential extinction below $1\,\mathrm{mag}$ are more frequent.

2.8 The spectral energy distribution

We constructed the observed SED of T Cha using all optical and near-IR photometry available(Alcalá et al., 1993; Covino et al., 1996), as well as data from public catalogues. In Fig. 2.17, the SED is shown for wavelengths shorter than $10\,\mu$m. We remark that photometric errors are smaller than the symbol size, and the considerable scatter of the optical ($UBVRI$ bands) data points reflects the significant variability of the star. Although of smaller amplitude, variability in the near-IR (JHK bands) can also be appreciated. Therefore, relying on data that have not been acquired simultaneously may be a limitation in the SED analysis.

Table 2.5: Total to selective extinction ratios, $R_\lambda = A_\lambda/E_{B-V}$, for T Cha, derived from $UBVRI$ photometry (Covino et al. 1996).

R_U	R_B	R_V	R_R	R_I
8.4 ± 0.4	6.5 ± 0.3	5.5 ± 0.2	4.9 ± 0.2	4.5 ± 0.2

At the brightest level, the observed J flux was lower than the expected stellar photospheric flux. However, I note that T Cha has not been moni-
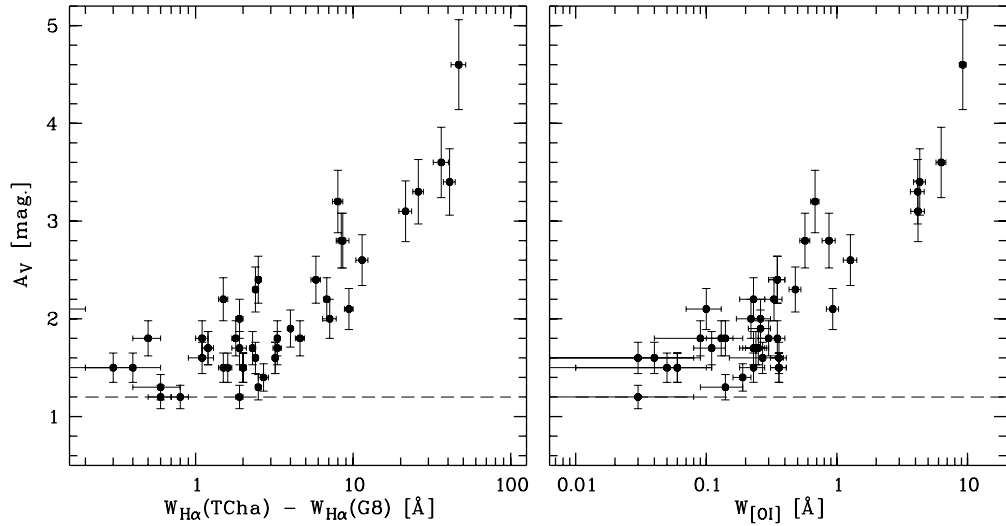
Figure 2.15: Visual extinction derived from low-resolution flux-calibrated spectra versus the equivalent width of Hα (left panel) and [O$\textsc{i}$] 6300Å (right panel) emission. For Hα, the abscissa refers to the net emission after subtracting a constant value corresponding to the photospheric absorption for a G 8 star. The horizontal dashed line indicates the minimum value of A_V obtained for T Cha at maximum brightness.
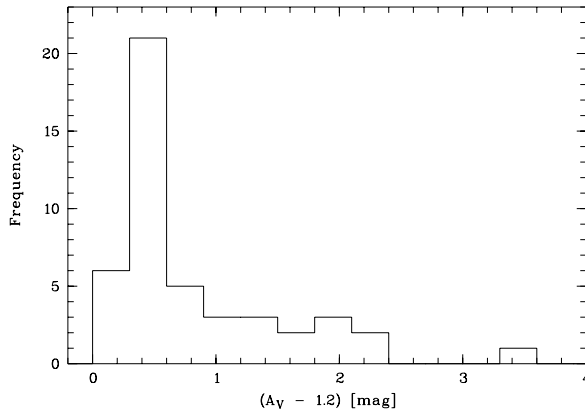
Figure 2.16: Histogram of differential visual extinction. The most frequent value is around 0.5 mag, while the maximum observed is 3.3 mag.
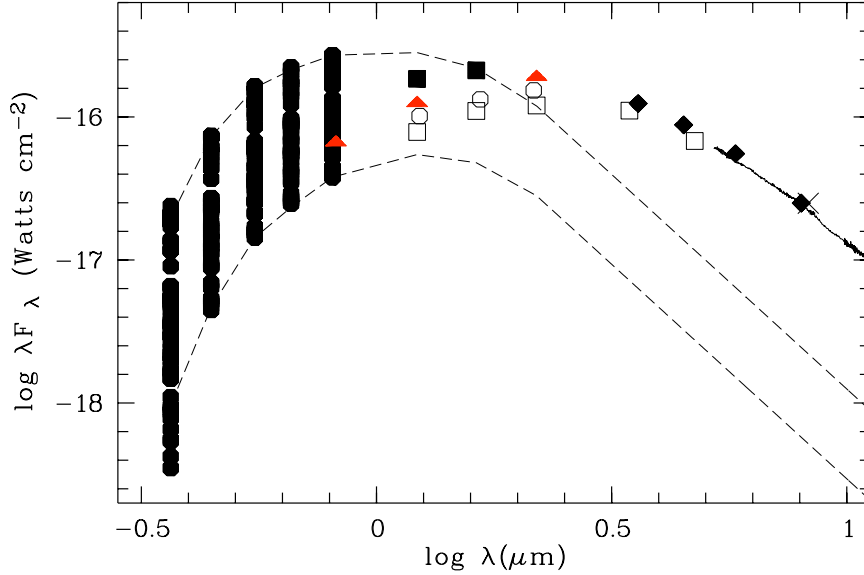
Figure 2.17: Observed SED of T Cha for $\lambda < 1\mu$m. The U,B,V,R,I data (filled circles) are from Alcalá et al. (1993); Covino et al. (1996). The IR fluxes come from different papers: Alcalá et al. (1993) (open squares), 2MASS fluxes (open circles), DENIS survey (filled triangles), Morel and Magnenat (1978) (filled squares), Spitzer IRAC bands (filled diamonds), MSX6C (crosses). IRS spectra are also superposed. The upper and lower dashed lines represent the SEDs of a G8 V standard, reddened to the corresponding $(B-V)$ values that match the brightest and faintest I-band observed fluxes, respectively.

tored as extensively in the near-IR as in the optical. Therefore, the available data probably did not detect the brightest J flux. For that reason, the J flux was excluded from the SED-fitting. Excess emission is instead observed for wavelengths longer than the H band. The agreement of the Spitzer spectroscopy with the photometric data in the mid- and far-IR (cf. Fig. 2.18) indicates that there is no significant variability at longer wavelengths. This is expected in the case that the strong brightness and colour variations affecting the star are due to variable extinction of the stellar photosphere from inhomogeneous, circumstellar material.

By assuming variable extinction, I used relationships derived from $UBVRI$ photometry (Covino et al. 1996) to probe the dust column af-

fecting the brightness of T Cha. In Table 2.5, I report the circumstellar extinction law for T Cha, expressed by the total to selective extinction ratios, $R_\lambda = A_\lambda/E_{B-V}$, derived from the differential brightness variations measured in the $UBVRI$ bands (Covino et al. 1996). The resulting value of R_V deviates from the normal value ($R_V = 3.1$) for the diffuse interstellar medium, which indicates different physical properties of the circumstellar grains. In particular, a higher value of R_V means a flatter extinction curve (i.e., greyer extinction), and reveals the presence of larger grains, thus implying probable grain growth and depletion of small grains (Draine, 2009).

Therefore, in the following SED analysis, I considered more suitable the flux measurements corresponding to the brightest level of the star, shown in Fig. 2.18.
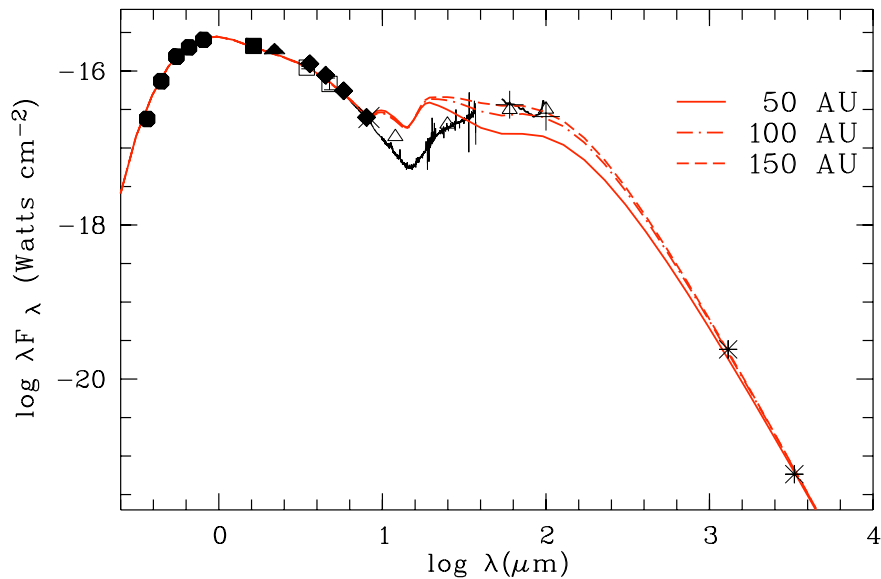
Figure 2.18: Observed data-points used for SED fitting. Optical: symbols as in Fig. 2.17; IRAS: open triangles. Also superposed are IRS spectra (thin line). Three disc models, whose parameters are reported in Table 2.6, are represented by the solid, dashed and dotted lines, for different disc radii.

Disc models such as those by Robitaille et al. (2006), .Robitaille et al. (2007) do not take account of the presence of a partially evacuated inner hole or gap, so may be inadequate in reproducing the SED of transitional objects such as T Cha. Brown et al. (2007) found that the mid-IR spectrum of

Table 2.6: Estimated stellarand disc parameters resulting from SED-fitting using Dullemond et al. (2001) model.

Stellar Parameter	value
L (L$_\odot$)	2.6[†]
T$_{\text{eff}}$ (K)	5520[‡]
R (R$_\odot$)	1.8[*]
M (M$_\odot$)	1.3[**]
Age (Myr)	10[**]
Model Disc Best-Fit Parameters	
L$_\star$ (L$_\odot$)	2.5
T$_\star$ (K)	5400
M$_\star$ (M$_\odot$)	1.5
M$_{disc}$ (M$_\odot$)	5×10^{-3}
R$_{out}$ (AU)	150
R$_{in}$ (AU)	0.13
Temperature of rims	1300
Inclination i	75º

[†] from SED integration and adopting d=100 pc and A$_V$=1.3; [‡] from the relations by Kenyon and Hartmann (1995) for a G8 V star; [*] from the Stefan-Boltzman law; [**] from comparison with Palla and Stahler (1999) PMS tracks.

T Cha can be reproduced by a disc truncated at 0.08 AU with a gap between 0.2 and 15 AU, but they did not consider the strong variability of the object nor use the available millimetre data.

We explored the possibility of modelling the SED, simultaneously from optical to millimetre wavelengths, using the CGPLUS prescription by Dullemond et al. (2001). Starting from the stellar parameters in Table 2.6, I constructed a grid of SEDs. The results of the SED fitting are reported in Table 2.6 and the best-fit models are overplotted on the observed SED in Fig. 2.18. The dust opacities calculated by Laor and Draine (1993), modified to match the Beckwith et al. (1990) opacity law at wavelengths longer than 100 μm were used. We note that a blackbody with T$_{\text{eff}}$ =5400 K better reproduces the optical data. Previous estimates of the disc mass based on single measurements at millimetre wavelengths are in the range of 3×10^{-3}– 1×10^{-1}M$_\odot$ (Henning et al., 1993; Lommen et al., 2007), but the estimate reproduces well the observed data for wavelengths longer than 60 μm. The disc radius is more poorly constrained, but values between 100 and 150 AU

provide quite reasonable results. The latter is consistent with the 3.3 mm observations by Lommen et al. (2007) that did not resolve the disc around T Cha. We note that the disc radius adopted by Brown et al. (2007) is a factor of two higher than the value derived here.

Although the model with a disc radius of 150 AU reproduces well the observed SED at optical, far-IR, and millimeter wavelengths, all the models predict too high flux between 10 and 30 μm relative to the observed SED. Thus, despite the attempt to minimize the effects of colour changes by adopting the brightest flux level in each band, I were unable to fit the complete SED of T Cha with a simple reprocessing-disc model. This failure is probably caused by excess emission in the near-IR. Therefore, the most plausible disc model for reproducing the SED of T Cha is a disc with a gap, as proposed by Brown et al. (2007).

2.9 Discussion and conclusions

Before discussing my interpretation of T Cha, I briefly summarise the most significant properties of the star derived from analysis of the spectroscopic observations presented here, complemented with published photometry and other data from public archives:

a) I confirmed the spectral type G8 and a lithium abundance indicative of a very young age.

b) I detected RV variations of almost $10 \, \mathrm{km \, s^{-1}}$ on relatively short timescale, but did not find any clear periodicity that could be related to orbital motion. Besides that, the $v \sin i$ determinations obtained from FEROS observations are consistent with the value of $37 \pm 2 \, \mathrm{km \, s^{-1}}$, except for a few spectra in which the photospheric lines are significantly narrower, yielding a $v \sin i$ of $30 \pm 2 \, \mathrm{km \, s^{-1}}$.

c) strong variability in the main emission features (e.g., Hα, Hβ, and [O I] lines) on timescales comparable to that of photometric variability, and a close correlation between the Hα and [O I] line intensities are found.

d) variations in the photospheric continuum slope are observed in connection with intensity changes in the main emission features (i.e., the line intensities strengthen when the star reddens and fades).

e) clearly evident relationships between brightness and colours based on optical photometry (Alcalá et al., 1993; Covino et al., 1996) have allowed to derive a circumstellar extinction law characterised by $R_V = 5.5$ and infer the presence of large circumstellar dust grains.

f) the observed SED, showing a dip at mid-IR wavelengths, is typical of a transitional disc. SED modelling has confirmed the presence of a disc with

a gap and a high inclination angle, as first indicated by Brown et al. (2007).

Several of the properties outlined above provide clues (e.g., items *c*, *d*, and *e*) that a mechanism of variable circumstellar extinction is most probably operating in T Cha, as in UX Ori-like stars (Natta et al., 2000; Rodgers et al., 2002). The simultaneous brightening of Hα emission and oxygen forbidden lines as reddening increases, as well as the existence of a tight correlation between brightness and colour variations, can be most plausibly explained in terms of variable extinction produced by obscuring clumpy material moving across the line of sight to the star. First of all, whereas the Hydrogen Balmer lines originate in regions closer to the star, the oxygen forbidden lines form instead farther away from the star and are hence not expected to be sensitive to variations occurring in the inner parts of the disc. Moreover, the dominant timescales and ranges of the observed variability phenomena indicate that the occulting clumps must be small compared to the size of the disc and more likely concentrated within a distance of a few tenths AU from the star. These clumps occasionally obscure the star favoured by the high inclination of the disc, while not affecting either the outer, extended, low-density wind region traced by the [OI], or the bulk of the circumstellar hydrogen emitting zone. The consequence is a strong contrast enhancement of all emission lines relative to the photospheric continuum when the star is highly attenuated, while the lines weaken or even disappear as the photospheric contribution turns brighter. Furthermore, these dusty clumps might also be associated with patchy gas structures orbiting close to the star ($\lesssim 0.2\,\mathrm{AU}$) that cause daily changes in the Hα line profile, similar to those I observe (see Sect. 2.5.3), due to variations in the absorbing column of material shielding the star. If the Hα variability were merely a consequence of the brightening and fading of the stellar continuum flux, the shape of the line profile should not change with time. This is generally not the case, suggesting that some other modifications in the Hα forming region must also intervene. In particular, I expect that the parts of the Hα profile originating closer to the star (e.g., the redshifted absorption components, in the case of magnetospheric accretion) also show the effects of occultation by orbiting material as well as eventual modulation induced by rotation. This is consistent with the nightly line profile changes seen in the FEROS high-resolution spectra and the continuum flux (i.e. extinction) variations sharing a common timescale. However, while I can estimate that the time required for an occulting clump to appear in front of the star likely ranges between about one-third and two-thirds of a day, it is difficult, from the present data, to quantify in a reliable way the fraction of Hα emission that may originate close to the star, as it is not possible to determine the detailed geometry of the occultation.

But what is the source for the bulk Hα emission in T Cha? It is generally

accepted that the strong Hα emission line in T Tauri stars is due to mass accretion, which leads to UV excess emission and photospheric continuum veiling (Hartigan et al., 1989). Transitional objects, however, have more evolved discs in which accretion should decrease significantly with respect to the earlier CTTS phase. In T Cha, no veiling is apparently detected, not even in the stages of strong Hα emission (see Figs. 2.5 and 2.19) suggesting very low or no mass accretion. However, the non-detection of veiling in T Cha may also caused by the relatively high continuum flux emitted by its G8 photosphere. Hence, I cannot exclude the possibility that erratic accretion episodes are caused by instabilities in the inner disc, in which infalling gas produces the variable redshifted absorption features, observed in the Hα line profile. However, the [OI] $\lambda 6300$ Å emission, which corresponds to a luminosity of $\log(L_{[\text{O I}]}/L_\odot) \approx -4.8$, implies the presence of strong winds, although the width of the line ($\approx 100 \, \text{km s}^{-1}$, see Fig. 2.6) is at the lower limit of a typical high-velocity component (Hartigan et al., 1995). It is probable that the bulk of the Hα emission observed in T Cha is also produced in a wind, as reported for some Herbig Ae stars (Kraus et al., 2008). Moreover, the Hα versus [OI] correlation shown in Fig. 2.7 is more easily explained in terms of variable circumstellar extinction, rather than variable accretion.

By both assuming variable circumstellar extinction, and adopting the relation $A_V = 1.086 \, C_{ext}(V) N_H$ and the extinction cross-section per H nucleon for $R_V = 5.5$, $C_{ext}(V) = 6.715 \times 10^{-22} \text{cm}^2/H$, given by Draine (2003), I estimate the column density for an obscuring clump to be $N_H \approx 1.4 \times 10^{21} A_V \, \text{cm}^{-2}$. By also assuming the maximum observed differential extinction of 3.3 mag, I obtain a hydrogen column density $N_H = 4.6 \times 10^{21}$ cm^{-2}. We can estimate the mass of the obscuring clumps, M_{cl}, by assuming that they cover completely the photospheric disc of the star. Using the stellar radius reported in Table 2.6, the result is $M_{cl} \approx 4 \times 10^{20} \, \text{g}$, i.e., of the order of $2 \times 10^{-13} \, \text{M}_\odot$. Similarly, assuming the most frequent differential circumstellar extinction from the histogram in Fig. 2.16, the result would be $M_{cl} \approx 3 \times 10^{-14} \, \text{M}_\odot$. In contrast, the mass of asteroid 253 Mathilde is $5 \times 10^{-14} \, \text{M}_\odot$ (Yeomans et al., 1997).

Finally, could the RV variations in T Cha becaused by a low-mass companion? Some PMS stars with transitional discs, such as CoKu Tau/4, have been discovered to be binaries (e.g., Ireland and Kraus, 2008). The inner edge of circumbinary discs is believed to be set by dynamical truncation. In the case of CoKu Tau/4, where the binary separation is about 8 AU, the truncation radius would be of the order of 13-16 AU, depending on the eccentricity of the binary (Ireland and Kraus, 2008). As concluded from the analysis of the CCF bisector, the RV variation of T Cha is about $10 \, \text{km s}^{-1}$. A very low-mass object, say a $0.05 \, \text{M}_\odot$ brown dwarf on a circular orbit with a radius

of about 0.1 AU may cause this variation, producing a disc truncation radius of about 0.2 AU, consistent with the inner disc edge proposed by Brown et al. (2007). However, no obvious periodicity is detected in the RV measurements. On the other hand, the gap proposed by Brown et al. (2007) cannot be explained in terms of truncation by a companion at a separation of about 10-15 AU. At such separation, a $0.9\,\mathrm{M}_\odot$ star would be necessary to produce the observed RV variation. An object of that mass and separation would have been eventually detected either as a spectroscopic binary, or by Köhler (2001) in his *speckle* survey. Thus, the gap of the transitional disc in T Cha is probably not the result of dynamical truncation due to a binary companion. In any case, the presence of a lower-mass (stellar or substellar) companion cannot be definitely excluded because a quasi-periodicity of about 3 days is clearly evident throughout the entire data-set of T Cha. On the other hand, T Cha is a relatively fast rotator ($v \sin i \approx 37\,\mathrm{km\,s^{-1}}$) and a magnetically active ($\log L_X \approx 30\,\mathrm{erg\,s^{-1}}$) PMS star. Therefore, the observed RV variations might be alternatively induced by stellar spots, as in the case of the WTTs V410 Tau (Steltzer et al., 2003). Otherwise, I cannot exclude the possibility that the same circumstellar inhomogeneities responsible for the variable extinction may also alter the symmetry of the photospheric lines, and cause apparent RV shifts due to a sort of Rossiter effect, as in eclipsing binaries, which occurs when the stellar photosphere is partially obscured. In all cases, the presence of an inner disc characterised by a clumpy structure and the evidence of grain growth both indicate that T Cha is a likely candidate to host planet formation.
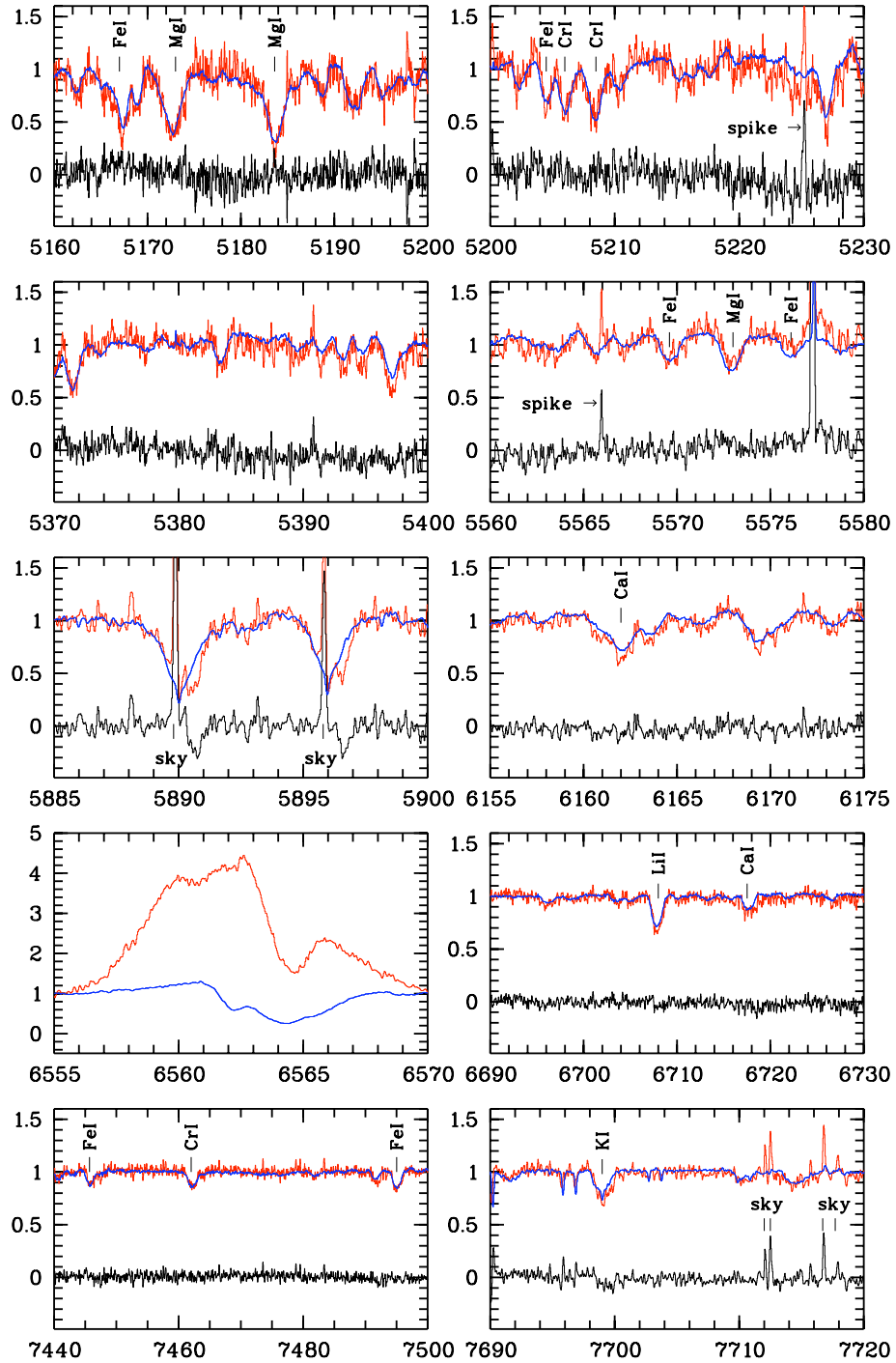
Figure 2.19: Comparison between T Cha spectra observed in two different epochs: in blue the spectrum observed on 14 Feb 2002, in red the one observed on 26 Apr 2004, in black the difference between the two. Various spectral lines at different wavelengths are marked.

Chapter 3

The effects of YSO parameters on [Ne II] diagnostic lines

3.1 Introduction

Young solar mass stars are generally surrounded by dust and gas distributed in a circumstellar disk which is the birthplace of planetary systems. The dust is easier to observe due to its higher contribution to the opacity respect than the gaseous component. However, the gas dominates the mass of circumstellar disks, determining the density structure and influencing all dust dynamic and at last the formation of the planets. In fact, the evolution of the gaseous phase has important role in the formation of gas-rich or gas-poor planets (Gorti and Hollenbach, 2004). For example, the gas dispersal can drag away small dust particles before they could grow up further or, in case that enough massive cores were already formed, can prevent the accretion and the formation of giant planets like Jupiter or Saturn, setting an upper limit on the giant planet formation (Zuckerman et al., 1995). On the other side, the gas evaporation combined with the dust settling can increase the dust-to-gas ratio in the disk midplane until gravitational instabilities can be triggered (Youdin and Shu, 2002), favouring an alternative way to form planets than the core accretion theory[1] (Bodenheimer et al., 2000; Pollack et al., 1996). Moreover, the presence of gas in a planet hosting circumstel-

---

[1]The core accretion theory predict the formation of a gas giant planets by a two-stage process after the dust coagulation in planetesimals within the disk. In this theory first it is formed a core of mass of about ten earth masses by collisions between planetesimals, then gas is accreted on the core increasing his mass as the gas cools and contracts onto it. After a critical core mass, beyond which a hydrostatic envelope cannot be maintained, a gas runaway growth is triggered building up the gaseous planet extremely fast until the supply of gas is terminated.

lar disk has strong influence on the final apparence of the planetary system once the disk is dissipated (Kominami and Ida, 2002), since the intial orbital radius can be altered (orbital migrations) by the gas-planet interactions (Bodenheimer and Lin, 2002; Ward, 1997).

Although fundamental to answer questions about planet formation, the properties of the gaseous phase are also relevant to understand the nature of the physical mechanisms responsable for the disk accretion. During the accretion most of the disk mass is accreted on the central star, while the angular momentum is transfered to a small fraction of particles toward large radial distances. Such momentum trasport needs the presence of a viscous force, a friction able to dissipate the energy locally to have an inward net motion of mass (Papaloizou and Lin, 1995; Pringle, 1981). The rate of such transfering controls the evolution of the star-disk system. However, it is not clear what is the dominant contribution to such viscosity. This ignorance is usually overcame adopting a parametric formulation for the viscous force through the use of an "α" parameter (Pringle, 1981; Shakura and Sunyaev, 1973) tuned by comparison with the observation. Nevertheless, several theories try to explain the viscous force from basic principles. The most favoured mechanism is the "magneto-rotational instability" (MRI) (Balbus and Hawley, 1991, 1998), active in a large portion of the disk, producing an efficient α-type viscosity able to drive the disk accretion[2]. However, to make MRI work it is necessary that the magnetic field couples tightly with the gas, thus its efficiency strongly depends on the amount of ionized gas present in the disk. In the cold disks around young stars the ionization fraction is believe to be quite low (Gammie, 1996), but in the inner region regions ($R \lesssim 10$ AU) of these disks the UV and X-Ray radiation fields form photon dominated regions on the surface layers of the disk. The high number of electrons and low-ionization potenzial ion can provide the MRI to operate.

Thus, to further improve the knowledge of star and planet formation is extremely important to study also the disk gaseous phase characterizing its dynamical state, physical and chemical (temperature / abundances) structures, its evolution and interaction with the short-wavelength radiation (from UV to X-rays).

In this chapter I review briefly the topic of of the gaseous disks, intro-

---

[2]Without entering in detail the MRI, known also in literature as the Velikhov-Chandrasekhar instability or Balbus-Hawley instability, predicts that a weak axial magnetic field is present in the disk. Such magnetic field acts as a connecting spring on close disk annuli. In a keplerian disk the inner regions rotate faster than the outer ones, stretching the springs. The restoring forces hence speed up the outer disk, increasing their angular momentum and moving to higher orbit, while slow down the inner disk, moving therefore to lower orbits.

ducing typical observational diagnostics, and then focusing on the neon fine structure lines, predicted in the theory of high energy irradiated disks and observed by *Spitzer* space telescope. The mean observed luminosity of [Ne II] 12.81 μm line revealed to be comparable to the predicted value from the models, but the scatter of the observed values around this mean spans over three orders of magnitude (Güdel et al., 2009). If the [Ne II] line is to be used as a useful diagnostic of the gaseous phase of the inner disks its origins must be well understood. In the next sections I descrive the work performed to justify the spread of the observations luminosities in the current theoretical framework. Such work as been published in E. Schisano, B. Ercolano and M. Güdel, *Monthly Notices of the Royal Astronomical Society*, Volume 401, Issue 3, pp. 1636.

3.1.1 The gaseous disk

For a typical disk, the temperature structure of the gas in its interior, closer to the midplane, up to vertical column densities of $A_V \sim 1$ (Dullemond et al., 2007), follows the one of the dust, determined through SED modelling (D'Alessio et al., 1998). In fact for such densities the dust and the gas are thermodynamical equilibrium, but at higher heights the density and the temperature decrease and the gas decouples from the dust, becoming an indipendent phase. Gas temperature can be at higher or lower temperature than the dust, depending on the heating and cooling processes in act that are at the same times influenced by the density, the chemistry, the temperature and the radiation enviroment. When the heating processes by stellar and external irradiation (including high energetic far UV and X-rays), by viscous accretion and by grain photoelectric exceed the cooling by dust-gas collisions and by recombination lines (forbidden, fine structure, rotational and rotovibrational lines) the gas temperature increase respect the dust one, forming an inversion region in the disk "cromosphere", able to producing many emission lines (Glassgold et al., 2004).

So the full self-consistent treatment of the gaseous disk atmosphere in the inner disk requires complicated modelling and only recently progresses are been made with the publication of different models (Glassgold and Najita, 2001; Glassgold et al., 2004; Gorti and Hollenbach, 2004; Jonkheid et al., 2004; Kamp and Sammar, 2004; Kamp and van Zadelhoff, 2001; Nomura and Millar, 2005; Semenov et al., 2004). Even if such models are based on simple assumptions like chemical, thermal and hydrostatic equilibrium, the overall picture is that the vertical stratification of the gaseous disk composed, moving from the midplane toward higher heigths, by a cool molecular layer, then a warm ($\sim$ 500-2000 K) partially molecular layer, a partially hot ionized

atomic layer and an X-Ray irradiated high temperature ($\sim$ 5000 K) and a fully ionized (HII) EUV-irradiated layer (T $\sim 10^4$ K).

3.1.2 The disk gaseous component diagnostics

Emission lines of atomic and molecular species are widely used as gas-phase probes of the inner disk region (Najita et al., 2000, 2007a). Even if high spatial resolution spectroscopy in sub-mm/mm range is still challenging and optically thin lines in mid infrared are often faint, several observations have detected the fundamental and the overtones transitions of CO, the H_2O infrared rotovibrational transitions, the OH molecular emission and the H_2 UV/infrared transitions in many young stellar objects (Carr and Najita, 2008; Herczeg et al., 2002, 2005; Lahuis et al., 2006; Najita et al., 2003, 2000; Salyk et al., 2008). The formation of an emission line requires that the atoms/molecules get excited to higher states and remain in such state until they radiatively decay. The excitation can be due to collisions with other particles, typically electrons in thermal motions, in low density regions and, in some cases, to not-thermal processes induced by the UV and/or X-Rays fields. The amount of energy emitted at line wavelength is proportional to the number of excited atoms/molecules, the latter depending on the density and temperature condition of the emitting layer. The observed lines are excited by different temperature, so they probe various regions of the disk, ranging for example from the warm temperature ($\sim$ 2000 K), closer to the star and up in disk atmosphere, needed for CO overtones formations to the low temperature ($\sim$ 100K) for pure rotational H_2 transitions. The emission line fluxes are interpreted in the framework of a model for the thermal, chemical and excitation structure of the gas.

Such models are computed determining disk parameters from other diagnostic tools, like the spectral energy distribution.

With the improvement of the models new lines are proposed as diagnostic, expecially to probe the characteristics of the surface layers exposed to the UV/X-Rays radiation field. The recent infrared observations carried out expecially by *Spitzer* space telescope encouraged a detailed study on the atomic fine structure lines emitted by the heavy elements (and their ions). Those theorical works pointed out the importance of the Ne (Glassgold et al., 2007), C, S, O, Si, Fe lines (D.Hollenbach and Gorti, 2009; Gorti and Hollenbach, 2008; Hollenbach and Gorti, 2004; Meijerink et al., 2008), confirmed by the detection of the stronger ones in a significant sample of circumstellar disks (Güdel et al., 2010; Lahuis et al., 2007; Pascucci et al., 2007). In particular great efforts either on the observational side and the theoretical one are involved in the study of the Ne emission lines as a probe of the effect of

the high energy radiation on the inner disk.

3.1.3 The Neon lines

The neon fine structure emission lines has been firstly suggested by Glass-gold et al. (2007) as a potential new probe of the planet formation region of circumstellar disks. The study of neon lines offers a lot of advantages, the most important ones are the relative high abundance in gas phase and the easiness of the modelling. In fact, since neon is present exclusively in atomic form and has a simple chemistry, the models do not require complex chemical networks. Their sensitiviness to the low column density region makes neon lines are also a powerful diagnostic expecially of the higher heights of the disk as well as for the unbound disk regions subjected to the photoevaporation. The infrared line [Ne II] 12.81 μm has been detected from space, with the *Spitzer* Infrared Spectrometer (IRS) (Espaillat et al., 2007; Lahuis et al., 2007; Pascucci et al., 2007), and from ground, with MICHELLE and TEXES at Gemini North (Herczeg et al., 2007; Najita et al., 2009) and with VISIR at VLT (Boekel et al., 2009; Pascucci and M.Sterzik, 2009). Actually there are ~ 50 of young systems, mostly with a strong infrared excess emission indicative of a circumstellar disk, with confirmed Ne II]. Glassgold et al. (2007) predicted also that the [Ne III] 15.55 μm should be observable, but due to lower abundaces of two-times ionized neon, it should be fainter than the [Ne II] 12.81 μm by a factor of ten. In fact only one detection of the [Ne III] was found so far. Even if the detection of those two lines represent a success, it is not fully understood how to use them to determine physical properties of the gaseous disk due to controversies on where the lines form, which is the main contribution to the disk heating there and, mostly, the source for the Ne ionization and for the excitation of its fine structure lines.

The [Ne II] 12.81 μm and the [Ne III] 15.55 μm lines are M1 transitions, corresponding, respectively, to $^2P^0_{\frac{1}{2}} - {}^2P^0_{\frac{3}{2}}$ and $^2P_1 - {}^2P_2$, linking each ion ground state to the closest fine structure upper level. The energies of the two transitions are $\Delta E = 0.097$ eV, for [Ne II], and 0.079 eV, for [Ne II], hence they require a temperature T$\gtrsim$ 1000 K to be excited. However, due the relative high ionization potential of Ne$^+$ (21.6 eV) and Ne^{++} (41.0 eV), the iones requires temperature of few 10^5 K to be thermally formed, but they can exist in the photoionized gas present in the bounded inner disk surface (Ercolano et al., 2008a; Glassgold et al., 2007) or in the photoevaporative flows (Alexander, 2008). In either cases, [Ne II] line could provide an indirect measure for the density and the temperature of the gas, but it would trace two differ-ent enviroments with diverse dynamic and scientific revelance. The inferred

temperature and densities, in the first case, allow direct investigation on the planet formation enviroment and to the mechanism of accretion through the disk, in the second case are linked to the efficiency of photoevaporation on the gaseous disk evolution.

Even if one assumes that the neon emission belong to the disk, there is a debate on which layer of disk atmosphere dominate the emission, because Ne can be ionized throught two different ionization path. In fact the ionization can be induced by the direct photoinozation by EUV photons, whose wavelengths is shortward of the ionization edge at λ 575 Å, equal to 21.56 eV, or by a K-shell absorption of X-Rays with energies $\gtrsim$ 0.9 keV with the knokback and ejection of one electron. In the first case, since the EUV photons are absorbed very efficiently by hydrogen, the line emission is dominated by the HII-like photodissociated layer, while in the second case larger fraction of the disk atmosphere are involved. Whatever of the two paths is the main source of produciton of Ne^+ ions, the interpretation of the observed [Ne II] line luminosity differs. In fact, D.Hollenbach and Gorti (2009) suggested that if EUV irradiated layer dominate the emission the line is insensitive to plasma density and temperature, but it can be used as a probe for the EUV photon luminosity Φ_{EUV}, generally extremely uncertain. In the two cases the involved main gas heating mechanism is rather different; in the first case it is produced by the photoelectric effect over small grains or the PAH[3] heated by UV radiation (Gorti and Hollenbach, 2009) while, in case of X-Rays, by thermalization by collision of the high velocity electrons produced by Auger effect or by K-shell knockback from X-Ray photons. Such mechanisms imply different heating efficiency that has to be taken into account when modelling the disks temperature structure, with implications on the planet formation in the inner disk.

Finally den Ancker et al. (1999) suggested that neon is ionized and excited by the dissociative J-type shocks present in (star) wind-disk interaction zone. Such possibility has been excluded by some recent models, suggesting that the internal shocks in the wind are too weak to ionize the specie (D.Hollenbach and Gorti, 2009), however in case of strong wind it should not be ruled out.

Observations should help to define which case descrives better the enviroment of the circumstellar disk around a typical young star. The sample is still small, but it seems that the mean observed line luminosity of 10^{-5} $L_\odot$ have a good agreement with the models where X-Rays act like the main source of disk heating and line excitation. If the line is formed in the disk by irradiation of the gas by X-rays from the central star then one naturally

---

[3]Polycyclic aromatic hydrocarbons are organic molecules that are flat (few atoms thick < 10 Å) detected in the hot regions of space where stars are born.

expects to find a correlation between line luminosity and X-ray luminosity for the observed sources. Such correlation is indeed observed by Pascucci et al. (2007), on a rather small sample, and then confirmed by Güdel et al. (2010). However such studies that for objects with the same X-ray luminosity the [Ne II] line luminosities span over at least one order of magnitude. More, the observed values scatter around the $L_{[Ne\ ii]}$ mean in a range covering about three orders of magnitude, $10^{-4} - 10^{-6}$ $L_\odot$ (Güdel et al., 2010; Lahuis et al., 2007), arguing against the revelance of X-Rays as main drive. On the other side, Espaillat et al. (2007) reported a correlation between $L_{[Ne\ ii]}$ and the accretion rate, thus sustaining the thesys that the main heating/ionizing agents of the disk surface is the EUV radiation produced by the accretion shocks, rather than stellar X-rays.

On other side there is the possibility that the Ne emission is not produced in the disk. Boekel et al. (2009) observed, in the case of T Tau, an extended [Ne II] emission associated not with the circumstellar disk but with the outflow present in the system. Indeed, it is generally found that sources with outflows have high $L_{[Ne\ ii]}$ Güdel et al. (2010), suggesting that a contamination from outflow emission is possible. Such fact is indeed confirmed by the observations with ground instruments, performed at higher resolution and with narrower slits. First indication is few cases indicate that the neon disk emission is around one third of the overall line fluxes observed by *Spitzer* satellite (Herczeg et al., 2007; Najita et al., 2009; Pascucci and M.Sterzik, 2009).

All those observations indicate that the [Ne II] line formation in young star is rather complex argument. Mostly in the framework of the X-Rays irradiated disks, one of the most favourable models to explain the neon emission, it has to be addressed the problem on the observed scatter in the luminosities. Understanding what is producing such scatter in the data as well as various correlations is extremely important to improve the modelling and to adopt such line as useful diagnostic. A possible answer to such issue is that intrinsic disk properties, like the presence of disk holes or different degree of flaring, not considered in earlier models have an effect on the [Ne II] emitting region, hence on overall luminosities. Once setted those issues, one more relevant question to answer is whether the [Ne II] line originates in the bound layers of the disk irradiated mainly by X-rays or whether it includes a contribution from a photoevaporative outflow (Alexander, 2008). In this sense future high-resolution spectra will be fundamentals to distiguish between the ordered flow, present in a "disk - wind" scenario, from the spreading due to the keplerian rotation and the turbulence in the case of a bound upper disk atmosphere.

3.2 The system modelling

In this work, I assumed that the emission of Ne takes place in the upper circumstellar disk atmosphere irradiated by an high energy (UV+X-Rays) spectrum. The aims are multiple: 1) to address that the X-Rays are the main contributers to the ionization and excitation of the neon fine structure line, 2) to explore the possibility that the scatter observed in [Ne II] line luminosities for a given X-ray luminosity, that is the principal observative argument against the X-Ray cause, may be due to further properties not included in previous modelling, 3) to determine observative properties, like line profiles and their width, to be compared with current and future to high resolution observations (Herczeg et al., 2007; Najita et al., 2009; Pascucci and M.Sterzik, 2009). In particular, I have verified the effect of details of the irradiating field and of the disk structure (i.e. degree of flaring) on the observed luminosities and line of profiles of neon.

To reach this aims I had to model the density-temperature structure of an high-energy irradiated disk, solving autoconsistently the neon ionization and the statistic equilibrium in each region of the disk. Different approach exist in literature, but so far no code includes all the important physic and chemistry to exactly solve such problem. Moreover, most of the works available so far are based on 1D or 1+1D models and only recently, see Ercolano et al. (2008b, 2009), multidimensional calculations were carried on thanks the introduction of 2D and 3D codes. Following such approach, I have used the montecarlo radiative transfer code MOCASSIN to compute the thermo-chemical structures of different models and their [Ne II] line luminosities. From those solution, adopting the hypothesys of a keplerian rotating disks, I have computed the line profiles in the case of different irradiating spectra. In this section i descrive briefly the MOCASSIN code, the details of the models built, the high energy irradiating sources and the disk models, and the adopted processes to compute the line profiles.

3.2.1 Brief description of the code MOCASSIN

MOCASSIN (MOnte CArlo SimulationS of Ionized Nebulae) is a three-dimensional radiative transfer code based on the principle of locally simulating the processes of ionization and recombination and heating and cooling (Ercolano et al., 2008b). The simulated region is approximated by a three-dimensional cartesian grid. The radiation field is expressed in terms of energy packets, used as 'quanta' for the calculation. Such packets are created at the position of the high-energy source in the grid and a launched in the outward radial direction. The code computes the each

packet trajectory through the density distribution simulating the absorption and re-emission events depending on the optical depth and the emissivity of the gas. During such processes they alter the local radiation field along a specific direction, as packets are scattered away or inside it, and they influence the physical properties of each grid cell. At each location thus the properties must be determined by solving the ionizations balance and thermal equilibrium equations, which are coupled through the electron temperature and density and the radiation field across the cell. The solution is found iteratively, determining at each step the local radiation field and the physical properties, until the convergence is achieved on all the cells of the grid. In such way MOCASSIN gives in output not only the emerging spectrum by the sums of all the energy packets reaching the outer bounds of the grid, but also the line emissivities corresponding to the derived physical conditions (e.g.ion fractions, electron temperatures and densities) at each grid point. Moreover, one of the output of MOCASSIN is the the density and temperature structure altered by the radiation field.

One of the features included the version of MOCASSIN I have used is the possibility to use a routine to include the self-consistent calculation of the one-dimensional vertical hydrostatic equilibrium structure. Starting from the initial density distribution the code is able at each iteration to compute the new density structure for the gas compatible with the calculated temperature structure starting from the height on the z-axis, z_{dec}, where the gas and dust temperatures become decoupled. In such way the density profile below this point is unaltered, taking into account the (not included in the source irradiation omdel) effect of the stellar photosphere heating. The new density profile is given by the solution of

$$\rho(z) = \rho_{z_{dec}} \frac{T_{z_{dec}}}{T(z)} e^{-[\frac{m_H \frac{GM_\star}{k_B}} \eta(z)]} \tag{3.1}$$

where $\rho_{z_{dec}}$ and $T_{z_{dec}}$ are the density and temperature at the lower boundary, m_H is the hydrogen atomic mass, G is the gravitational constant, $M_\star$ is the mass of the central star, k_B is the Boltzmann constant and $\eta(z)$ is defined by:

$$\eta(z) = \int_{z_{dec}}^{z} \frac{\mu(z)}{T(z')(z^2 + r^2)^{\frac{3}{2}}} dz' \tag{3.2}$$

with z and r the cylindrical coordiante and $\mu(z)$ the local molecular weight (Alexander et al., 2004; Ercolano et al., 2009). An example of the results of the routine is shown in figure 3.1
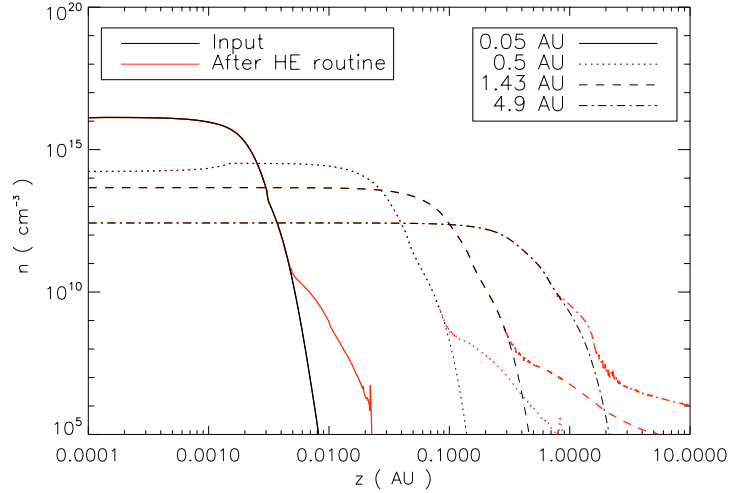
Figure 3.1: Example of the routine to compute the new hydrostatic equilibrium. Higher layers are warmed to higher temperature with the result that the disk puff up.

3.2.2 The X Ray spectrum model

The models were irradiated with synthetic spectra extending from the EUV to the X-Ray spectral region (13.6 eV-10 keV). Stellar and interstellar radiation transfer are not included in those simulations, since they will increase the computational time and will influence mostly the dust temperature structure. Those effects are taken into account in the the initial disk model, see section 3.2.3. In the young stars, the high energy photons are mostly emitted by the high temperature plasma magnetically confined in the cromosphere and the corona. In the case of the actively accreting T Tauri stars, the emitting plasma is confined in accretion columns, that drive the matter from the inner disk edge to the star. However, the physical properties of those dense accreting columns are strongly uncertain, so for the aim of this work I have only simulated the case to an high energy emission arising from a optically thin plasma, like a star chromosphere/corona. I have followed Ercolano et al. (2008a) and Ercolano et al. (2009) to obtain the irradiating spectra.consisting in an Such spectra are computed using the PINTofALE
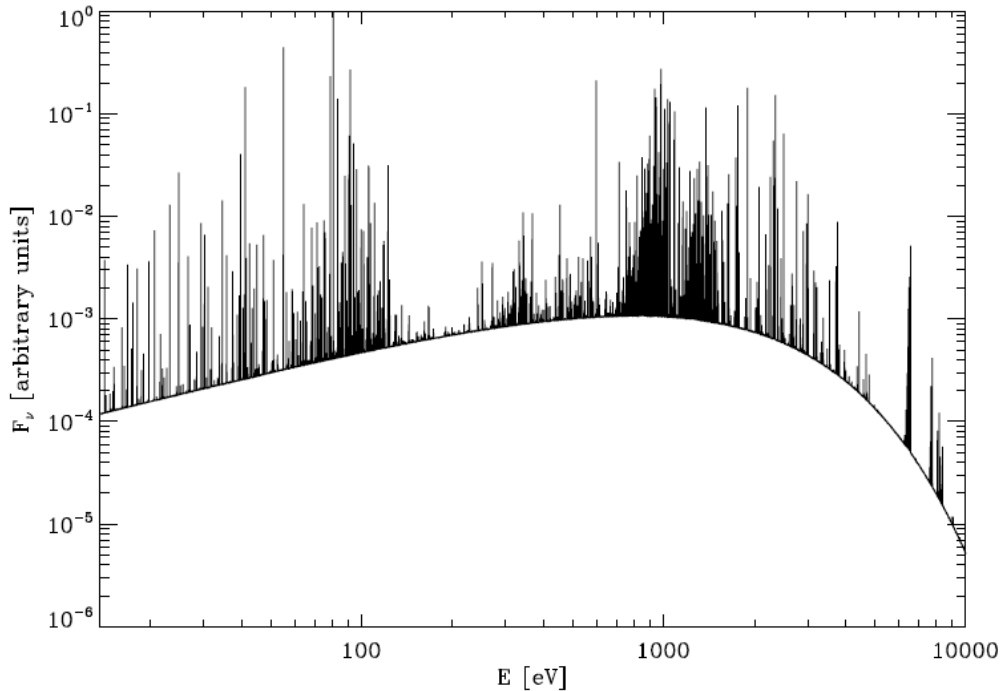
Figure 3.2: Single temperature (T = 1.6×10^7 K) X-Ray spectrum adopted as exciting source in the simulations with only X-Ray (see text below).

IDL software suite (Kashyap and Drake, 2000), adopting the solar chemical composition (Grevesse and Sauval, 1998). Lines and continuum emissivity for the first 30 elements are taken into account adopting the atomic data from the CHIANTI compilation (Landi and Phillips, 2006) and the ion populations from Mazzotta et al. (1998). Two different kind of models are computed: a single temperature isotermal spectrum with $\log T_X = 7.2$, simulating the X-Ray spectrum for a typical T Tauri, and a multi-temperature distribution to simulate also the lower energy (EUV+very soft X-Rays in the 0.1-1 keV energy range) contribution. The unabsorbed emitted spectrum in such energy range is hard to constrain from observations for young stellar object, since it is rapidly absorbed by the circumstellar matter. For this reason, following Ercolano et al. (2009), I have adopted the temperature distribution from the satellite observation of RS CVs binaries[4] (Sanz-Forcada et al., 2002)

Figure 3.2 and 3.3 show the two different initial irradiating spectra. How-

---

[4]The RS Canum Venaticorum are late-type, evolved (spectral type K) stars found in binary systems. They have high magnetic activity due to the presence of an intense dynamo effect produced by the coupling of an high rotation, inducted by the tidal interaction with the companion, with deep convection zone.
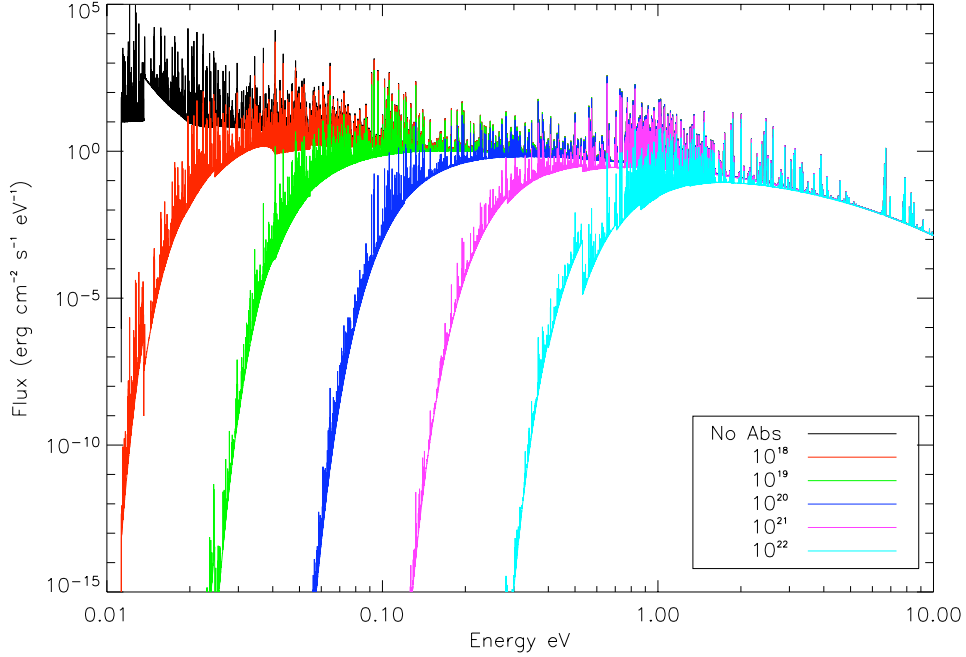
Figure 3.3: Multi-temperature spectra adopted as exciting source in the different models (see the text below). In black the whole high-energy spectrum built with a temperature stratification. In different colors the emergent spectra after the absorption by various column densities 10^{18} (*red*), 10^{19} (*green*), 10^{20} (*blue*), 10^{21} (*magenta*), 10^{22} (*pink*) cm^2.

ever, the presence of matter in the circumstellar enviroment really close to the star can influence the effective spectrum irradiating the disk surface, so different irradiating spectra were computed from multitemperature spectrum simulating the absorption of the high-energy photons by the screens of various thickness (Ercolano et al., 2009). I have determined the neon line emissivities in each case of the irradiating spectra shown in Figure 3.3, obtained after the the attenuation by photoelectric absorption by neutral hydrogen column densities of $10^{18}, 10^{19}, 10^{20}, 10^{21}, 10^{22}$ cm^{-2}. The hardness[5] of the irradiating spectra increases with the increasing column density of the inner screen as the less energetic radiation is more effectively absorbed. With such choise of irradiating spectra it is possible to investigate the contribution of the photons of different energy to the resulting neon line luminosity. I have thus

---

[5]In this case the the hardness of a spectrum is defined as the ratio between the emission at high energy (few keV) and the one at lower emission (few hundeds eV).

normalized the irradiating spectra to have an integrate luminosity between 0.1 and 10 keV equal to $L_X(0.1-10 \text{ keV}) = 2 \times 10^{30} \text{ erg s}^{-1}$, compatible with the mean emission of solar mass stars.

Observations of clusters indicate that the total luminosity of the high-energy portion of the spectrum emitted by a young solar mass star has not a well defined value and change with time. Several surveys conducted at the X-Rays wavelengths region (Feigelson et al., 2005; Güdel et al., 2007; Preibisch et al., 2005; Telleschi et al., 2007) shows that the observed X-Ray luminosity, L_X, for solar mass stars covers more than two order of magnitudes, once that dependence from the central star luminosity and age are taken into account.[6]. Thus I have simulated such effect computing again the models adopting X-Ray luminosity $L_X(0.1-10 \text{ } keV)$ 10 times fainter and 10 times stronger to ensure that any scatter produced by varying screen thickness at fixed $L_X = 2 \times 10^{30} \text{ erg s}^{-1}$ would also be reproduced for higher or lower X-ray luminosities.

It worth noting that the spectrum is renormalized to the adopted value of L_X(0.1-10 keV) after that the screening effect is taken into account to isolate the effects of the incoming radiation field hardness from the increased amount of incident number photons. This prescription results in the unscreened models to have a total ionising luminosity L_{tot}(13.6 eV-10 keV) of approximately twice the X-ray luminosity and the moderately screened models ($N_H = 10^{18}$ cm^{-2}) to have a total ionising luminosity 1.2 times the base luminosity.

Finally note, the position of the source do not correspond to the center of the grid, but for but at the height of 2 R$_\star$ along the z-axis of the system. In few cases it were already available models with a different source height (10 R$_\star$).

3.2.3   Disk models

To compute the line luminosities it is needed an initial guess of the dust density and temperature structure. I followed the general approach used in lines luminosity studies using a precalculate fixed grid representing the typical disk dust density and temperature structure. Two kind of models were used in this investigation. On first I used d'Alessio disk models available in

---

[6]The X-Rays luminosity, L_X, of the young population in Orion Nebula and Taurus-Aurigae clusters spans, respectively, luminosities from $\log L_X = 27$ to 32 and $\log L_X = 28$ to 31. However, Preibisch et al. (2005) shown that the ratio of X-Ray to stellar luminosity is almost constant, thus, due to the scaling of the stellar luminosity with mass, $L_\star \propto M_\star^2$, two order of magnitude of spread can be advocated to the masses range of young objects. Moreover evolutionary spread in stellar age can explain a further order of magnitude spread in L_X (Feigelson et al., 2005)
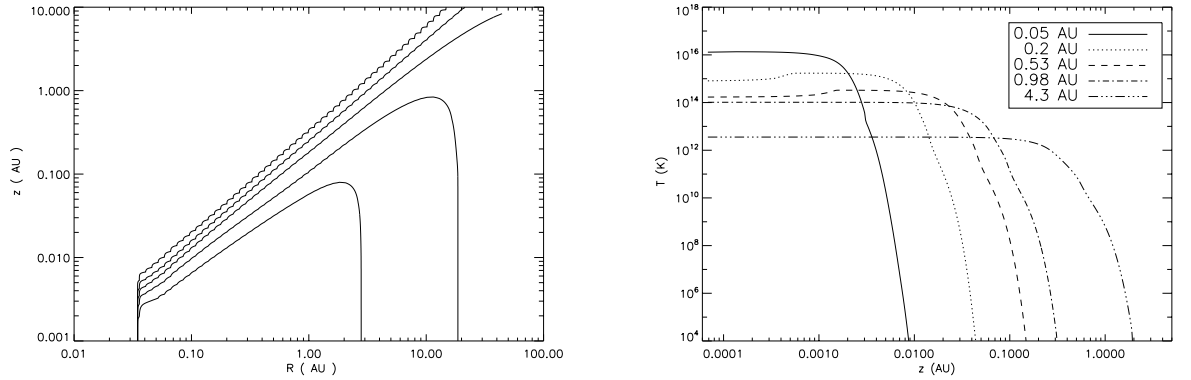
Figure 3.4: Density structure for the d'Alessio disk model used in this work as as initial distribution. The plotted curves are the isodensities relative to 10^5, at higher heights, to 10^{13} particles cm^{-3} deeper into the disk with steps of 10^2 cm^{-3}.

literature (D'Alessio et al., 1998), consisting in a detailed numerical solution of a geometrically thin disk problem under the heating effects of the viscous dissipation and the irradiation from the central star.

Such model were computed assuming the steady state and that the vertical and the radial structure were decoupled problems like in Lynden-Bell and Pringle (1974). The viscous accreting heating is taken into account throught the formulation of Pringle (1981), with a parametric treatment of the viscosity through the α prescription with viscosity parameter setted at $\alpha = 0.01$. Moreover, for the initial density structure, it is assumed that the mixture of dust and gas in the disk are thermally coupled, in other word descrived by a unique temperature. The choise of star + disk parameters was done to best reproduce the typical T Tauri star in matching the median spectral energy distribution in a star formation region. Following D'Alessio (2003), the model is composed by a central star of mass 0.7 M$_\odot$, radius 2.5 R$_\odot$ and temperature 4000 K surrounded by a disk of mass 0.027 M$_\odot$ and estention 100 AU. The corresponding accretion rate is of the order of M$_{accr}$ = 10^{-8} M$_\odot$ yr^{-1}, that best reproduce the spectral energy distribution of Taurus. Figure 3.4 and 3.2.3 represent the density and temperature structure of the descrived model.

D'Alessio models are the solution of a set of differential equations that describe the disk structure, The degree of flaring of the disk surface is com-
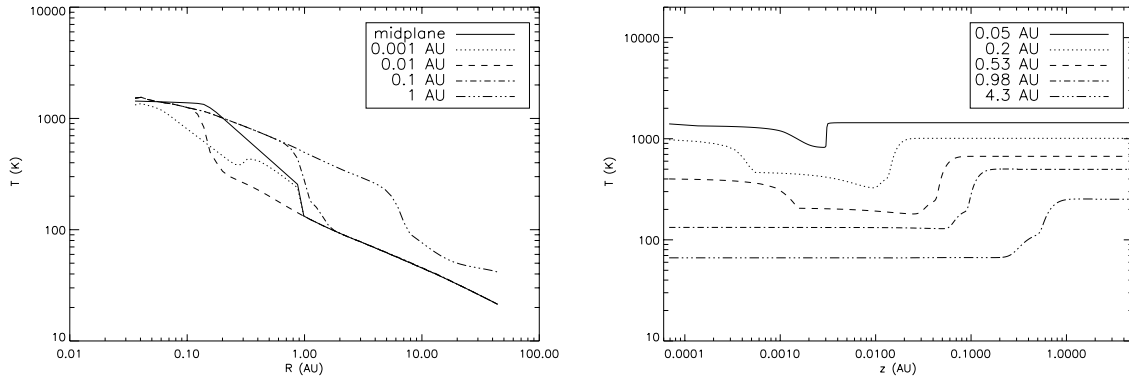
Figure 3.5: Temperature structure for the d'Alessio disk model used in this work. Notice the higher temperature in the midplane respect the slightly higher layers.

puted selfconsistently and has a fixed value once setted the central star and disk parameters. However, the investigation of the slope of the spectral energy distribution shown that stars with the same physical properties can have disks with different flaring. Thus, even if d'Alessio models reproduce the mean shape of the the typical disk population, single objects can have different structures, not descrived by the assumptions of such models. For example, evolutionary effects like the dust sedimentation toward the midplane can produce flatter systems and thus altering the heating efficiencies of the inner regions (Furlan et al., 2005).

The flaring of the disk adds an extra term into the grazing angle at which the radiation strikes the disk (Chiang and Goldreich, 1997). This irradiation angle at a distance R from a star of radius $R_\star$ is given by :

$$\psi \simeq 0.4\frac{R_\star}{R} + R\frac{d}{dR}\left(\frac{H_s(R)}{R}\right) \tag{3.3}$$

where H_s is the height above the midplane where the disk become optically thick to impinguing stellar radiation. Such effect should be taken into account when considering the heating and ionizating of the disk by the X-Rays. To mimic the effect of the flaring keeping costant the other parameters I used the simple analytical prescription of the disk structure adopted by Robitaille et al. (2006) to produce his grid of spectral distributions. The density dis-
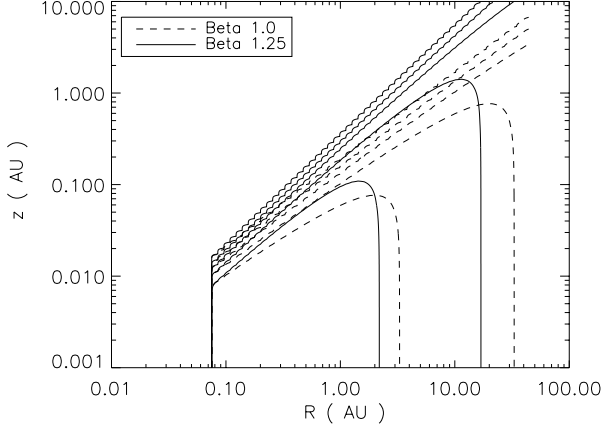
Figure 3.6: Isodensity curves of the two input disk models used in this work to explore the impact that different degree of flaring has on [Ne II] line luminosity. The black solid lines show the flat model ($\beta = 1.0$) and dashed lines show the flared model ($\beta = 1.25$). The plotted contours refer to increasing densities from 10^5, at higher heights, to 10^{13} particles cm^{-3} deeper into the disk with steps of 10^2 cm^{-3}.
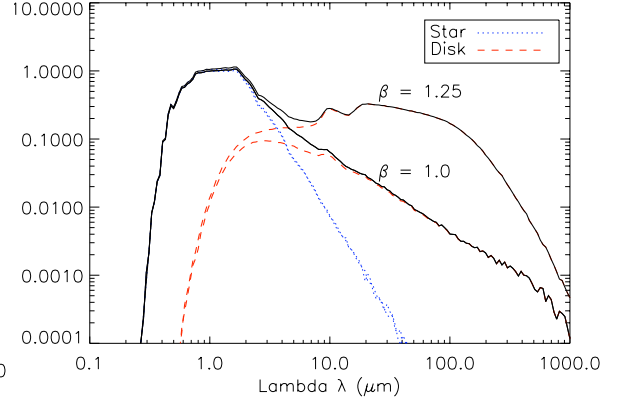
Figure 3.7: Spectral energy distribution relative to the flared and the flat models used in this work.

tribution is given by a power-law decline in radial direction coupled of a formal solution of 1D hydrostatic equilibrium of an isotermal disk along the z-direction (Bjorkman and Wood, 1997; Hartmann et al., 1998):

$$\rho(R,z) = \rho_0 \left(1 - \sqrt{\frac{R_\star}{R}}\right) \left(\frac{R_\star}{R}\right)^\alpha \exp\left(-\frac{z^2}{2H^2(R)}\right) \qquad (3.4)$$

where ρ_0 is a scale factor fixed by the disk total mass and $H(R)$ is the disk pressure scale height. The dust distribution do not continue until the star, but it is truncated at the dust sublimation radius, R_{in}, depending to the temperature, T_{dust} at which the dust evaporate. For a typical dust composition, T_{dust} is ~ 1600 K, but it can vary in the range 1500-1800 K depending of

dust costituents. I have followed Whitney et al. (2004) adopting an empirical relationship between R_{in} and T_{dust}:

$$R_{in} = R_\star (T_{dust}/T_\star)^{-2.1} \tag{3.5}$$

The pressure scale height at distance R from a star of mass $M_\star$ is defined by hydrostatic equilibrium and depends by the midplane disk temperature T_c as

$$H(R) = \sqrt{\left(\frac{k_B T_c}{\mu m_H} \frac{R^3}{G M_\star} \right)} \tag{3.6}$$

where k_B is the Boltzmann constant, G is the gravitational constant, μ is the mean molecular weight and m_H is hydrogen atomic mass. Note that H is different than H_s defined above. The latter is a factor few times H (Dullemond et al., 2001). In general, as it was shown by Chiang et al. (2001), the ratio between H_s and H depends on distance from the star and should be computed by the dust opacty of the disk atmosphere. To overcame such difficulty I have followed Robitaille et al. (2006) assuming that the disk scale height increase with radius as a power-law, $H \propto R^\beta$, where β define the flaring power. In such formulation the scale height is fixed at the dust sublimation radius, $H_{in} = H(R_{in})$ to be that of the hydrostatic equili with $T_c = T_{dust}$ thus:

$$H(R) = z_{factor} * H_{in} \left(\frac{R}{R_{in}} \right)^\beta \tag{3.7}$$

where z_{factor} is introduced as a coefficient to reproduce the effect of eventual gas closer to the star than R_{in} whose opacity would reduce the stellar flux incident the disk inner edge.

Hence, β, defined as a constant through the disk, parametrizes the degree of flaring in the disk. Increasing the β parameter the surface of the model has an higher height respect the midplane at fixed distance from the star. From the integration of the eq. 3.4 along z-direction it is determined the surface density distribution that scales as $\Sigma(R) \propto R^{\beta - \alpha - \frac{1}{2}}$. Assuming precise declines for $\Sigma(R)$, it is possible to couple the radial profile with the vertical one. To fix such coupling and to reduce the number of free parameters, I have chosen to keep the exponents costant over the whole disk and to constraint $\alpha = \beta + 1$, as prescribed by Whitney et al. (2003a) and Whitney et al. (2003b). In such way, all the computed models have asurface density power law scaling as $\Sigma(R) \sim R^{-1.5}$, indipendently from the values of the radial and height exponents, as expected in the "minimum mass solar nebula"

(MMSN) distribution[7] (Hayashi, 1981) and the density profile obtained from some extrasolar systems (Kuchner, 2004). However, observations of young circumstellar disks Kitamura et al. (2002), where planets are not yet formed, with high resolution mm-wave continuum imaging indicate that, at least in T Tauri stars, $\Sigma(R) \sim R^{-p}$, with p ranging from 0 to 1. Such values are in agreement with the simple model of a the steady uniform-α accretion disk model, for which, due to the conservation of angular momentum, $p = 1$ (Shakura and Sunyaev, 1973). This discrepancy is due to the assumptions of the steady state, that is verified only for short periods of the disk lifetime. Even if the "minimum mass solar nebula" does not strictly represent the mass distribution at any istant, it is seems that planetary systems has passes throught it during their lifetime.

To evaluate the effect of flaring of an X-Ray irradiatated disk on the [Ne II] luminosities and line profiles, I built two different models with the same central star and disk parameters of the d'Alessio one, but a different degree of flaring. Adopting a dust sublimation temperature, T_{dust}, of 1600 K, the dust sublimation radius is $R_{in} \sim 0.08$ AU, around twice the one obtained in the case of d'Alessio one, where the inner radius is $R_{in} \sim 0.03$ AU. Extreme values of $\beta = 1.0$ and $\beta = 1.25$ corresponding respectively to a 'flat' and a 'flared' disk case were used to determine the amplitude of the spread in the [Ne II] luminosities and their line profiles. Such values are the limits for the β parameter in the entire set of SEDs of Robitaille et al. (2006), that are typically used in the literature to fit real observations (Alcalá et al., 2008). The density distribution for the flared model have similar slope of the d'Alessio viscous model for distances $R \geq 6$ AU (D'Alessio et al., 1998) and it is really close to the power of 9/7 obtained in the special case of a passive irradiate disk model with fixed ratio between H_s and H (Chiang et al., 2001). Hence, to reduce the differences in the two different disk models, I have detemined the z_{factor} in order toi have the flared model to match the d'Alessio one. The resulting z_{factor} adopted is then 1.

The SEDs relative the two density distribution, computed with the montecarlo radiative code of Whitney et al. (2003a), are shown in Figure 3.7.

Figure 3.6 shows the isodensity curves of the two disk models with different flaring powers. Comparing the flared model to the flat model, the latter

---

[7]The MMSN model is believed to represent the dust distribution of the Sun primordial disk where the solar system formed. The distribution was computed by Hayashi distribuiting continuosly the mass of each planet in its surrounding. Recent observations of extrasolar planets suggest that planets migrate during the early stages of their evolution, going against the MMSN distribution. However, the few studied cases of extrasolar planetary systems indicate profiles that are still compatible with such profiles, hence the MMSN distribution is still used in literature.

has a scaleheight reduced typically by a factor of about 3-4 between cylindrical radii from 1 to 10 AU. In order to isolate the effects of disk flaring only I keep the density structures fixed and do not impose hydrostatic equilibrium on these models.

Finally, for the disk gas I have adopted the solar chemical composition (Asplund et al., 2005) depleted in base to Savage and Sembach (1996) or, in number densities respect to hydrogen, equal to He/H = 0.1, C/H = 1.4^{-4}, N/H 8.32×10^{-5}, O/H = 3.2×10^{-4}, Ne/H = 1.2×10^{-4}, Mg/H = 1.1×10^{-6}, Si/H = 1.7×10^{-6}, S/H = 2.8×10^{-5}.

Table 3.1: Summary of parameters used in the disk models. For detail read the text

Model	d'Alessio	Analytical
$M_{\star}$ ($M_{\odot}$)	0.7	0.7
$T_{\star}$ (K)	4000	4000
$R_{\star}$ ($R_{\odot}$)	2.5	2.5
M_{disk} ($M_{\odot}$)	0.027	0.027
R_{disk} (AU)	100	100
M_{acc} ($M_{\odot}$ yr^{-1})	10^{-8}	-
R_{in} (AU)	0.08	0.03
Flaring	selfcomputed	β-prescription

3.2.4 Model strategy summary

Each model consist in an input initial density and temperature structure. In case of d'Alessio model, such input parameters were already available, instead for the analitical density distribution I have used Whitney et al. (2003b) radiative code to determine the dust temperature. The largest differences were obtained mainly in the midplane due to the viscous heating present in d'Alessio models. Such cells, however, do not contribute to the [Ne II] emission and are barely reached by any energy packet due to the large column densities they have to cross. However, Whitney et al. (2003b) adopt grids in polar coordinates, while MOCASSIN works with cartesian coordinates. To overcome such issue I have interpolated the temperature structure in function of the vertical column density and projected in the adopted density grid. Despite this, sligthly differences in the initial cell temperature can be present, however, they do not influence the result.

The MOCASSIN code requires several days to run a single model even on a cluster, often with limited access. For this reason an accurate modelling strategy is required. In this work, a total of 21 models were computed; of this number, some of the thermo-chemical structures were already available from the work of Ercolano et al. (2009), in which case I have calculated the line emissions, while most of them were full computed. Moreover, most of the models were computed twice adopting or not the hydrostatic equilibrium routine for convergency reasons.The same model were computed more than one time to determine the errors in the results due to the stocastic nature of the code.

To investigate the effect of the flaring of the disk a total of 6 models were computed relative to two density distribution, with $\beta = 1.0$ and 1.25, each one with three different total luminosity for the irradiating, $L_X = 2\times10^{29}$, 2×10^{30}, 2×10^{31} erg s^{-1}. For the shape of the irradiating spectrum, 6 models were computed adopting the 6 high-energy spectrum of Figure 3.3 with a different amount of column extinction between the source and the disk (N_H = 0, 10^{18},10^{19},10^{20},10^{21},10^{22} cm^{-2}) for one at fixed irradiating luminosity L_X = 2×10^{39} erg s^{-1}. Four (4) additional models were calculated for the two spectra N_H = 0 and 10^{21} cm^{-2} with the total luminosity , L_X, scaled by a factor 10 times higher and lower. Finally, I computed the line luminosities for 5 more available models, 4 of which had the as irradiating source the X-Ray spectrum at single temperature, 3.2. Of those three differs for the value of total luminosity L_X and the last one has the source shifted at 10 $R_\star$ and L_X = 2×10^{30} erg s^{-1}. The last one has the source placed at 10 $R_\star$ and irradiate the full high-energy spectrum, including the EUV component. A complete summary of all the models is reported in table 3.2.

3.2.5 The line profiles

Since MOCASSIN code solves the problem of radiation transfer locally in the grid, it is possible to obtain the total power emitted in a particulary atomic transition from each cell and not only from the overall grid. Thus, adopting a velocity field in the grid, line profiles can be computed for all the models.

In this work I have considered the [Ne II] emission produced in the disk atmosphere and then I have assumed, for simplicity, a disk in keplerian rotation. Other components to the local velocity field, like turbolence or photoevaporative flow, present in the real disks are ignored in the following. A treatment of such components needs a complete numerical solution of the magneto-hydrodinamic equations coupled radiative transfer, solved so far only in limited number of cases, and will be considered in future works.

Table 3.2: Summary of the models used in this work

Disk Model	Height Source $(R_\star)$	Type Source	Attenuation N_H (cm^{-2})	L_X $(10^{30}$ erg s$^{-1})$
D'Alessio	2	X-Ray Single T	0.	2
D'Alessio	2	X-Ray Single	0	0.2
D'Alessio	2	X-Ray Single	0	20
D'Alessio	10	X-Ray Single	0	2
D'Alessio	10	Full Spectrum	0	2
D'Alessio	2	Full Spectrum	0	2
D'Alessio	2	Full Spectrum	10^{18}	2
D'Alessio	2	Full Spectrum	10^{19}	2
D'Alessio	2	Full Spectrum	10^{20}	2
D'Alessio	2	Full Spectrum	10^{21}	2
D'Alessio	2	Full Spectrum	10^{22}	2
D'Alessio	2	Full Spectrum	0	0.2
D'Alessio	2	Full Spectrum	0	20
D'Alessio	2	Full Spectrum	10^{21}	0.2
D'Alessio	2	Full Spectrum	10^{21}	20
Analitical $\beta = 1.0$	2	Full Spectrum	0	2
Analitical $\beta = 1.0$	2	Full Spectrum	0	0.2
Analitical $\beta = 1.0$	2	Full Spectrum	0	20
Analitical $\beta = 1.25$	2	Full Spectrum	0	2
Analitical $\beta = 1.25$	2	Full Spectrum	0	0.2
Analitical $\beta = 1.25$	2	Full Spectrum	0	20

The disk is assumed to be axis-symmetric, so i have 3D grids ($N_r \times N_z \times N_\theta$) from the simulated 2D output of the code($N_r \times N_z$), sampling the polar θ coordinate at steps of 1 degree. The overall grid is the composed of 89 $\times$ 1779 $\times$ 360 cells each one with emission $I(\lambda, R, z)$. For each cell, moreover, the local contribution to the line profile is assumed to be Doppler broadened by the local thermal velocity, v_{th} of the Ne$^+$ ions equal to

$$v_{th}(R, z) = \sqrt{\frac{3k_B T(R, z)}{m_{\text{Ne}} m_{\text{H}}}} \tag{3.8}$$

where $T(R, z)$ is the temperature of the cell. In the computed models the temperature structure of the disk produces thermal broadening width $\leq$6 km s^{-1}. Cells at fixed R and different height z move at the same velocity $v_{kepl} = \sqrt{\frac{GM_\star}{R^3}}$, due to the hydrostatic balance among the z-direction. Thus, the single cell contribution located at (R_i, θ_j, z_k), has the form

$$\phi(R_i, \theta_j, z_k, v) = \frac{I(R_i, z_k)}{\sqrt{2\pi} v_{th}(R_i, z_k)} \exp\left(-\frac{(v - v_{los}(R_i, \theta_j))^2}{2v_{th}(R_i, z_k)^2}\right) \tag{3.9}$$

where $v_{los}(R_i, \theta_j)$ is the cell velocity projected along the line of sight. The projection of the keplerian rotation $v_{kepl}(R)$ on the generic line of sight forming an angle i with the perpendicular of disk surface is given by

$$v_{los}(R_i, \theta_j) = v_{kepl}(R) \cos\theta \sin i \tag{3.10}$$

The emission profiles of each cell is sampled at step of 0.5 km s^{-1} in the velocity range of [-50,50] km s^{-1}. The overall line profile, $\Phi(v)$ is computed by summing all together up the contributions from each cell of the grid

$$\Phi(v) = \sum_{i,j,k} \phi(v) \tag{3.11}$$

Group of cells with the same projected velocity contribuite to the profile at the same λ, see figure 3.8.

In the sum I have assumed that the midplane is optically opaque to the [Ne II] line radiation so only contributions from one side of the disk are taken into account when computing the profile. Indeed, adopting the dust cross section $\sigma_{12.81\mu m} = 1.6 \times 10^{-23}$ cm^2 / H and $\sigma_{15.5\mu m} = 1.4 \times 10^{-23}$ cm^2 / H from Weingartner and Draine (2001) extinction law with $R_V = 5.5$, reproducing the typical dust absorption in molecular clouds, I found that optical depths of the order of $\sim$1 are reached for hydrogen column density of about 6-7 x 10^{22} cm^{-2}. Such column density are reached, for all inclination $\leq$ 60, at heights
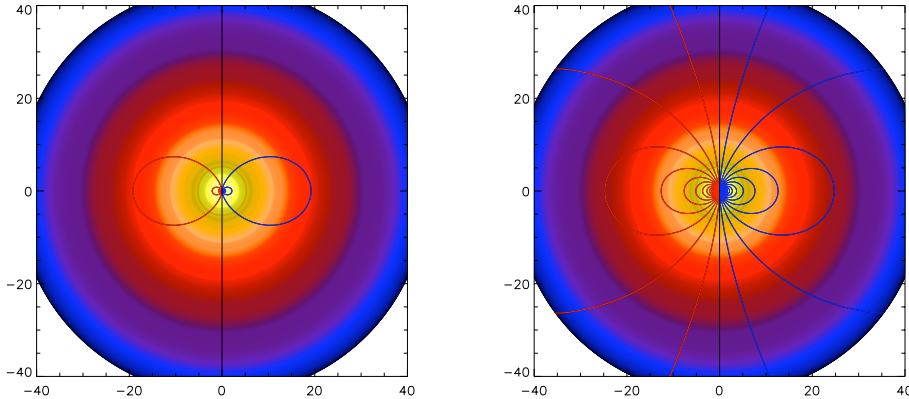
Figure 3.8: Computing the line profile. Contour levels, sampled at $1\,\mathrm{km\,s^{-1}}$, split the disk in regions with the same projected rotational velocity, contributing to the overall profile at the same λ. The two extreme cases of line of sight inclinated to 10º (left panel) and 80º (right panel) and are displayed.

of ≤ 0.1 AU to radial distance of 1 AU and $\sim$1 AU to distance $\sim$10 AU, deeper in the disk than the Ne^{+} emitting region shown for example in Figure 3.9. Still, in the case of almost edge-on systems the column density along the line of sight[8] could be large enough to attenuate the observed line intensities, this is not taken into account in this work, even if it should be considered in future comparisons with real observations. For higher inclination the disk inner regions are obscured, changin the shape of the resulting overall line profile expecially in the wings.

Scattered light contribution to the profile is ignored due to the low albedo at 12.81 μm of the adopted Weingartner and Draine (2001) dust model ($\leq$ 0.01) . However, it worth nothing that the albedo could be significant for different dust models, up to value of 0.3 in cases of high abundances of icy grains. Such grains could not exist at the high temperature presents in the emitting region, but they can reflect toward observers the radiation propagating toward the midplane. Such second

---

[8]Mostly produced by the outer disk and not covered by the model grid here.

level radiation is not taken into account in the actual version of MOCASSIN.

The computed line profiles are smoothed to lower resolution than the virtual one by convolution with a gaussian function to simulate the instrumental effect. The results presented in the next section are relative to $\lambda/\Delta\lambda \sim 30000$ and 150000, obtained respectively with gaussian function with FWHM of 10 km s^{-1} and of 2 km s^{-1}, comparable with the available high-resolution spectroscopic observations.

3.3   Results

In this section I present the results relative the Ne emission line simulated by the code MOCASSIN. I report the integrated line luminosities, spatial distribution and theorical line profiles relative the disk and/or the irradiating source spectrum models described above. Due to the stocastic nature of the code using a Monte Carlo method in the following errors on the given line luminosities were obtained by comparing multiple runs of the same model and results to be of about 5% for the lines in question. However, in highly extincted models errors are usually higher, $\sim$10% or more, since less packets reach the deeper cells. Higher precision can be obtained adopting an higher number of energy packets emitted by the irradiating source, however due to really high computational times needed it is left for future works.
Despite the uncertains it is still possbile to draw relevants results regard the [Ne II] line luminosity response to (i) changes in the shape of the irradiating spectrum and (ii) changes in the disk density distribution (flaring) are shown below. For sake of completeness, I report also the computed line fluxes for the [Ne III], however they are not deeply discussed in the following, because there are still unresolved discrepancies with the lack of detection. In fact, I find that [Ne III] line luminosity is from 5 to 10 times fainter than the [Ne II], compatible with other works (Ercolano et al., 2008b; Gorti and Hollenbach, 2008). If that is the case the 15.5 μm line should have been observed in several objects, while the only detection so far indicate a line $\sim$ 20 times fainter (L([Ne II])/ L([Ne III]) $\sim$0.06, Lahuis et al. (2007).

3.3.1   Effect of the shape of the spectrum

Table 3.3 shows the values of [Ne II] 12.81 μm and [Ne III] 15.5 μm line luminosities for models irradiated by the X-Ray multi-temperature thermal spectrum descrived in section 3.2.2 screened by circumstellar material of increasing column densities 0., 10^{18}, 10^{19}, 10^{20}, 10^{21}, 10^{22}cm^{-2}, see Figure 3.3.
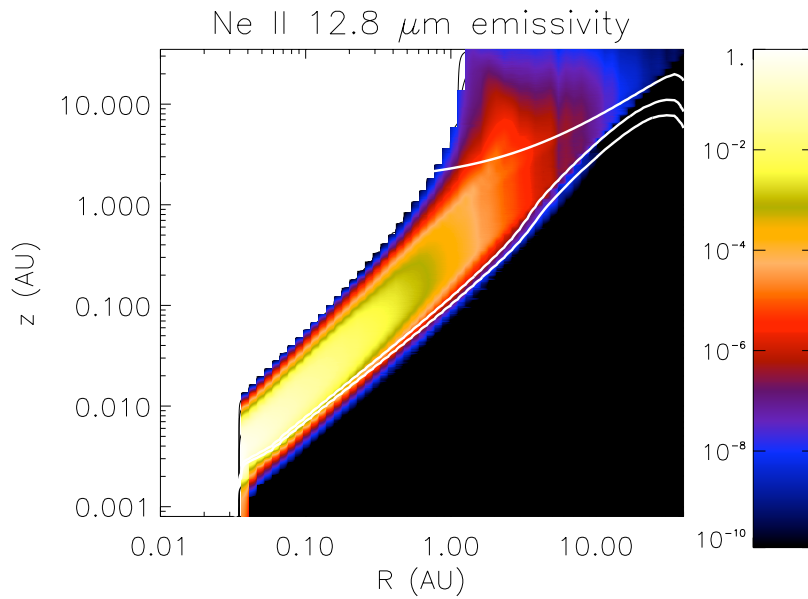
Figure 3.9: Section of the disk showing the region contributing to the [Ne II] emission. The simulated model refer to the d'Alessio disk model irradiated by the full high-energy spectrum of figure 3.3 The white lines, from the the deeper one to the higher layers, defines the regions where, respectively, column densities of 10^{22}, 5×10^{22} and 10^{23} cm^{-2} along the line of sight are reached. The case of 60º of inclination is shown here. For smaller angles all the emitting regions are observable, but at higher inclination the inner regions of the disk are obscured, resulting in different overall line profiles.

Table 3.3: [Ne II] and [Ne III] luminosities of disk irradiated by different high-energetic shaped spectrum with $L_X(0.1-10\text{keV}) = 2\times10^{30}$ erg s^{-1}. The disk model adopted is a d'Alessio disk model.

MODEL	L_{tot}(13.6 eV-10 keV) 10^{30} erg s^{-1}	[Ne II]	[Ne III]
		$(10^{28}$ erg s$^{-1})$	
Unscreened	4.0	2.3	4.9×10^{-1}
Log N$_h$ = 18	2.3	1.9	4.3×10^{-1}
Log N$_h$ = 19	2.04	1.7	3.2×10^{-1}
Log N$_h$ = 20	2.0	1.5	2.2×10^{-1}
Log N$_h$ = 21	2.0	9.1×10^{-1}	1.5×10^{-1}
Log N$_h$ = 22	2.0	1.4×10^{-1}	2.5×10^{-2}

Table 3.4: [Ne II] luminosities computed for a range of L_X. The corresponding value of L_{tot} are also reported.

MODEL	[Ne II] $(10^{28}$ erg s$^{-1})$		
L_X [2 10^{30} erg s^{-1}]	0.1	1.0	10.0
Unscreened ($L_{tot} = 2\,L_X$)	2.9×10^{-1}	2.3	22.0
Log(N$_H$) = 21 ($L_{tot} = L_X$)	3.0×10^{-2}	9.1×10^{-1}	5.8
Flared ($L_{tot} = 2\,L_X$)	1.0×10^{-1}	1.6	17.3
Flat ($L_{tot} = 2\,L_X$)	1.7×10^{-2}	1.3×10^{-1}	7.0×10^{-1}
-	[Ne III] $(10^{28}$ erg s$^{-1})$		
Unscreened ($L_{tot} = 2\,L_X$)	4.6×10^{-2}	5×10^{-1}	4.2
Log(N$_H$) = 21 ($L_{tot} = L_X$)	0.7×10^{-2}	1.8×10^{-1}	1.4
Flared ($L_{tot} = 2\,L_X$)	1.9×10^{-2}	1.8×10^{-1}	3.2
Flat ($L_{tot} = 2\,L_X$)	3.1×10^{-3}	3.2×10^{-2}	1.3×10^{-1}

Keep in mind that, to match the observed X-Rays luminosities, the spectra are normalized to have an integrate luminosity in the energy range 0.1-10 keV, so it is more useful to plot the neon luminosity to the total luminosity ratio as a function of the absorbing screen column as shown in Figure 3.10. Here the dashed line indicates the value predicted in the case of unabsorbed source.

As reported Table 3.3, EUV radiation (> 21.6eV and < 100eV) is less efficient at producing [Ne II] than the (soft) X-rays ($\gtrsim 100$ eV). In fact, even if the unscreened models have a total ionising luminosity (X-Rays+EUV) which is double than the X-ray only luminosity, they only produce a moderate increase in L([Ne II]). Such result strongly depends on the place where [Ne II] is most efficiently produced. Figure 3.15 shows an example of the density and temperature structure resulting after the irradiation and figure 3.16 shows the Ne^+ and Ne^{++} ion fractions and the [Ne II] 12.81 μm and [Ne III] 15.5 μm emissions as function of the height respect the midplane at different distances from the star. The dotted vertical line represents the height were the electron number matches the particle number densities. Such limit roughly define the region where the full ionized region starts[9]. [Ne II] is emission is mostly located in the deeper low ionization layer (electron fraction $x_e \lesssim 10^{-3}$), see also Glassgold et al. (2007); Güdel et al. (2010), irradiated by the EUV radiation less efficently than the more penetrative X-Rays[10]. Those results are computed directly by the code solving the radiative trasfer problem, indicating that any earlier statements based on order magnitude extinction estimates (D.Hollenbach and Gorti, 2009; Gorti and Hollenbach, 2008) suggesting that the EUV would be the main ionizing source were probaly inexact. Double ionized Ne is, however, less abundant in such layer due to the high efficiency of the charge exchange with the neutral H atoms, quickly recombining Ne^{++} into Ne^+. Contrarywise the process of charge exchange from singly ionised to neutral Ne is instead extremely slow, conspiring to produce high abundance of Ne^+ in this warm layer (few thousands of K). The net result is an [Ne III] emission is an order of magnitude weaker than the [Ne II]. However, higher in height in the lower density region of the disk atmosphere, standard photoionisation of neutral Ne by the EUV photon becomes the dominant source of ionization. The lower neutral H fractions in this region not allow an efficiente

---

[9]Based on the thermochemical structures here computed, it would be possible to investigate the efficiency of the MRI as possible viscosity process. However, to achieve such aim are necessary better disk models taking into account viscous dissipation in the upper layer. The simple models here studied are not sufficient to derive any robust conclusion.

[10]Column densities of neutral hydrogen of $\sim 10^{17} - 10^{18}$ cm^{-2} produce a unity EUV optical depth, instead to achieve the same results in the X-Ray cases are needed column densities of $\sim 10^{22} - 10^{23}$ cm^{-2}.
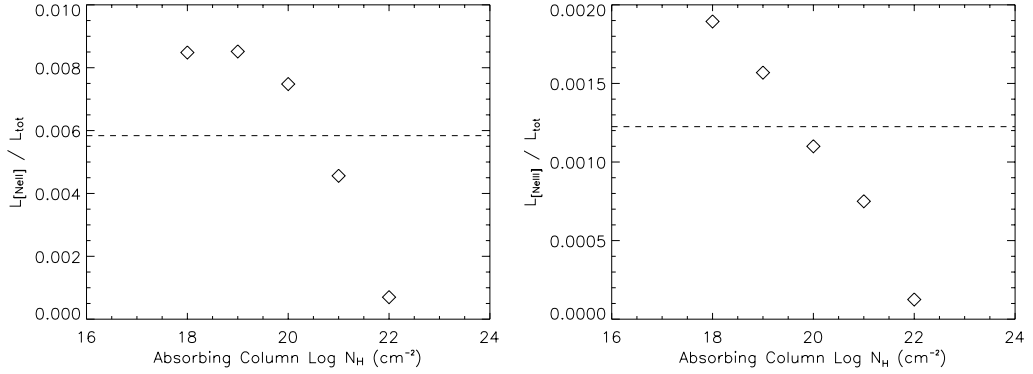
Figure 3.10: L([Ne II])/L$_{\text{tot}}$ as a function of the screening column of the irradiating spectrum. The dashed line indicates the value for the unscreened spectrum.

exchange process and most of the Ne^{++} produced remain in double ionized state, leaving higher [Ne III] emission in this H II-like photoioned layer.

The [Ne II] emission spatial map for the unscreened model is shown in Figure 3.9.

Furthermore, the models shown in Table 3.3 also suggest that the hard X-ray region is inefficient at the production of [Ne II] compared with the soft X-ray region. Indeed models irradiated by hard spectra with N$_H \geq 10^{21}$ cm^2 show a steep decline in the [Ne II] luminosity, even after forcing the X-ray luminosity (0.1-10 keV) to stay constant. Models illuminated by a harder X-ray spectrum result to be colder, the hard X-ray penetrate deeper in the disk reaching denser and colder regions. Such regions contribute marginally to the [Ne II] emission as seen by the spatial distribution. Moreover, in such models the lower temperature of the gas results in a smaller expansion. In such way the disk surface absorbs less efficiently the incoming radiation due to the smaller impact solid angle.

The hardness of the spectrum has a noticeable effect on the [Ne III] 15.5 μm/[Ne II] 12.81 μm ratio. This ratio is higher for softer spectra because doubly ionised Ne in these models can be produced in the upper layers of the disk where the neutral hydrogen fraction is lower and therefore charge exchange less efficient.

Those results show that changes in the irradiating spectrum can give an order of magnitude scatter (an extra factor of $\sim$2 can be introduced, because the L([Ne II]) vs L$_X$ relation do not take into account the effect EUV emission, contributing for a comparable ionising luminosity in the case of unscreened source).
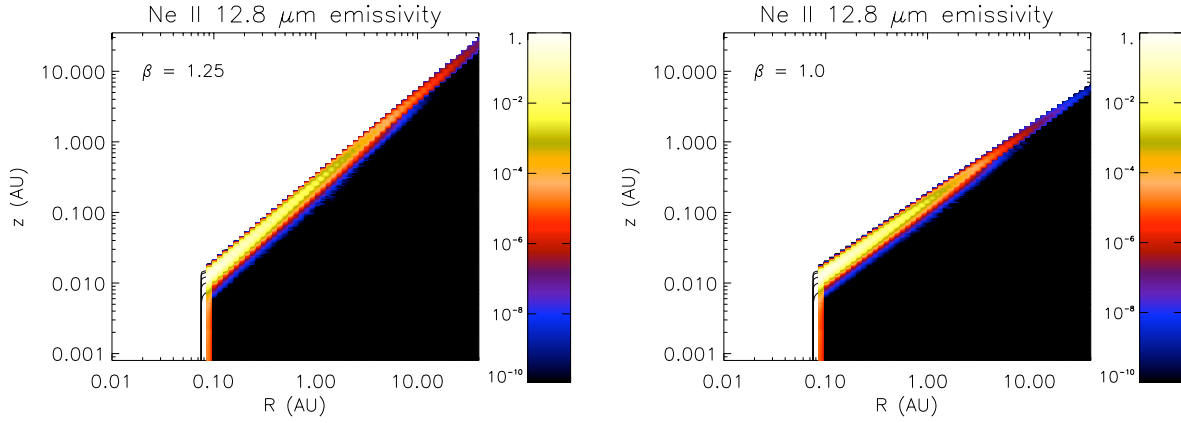
Figure 3.11: Two-dimensional distribution of the [Ne II] emissivity in arbitrary units. The *left* panel refers to the disk model with $\beta = 1.25$ (flared disk), instead the *right* panel show the disk model with $\beta = 1.0$ (flat disk).
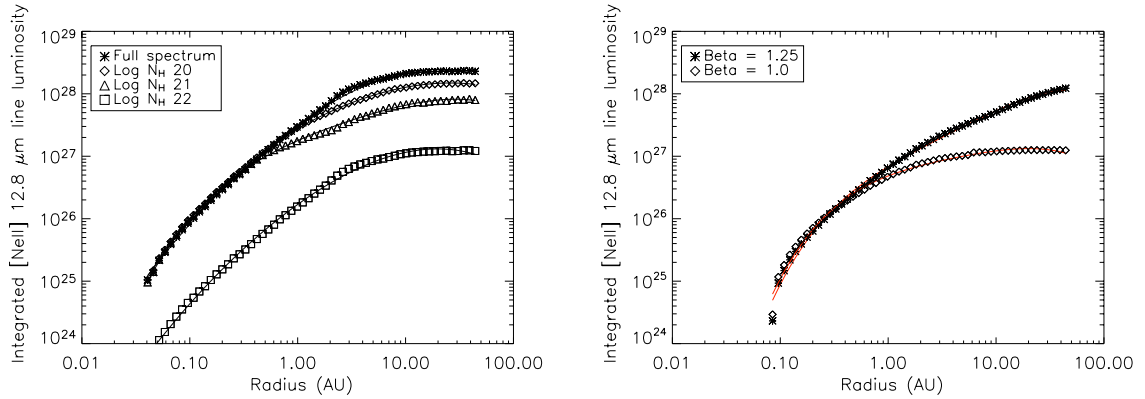
Figure 3.12: [Ne II] cumulative surface emission in erg s^{-1} (see text for details). *Left:* Hydrostatic equilibrium models irradiated by spectra screened by various neutral hydrogen columns. *Right:* Flat and flared disk models computed assuming Robitaille et al. (2006) density distribution.
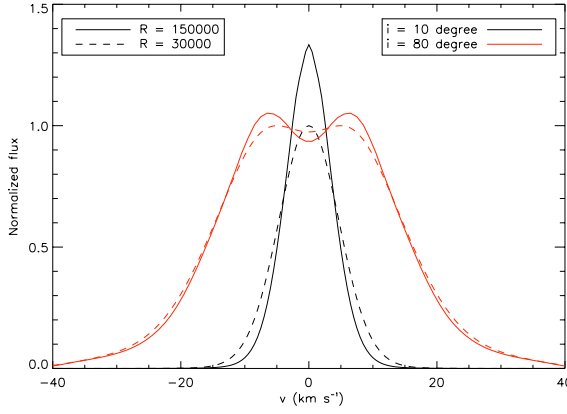
Figure 3.13: [Ne II] line profiles of a Keplerian disk in hydrostatic equilibrium irradiated by an unscreened EUV+X-ray source. The black lines are for low inclination (i = 10º) and the red lines for high inclination (i = 80º) disks. The solid lines have a resolution of R = 150000 and the dashed are the profiles degraded to a resolution of 30000. For clarity the lines are normalized to the peak value of the degraded case.
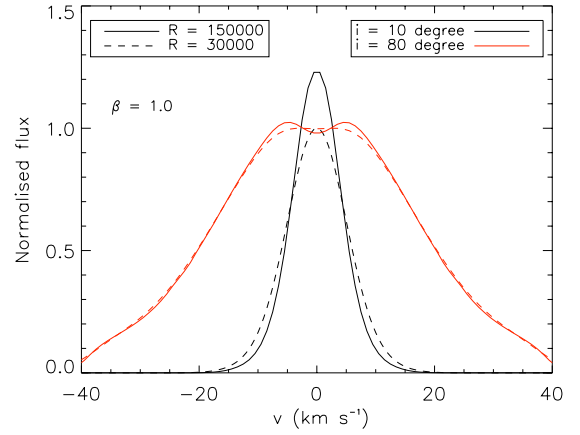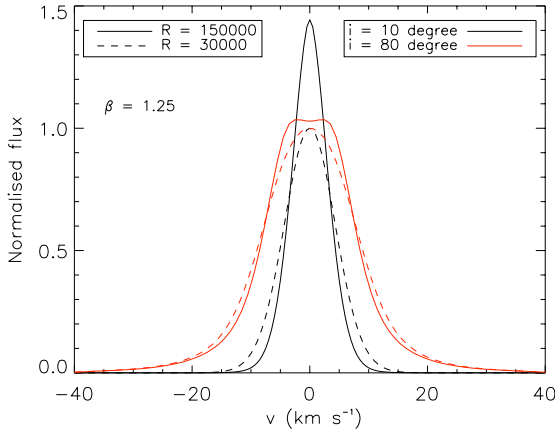
Figure 3.14: As in Figure 3.13, but for the flared disk model ($\beta = 1.25$) (*left*) and flat disk model ($\beta = 1.00$) (*right*) irradiated by an unscreened EUV+X-ray spectrum.

Figure 3.12 (left panel) shows the surface-integrated emission for some of the models discussed in this Section. We find that in all cases half of the total [Ne II] emission comes from the inner regions of the disk, $\lesssim$ 3-4 AU, so that the different spectra do not significantly affect the emission region for this line. Table 3.6 lists the half-luminosity and 90% luminosity radii for models of various screens. As the extent of the emission region does not significantly vary with spectral hardness, the line profiles obtained are also roughly invariant. As an example, Figure 3.13 show the [Ne II] profile for the unscreened model seen almost face on (10º inclination) and almost edge on (80º inclination), with respectly Full Width Half Maximum (FWHM) of $\sim$6-8 and $\sim$25-31 km s^{-1}..
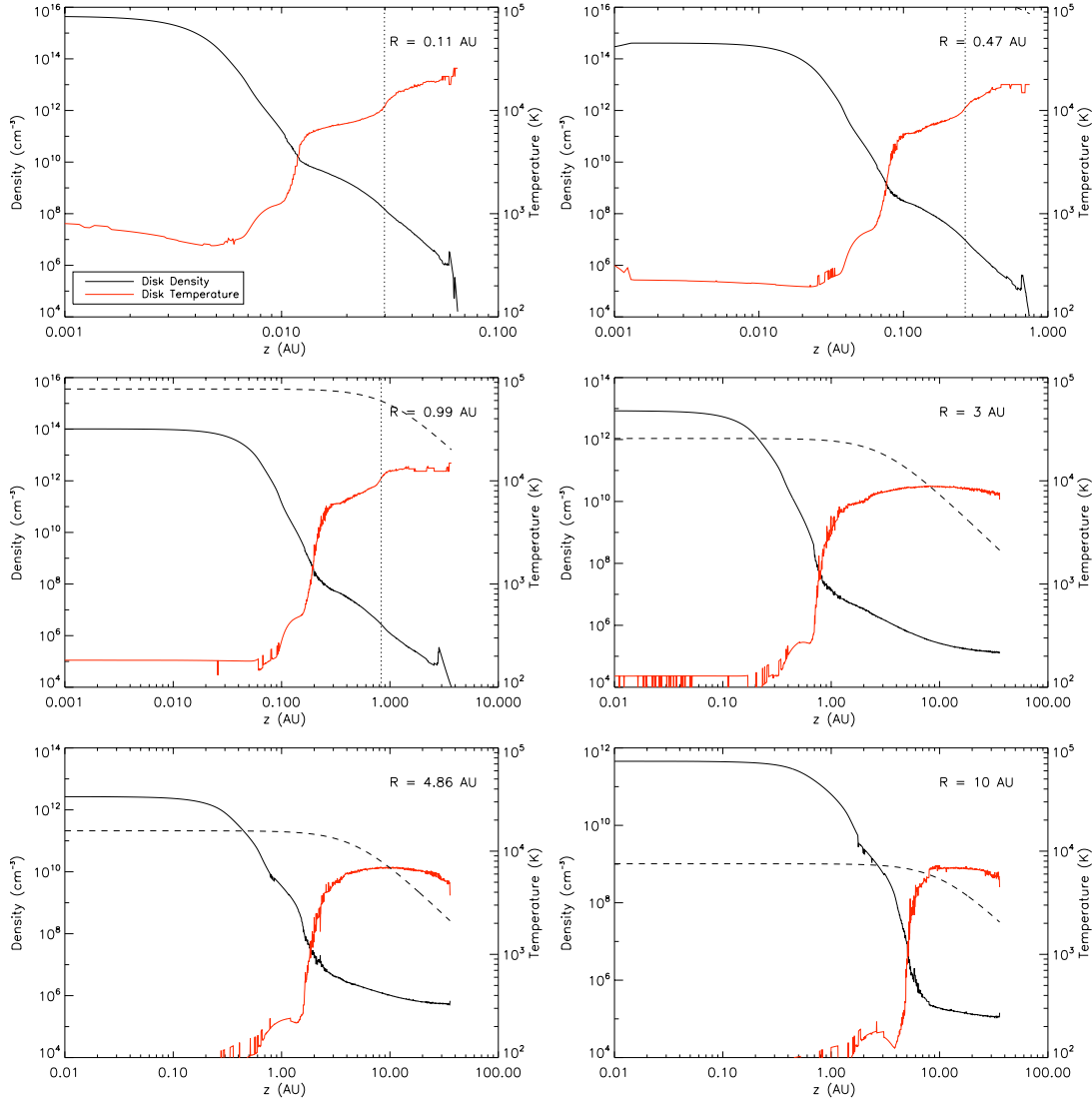
Figure 3.15: Computed density (black solid line) and temperature (red solid line) structure at different disk radii in the case of full high-energy (EUV+X-rays) irradiating spectrum and d'Alessio disk model. The vertical solid line roughly define the boundary of the ionized region. The dashed lines is defined to track the temperature above which the material is not gravitational bound to the disk anymore. Regions whose temperature is higher than this limit are involved in a photoevaporative flow.
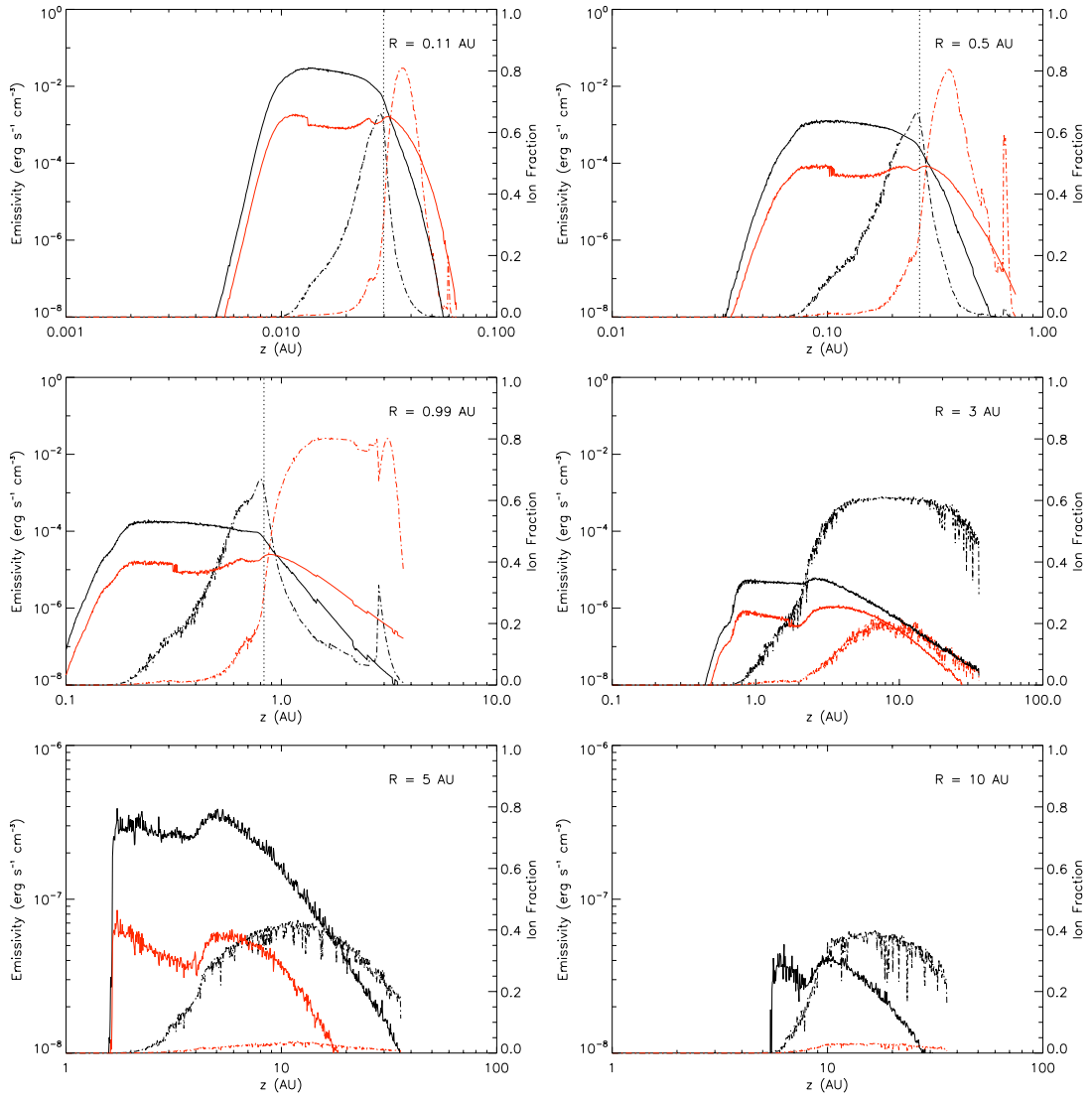
Figure 3.16: Emission of [Ne II] (black dotted line) and of [Ne II] corresponding to the solutions of figure 3.15. The solid lines plot the relative ion fraction for the two species Ne$^+$ (black) and Ne^{++} (red).

Table 3.5: Emissivity distribution statistics. See text for details.

Model	Half-L radius (AU)	90% L radius (AU)
Unscreened	2.9	10.1
Log N_h= 20	3.3	13.0
Log N_h= 21	3.5	12.8
Log N_h= 22	2.9	10.1
Flared $\beta = 1.25$	12.9	34.3
Flat $\beta = 1.0$	1.5	6.1

3.3.2 Effect of the flaring

Table 3.4 also shows the results for the L([Ne II]) for models with flared ($\beta = 1.25$) and flat ($\beta = 1.0$) disks. A casual inspection of this table reveals roughly an order of magnitude increase in the relative luminosity of the [Ne II] line when the flaring is changed from $\beta = 1.0$ to $\beta = 1.25$. This is easily understood when considering that a more flared disk would subtend a larger solid angle to the irradiation source.

Disk flaring has also a dramatic effect on the size of the [Ne II] emitting region. Figure 3.11 shows two-dimensional plots of the [Ne II] emissivity for the flared and flat disk models, while the right panel of Figure 3.12 shows the surface-integrated emission for the line for the two disk models. As summarised in Table 3.6, the emission region in the flared disk model extends out to a radius of $\sim$30 AU, within which 90% of the total [Ne II] luminosity is emitted. This radius is reduced to $\sim$6 AU for the flat disk model. Naturally, this has consequences on the line profiles for these two cases, which are shown in Figure 3.14 for two disk inclinations. The FWHM for the [Ne II] line produced by a flat disk seen almost edge on (inclination 80º) is roughly 40 km s^{-1}, while it is only 17 km s^{-1} for a flared disk where the emission region extends to larger cylindrical radii. The difference is of course smaller if the disks are seen almost face on (inclination 10º), thus dominated by the contribution of the thermal broadening, where a FWHM of $\sim$10 km s^{-1} is expected for a flat disk compared to a FWHM of $\sim$7 km s^{-1} for a flared disk. These statistics are summarised in Table 3.6.

3.3.3 Effect of the source height

Table 3.7 show that the [Ne II] line luminosites, once taken into account the hydrostatic routine, do not change with the position of the source. Result

Table 3.6: FWHM of the line profiles simulated for disks in Keplerian rotation viewed almost face on (10º inclination) and almost edge on (80º inclination) at two different spectral resolutions.

	Inclination 10 degree FWHM ($km\,s^{-1}$)		Inclination 80 degree FWHM ($km\,s^{-1}$)	
R =	150000	30000	150000	30000
Unscreened	8.2	11.1	31.3	32.6
Log N_H = 21	6.2	10.0	25.8	28.1
Flared $\beta = 1.25$	6.9	10.2	16.8	17.6
Flat $\beta = 1.0$	9.5	12.1	40.1	40.8

Table 3.7:

MODEL	[Ne II] (10^{28} erg s^{-1})	
	2 $R_\star$	10 $R_\star$
X-Ray	0.70	0.63
Full spectrum	2.34	2.27

luminosities overlap within the predicted errors by montecarlo testing. This is not true if hydrostatic routine is not included, in fact, without it, the different angle formed by the source rays and the normal to disk surface changes the efficiency heating of the more distant regions of disk. Such effect is not releavant, instead, when the hydrostatic equilibrium is forced on the hot disk. In such case the puffing of the inner disk ($\lesssim$ 10 AU) shadows the external regions most affected by such angle.

3.4   Discussion

As the sample of observed L([Ne II]) luminosities from protoplanetary disks continues to grow, together with the sample of pre-main sequence stars with measured X-ray luminosities, a trend between the two quantities becomes more and more evident (Güdel et al. 2009, Güdel et al. 2010). While this lends evidence to the [Ne II] line being a product of X-ray irradiation of disks as predicted by Glassgold et al. (2007), the large scatter associated with this relation makes the situation less clear-cut. For a handful of objects with known powerful outflows it is clear that this line cannot be used as a
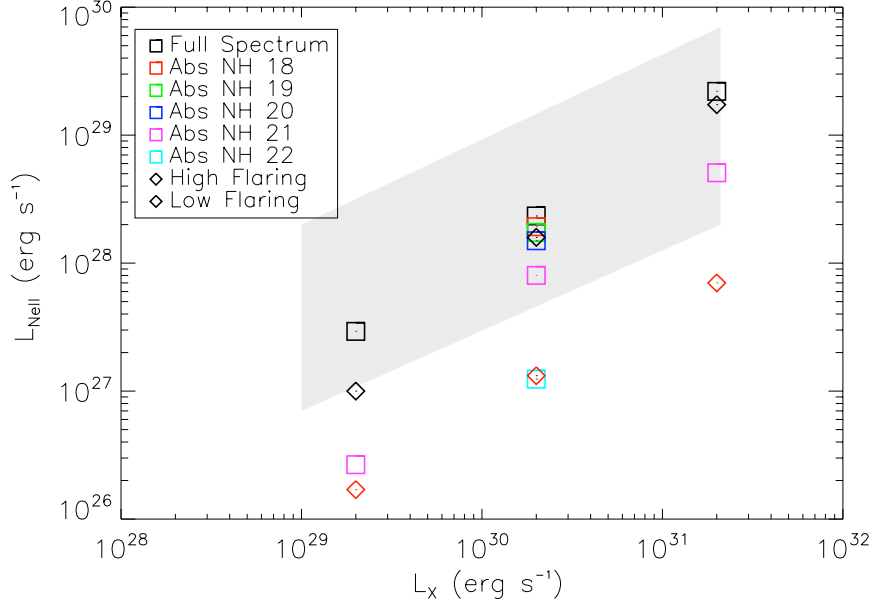
Figure 3.17: Comparison between the prevision of the models, where a relationship between the L([Ne II) and L$_X$ is expected and the observation. The shaded region covers the portion of the L([Ne II)-L$_X$ plane where the systems withundetected outfows falls.

diagnostics of the gaseous *disk* phase, as the emissivities may be dominated by gas in the outflows. However, even after removing objects with known outflows from the sample, there is still approximately *one order of magnitude variations in L([Ne II]) at any given L$_X$*. In this work I have investigated the origin of the large scatter observed in the [Ne II] – L$_X$ relation. We find that variations in the irradiating spectral shape and disk structure (flaring) are sufficient to explain the typically observed scatter of approximately one order of magnitude. Figure 3.17 shows the results from the computed models (coloured symbols) overplotted on a shaded region representing roughly the observations presented by Güdel et al. (2009), excluding the strong outflow objects (blue points in their plot). The definition of such region is affected

by the limited sample statistic that does not allow a sharper outline, but it shows where the bulk of data falls. Moreover, it should be noted here that I use luminosities *after* the screen while Güdel et al. use intrinsic luminosities derived from the observations. We have performed absorption calculations for a subset of the observations from which I found the following: absorbing the intrinsic X-ray spectral models by $N_{\mathrm{H}} = 3 \times 10^{20}$ cm$^{-2} - 4.6 \times 10^{22}$ cm^{-2} (a range occupied by the observations) reduces the 0.1-10 keV luminosity by factors of approximately 1.4–5.5 (also depending on the intrinsic thermal model from the individual fits). On average, thus, the *unabsorbed* L_{X} from the observations should be shifted by a factor of 3 (0.5 dex) to the left to obtain average absorbed values, with individual shifts ranging from 0.15 dex to 0.75 dex. These corrections do not change the plot qualitatively. We, however, refrain from using the individual *absorbed* (post-screen) luminosities derived from the observations here because it is not clear a priori that the absorbed luminosity seen from Earth is close to the absorbed luminosity seen by the disk. The latter luminosity is principally unknown. We also mention that Güdel et al. use the 0.3-10 keV range for their luminosities, while I use 0.1-10 keV. For the post-screen luminosities for stars with $N_{\mathrm{H}} > 10^{20}$ cm^{-2}, however, the difference is minor.

Our model predictions seem to agree well with the observations in terms of reproducing the scatter, and at intermediate and high X-ray luminosities the absolute values of L([Ne II]) also roughly agree with the observations. Models with low X-ray luminosities, however, fall short of the observed values, and while detection limits can partially affect the observations, the failure of the models to produce L([Ne II]) $> 10^{28} erg/sec$ for X-ray luminosities of $2 \times 10^{29} erg\, s^{-1}$ must have another origin. Nevertheless there is an overlap between those prediction for the unabsorbed source and/or the flared disk and the shaded region. Keep in mind, however, that the correction for absorption mentioned above aggravates the discrepancy between the model predictions and the observations (the latter being moved somewhat to the left in Fig. 8), but do not have effects on the conclusions on the scatter of [Ne II] luminosities.

It would be of little use here to speculate what other observational effects may be coming into play, however one thing that is worth noticing is that the measurements plotted in the Figure all come from the *Spitzer* Space Telescope, while recent observations from the ground at higher resolution suggest often lower luminosities than the *Spitzer* data (Herczeg et al., 2007; Najita et al., 2009). This has been interpreted as possible pollution from molecular emission in the *Spitzer* band, while more recent works (Najita et al., 2009) seem to lean toward extended emission, from undetected outflows, which would contribute to the flux in the *Spitzer* aperture, but would be excluded by the narrow slits used for measurements from the ground.

Our results thus support a disk origin of the observed [Ne II] emission as a consequence of X-ray irradiation, at least for systems with moderate [Ne II] luminosities and absence of jets. On the other hand, the additional parameters (X-ray spectral hardness, disk flaring) now found to influence the [Ne II] luminosity add complexity to the interpretation, and the usefulness of the [Ne II] line as a disk diagnostic depends on the ability to confine these other parameters as well. Clearly, [Ne II] *disk* diagnostics needs to avoid stars with known jets and outflows. Under the assumption of full dust and gas mixing, some information about disk flaring can be obtained by modeling the infrared spectral energy distribution (Chiang et al., 2001; Pascucci et al., 2003), providing some important constraints on the range of modeled [Ne II] luminosities. Constraining the shape of the ionizing spectrum is perhaps the most difficult task. The intrinsic spectrum can usually be modeled sufficiently well based on intermediate- or high-resolution X-ray spectroscopy, but the absorbing gas column density toward the disk may be different from that toward the observer. However, gas absorption matters the least in systems with weak or absent accretion, the possible presence of inner holes, and therefore they likely absence of strong winds emanating from the innermost disk regions. The [Ne II] *disk* diagnostic may thus be optimized for the study of transitional disks, most of which are also not known to drive outflows or jets. Several of these have been well studied, including new ground-based observations of spectrally resolved [Ne II] lines (Najita et al., 2009). In this context, the [Ne II] line may develop its full diagnostic power to study disk ionization and heating by ionizing radiation from the central star, processes that are pivotal for disk dispersal through photoevaporation (Alexander et al., 2006; Ercolano et al., 2008a, 2009; Owen et al., 2010)in the first place.

High resolution and high signal-to-noise line profile can help assessing the origin of the line, with profiles centred at the stellar radial velocity being synonymous with a disk origin. This is true for all inclinations except those very close to edge on, where outflows would also produce profiles centered on the stellar radial velocity. Blue shifted profiles are expected to be observed for system with outflows observed at non edge on inclinations (e.g. Alexander (2008)), and have been recently oberved by Pascucci and M.Sterzik (2009) in the spectra of TW Hya, Sz 73, T Cha and CS Cha. Other examples of high resolution spectra where the line has been detected include TW Hya Herczeg et al. (2007); $\lambda/\Delta\lambda \sim 30000$), GM Aur and AA Tau (Najita et al. (2009); $\lambda/\Delta\lambda \sim 80000$). Here the observed lines are consistent with being centred at the stellar radial velocity, suggesting a circumstellar disk origin, although the poor signal-to-noise of some of these detections makes it hard to say with certainty. The lines are broad with a FWHM of respectively $\sim$ 21 (TW Hya), 70 (AA Tau) and 14 (GM Aur) km s^{-1}. The [Ne II] FWHM

of GM Aur can be produced by a disk of normal flaring power, however the large FWHM of AA Tau requires the emission region to be dominated by very small radii and therefore implies a small degree of flaring. We finally conclude that high resolution observations of the [Ne II] line in YSOs, able to resolve its profile, are needed if this line is to be used to extract useful information on disk structure (e.g. flaring) and evolutionary stage by (e.g.) the detection of outflows and photoevaporative winds by comparison with line profile models like those of Alexander (2008) or those presented in this work.

Conclusions

In the last 20 years observations were focused on the study of the circumstellar disks around young stars, mostly because they are believed to be the birthplace of planets. Those efforts are leading to huge amount of data that are revealing new insight on the structure and evolution of these object. Nowadays it is widely accepted the fundamental role they play in the star and the planet formation process. Circumstellar disk are needed to remove the angular momentum from the matter falling on the central object. While feeding the central star, dust and gas stockpile in the disk and undergo physical and chemical evolution. In such enviroment the gaseous and terrestrial planet forms.
Despite the large amount of data collected, most of the knowledge on the circumstellar disk comes from the modelling of their spectral energy distribution. Even if, widely used such approach suffers of strong limitation due to high degeneracy of the models as well has the high variability that often young stellar system shows.

Large samples of sources has to be modelled in attempt to determine mean disk properties. Such statistical studies, even if desirable have the drawback of missing eventually details in disk structure and evolution. This is extremely important in the case of objects with poor statistic, like the transitional disk believed to be in a phase of fast evolution that eventually bring to the dissipation of the disk. They are generally identified by the shape of the SED, presenting a lack of emission in the near/mid infrared respect typical disk, but with a step rise at longer wavelegths. Transitional disk, hence, are objects that have a lack/reduced/ amount of dust in the inner regions ≤ 10 AU. It is among these objects that the planet - forming systems can be found. So future progresses in planet formation theories need to a stronger constrains the physical properties of the disk, explanation of the transitional disk phenomena and development of new diagnostic, in particular for the inner disk. SED modelling is a wise guide to identify releavant candidates, however, they results covers large spread of values.

This work moves In this framework. From one side, the detailed study of new identified transitional disk help to shed light on such objects. In fact, from their definition, the appear to be a rather inhomogeneous class. Peculiar systems, like circumbinary disks, not linked to evolutionary effect have the same SED shape. Here, I present a detailed study on the transitional disk T Chamaelontis. Differently than most of the other disks, it shows signature of excess emission in the near-infrared, indicating that the dust in the inner region is not removed completely. In this work I not only confirmed the transitional nature of the system, but tried to rule out other possible explanation to the SED's shape (e.g. binarity). However, T Cha revealed to be peculiar also for its striking variability up to ~ 3 mag in V band. This is mostly due to the fact the disk is observed close to the edge-on. Nevertheless, too often in the study of the young stellar objects and their related disks, variability is often not considered, directing toward missleading results. T Cha is one of such cases. Even if it is not possible to draw robusts conclusions on the absence/presence of a close companion, the observations indicate that the disk host the presence of dusty clumps, that move in front of the line of sight, obscuring the central star. This is compatible with a complex phenomenology that see the system becoming redder, while fainting. At the same time, the extinction of the stellar continuum results in the circumstellar enviroment to stick out. Thus, typical lines of young stellar objects (Hα, Hβ, [O I], Ca II] infrared doublet appear in emission becoming strong during such occultation events. How the presence of these clumps is linked to the transitional shape is still under debate, however, the derived extinction law and the mid infrared spectrum point toward the presence of grain growth in the inner regions.

If the SED is still the main diagnostical tool to probe the dusty disk, the recent progress in infrared and submillimiter technology has allow a direct investigation of the disk gaseous component. Gas dominates the mass, thus the dynamic, of the disk, sets the structure and interact with the dust. For example, small grain feels the areodynamical lift of the gas in keplerian orbit and are dragged in the accretion process toward the disk inner edge, hence the evaporation. Presence of gas influence the formation of giant gaseous planets and/or induce planet migration. Moreover gas is an excellent tool to probe the physical and chemical condition in the protoplanetary disks. Unfortunately in doing so complex models are required and classical gas diagnostics, like OH, H_2, CO emission lines often probes the surface regions of the disks where the temperature is difficult to compute. In particular on these surface layers the gas thermally decouple from the dust, increasing

its temperature under the effect of the stellar radiation and eventual high-energy (UV/X-Ray) fields.

With the opening of new observative windows, in the mid/far infrared offered by space telescopes (like *Spitzer* and *Herschel*) and ground instruments, new diagnostics has been proposed. Among those the theoretical prevision and then detection of the atomic fine structure emission lines of [Ne II] is considered a success of both theory and observations. However, to fulfill their diagnostic potential, it has to be determined the heating and ionization process that lead to their formation. Despite more than $\sim$70 detection in young systems, there is still a strong debate, not only on where the lines form, but also which are the exciting sources. X-Rays and EUV are strong candidates if the lines forms in the *disk* atmosphere layers. However, in each one of those cases, infrared fine structure lines are useful diagnostics for different properties, local density and temperature in the first case, ionization flux in the second.

In this field I have modelled the [Ne II] emission line and the its spectral profile to be compared with future observations, assuming X-Ray irradiated disks. Most important I have checked the dependance of the emission strengh from disk and star parameters. This is a critical issue, since the observed fluxes ranges in a interval covering 3 order of magnitude. Güdel et al. (2000) shown that the L([Ne II]) is correlated with the X-ray emission of the star. Despite this, even taking into account of such correlation, for a fixed X-Ray , L_X, luminosity the data still spread over one order of magnitude. If the line should be used as a diagnostic, this spread have to be addressed. This work is the first attempt to explain such observational evidence. I found that, fixed all the other disk parameters, adopting models covering the typical range of flaring needed to fit the observation, the observed [Ne II] spread come naturally from the different amount of exciting radiation effectively hitting the disk. In another way, the presence of absorbing material between the X-Ray source and the disk alter the irradiating spectra and the disk structure, again showing a spread in L([Ne II) compatible wth the observation.

Despite those success, the mean flux level of the modelled line is still fainter than the observation. This inconsistence is probably due to the contribution from the photoevaporative flow not taken into account in the actual modelling. First indications from ground base observations indicate that the *Spitzer* observed fluxes, covering most of the observed samples, are about $\sim$ 3 times higher than the contribution coming from the disk. Such evidences are encouraging. At the same times, models are in continue evolution. Owen et al. (2010) has performed the first autoconsistent modelling of either the disk contribution and the photoevaporative flow, showing that effectively

the neon is produced mostly in gravitationally unbound region of the disk. If from one side such behaviour plays against the use of [Ne II] as disk physical properties diagnostic, from the other side strongly helps the study of the photoevaporative winds, that offer an actractive, but still debated, explanation to the disk dissipation on very fast scale. In both cases, new horizons are opening in the study of circumstellar disks and the connected planet formation.

Acknowledgments

Bibliography

R. Akeson, D. R. Ciardi, G. T. van Belle, et al. Infrared interferometric observations of young stellar objects. *Astrophysical Journal*, 543:313, 2000.

J. M. Alcalá, J.M. E. Covino, M. Franchini, J. Krautter, L. Terranegra, and R. Wichmann. T-chamaeleontis - a weak-line yy-orionis star. *Astronomy and Astrophysics*, 272:225, 1993.

J. M. Alcalá, J. Krautter, J. H. M. M. Schmitt, E. Covino, et al. A study of the chamaeleon star forming region from the rosat all-sky survey. i. x-ray observations and optical identifications. *Astronomy and Astrophysics Supplement*, 114:109, 1995.

J. M. Alcalá, L. Spezzi, A. Frasca, E. Covino, et al. The first brown dwarf with a disk in chamaeleon ii. *Astronomy and Astrophysics*, 453:1, 2006.

J. M. Alcalá, L. Spezzi, N. Chapman, N. J. Evans, et al. The spitzer c2d survey of large, nearby, interstellar clouds. x. the chamaeleon ii pre-main-sequence population as observed with irac and mips. *The Astrophysical Journal*, 676:427–463, 2008.

S. H. P. Alencar and C. Batalha. Variability of southern t tauri stars. ii. the spectral variability of the classical t tauri star tw hydrae. *Astrophysical Journal*, 571:378, 2002.

R. D. Alexander. [neii] emission-line profiles from photoevaporative disc winds. *Montly Notices of the Royal Astronomical Society*, 391:L64–68, 2008.

R. D. Alexander and P. J. Armitage. Dust dynamics during protoplanetary disc clearing. *Montly Notices of the Royal Astronomical Society*, 375:500, 2007.

R. D. Alexander, C. J. Clarke, and J. E. Pringle. The effects of x-ray photoionization and heating on the structure of circumstellar discs. *Montly Notices of the Royal Astronomical Society*, 354:71–80, 2004.

R. D. Alexander, C. J. Clarke, and J. E. Pringle. Photoevaporation of proto-planetary discs - ii. evolutionary models and observable properties. *Montly Notices of the Royal Astronomical Society*, 369(1):229–239, 2006.

I. Appenzeller and R. Mundt. T tauri stars. *Astronomy and Astrophysics Review*, 1:291–334, 1989.

P. J. Armitage. Lecture notes on the formation and early evolution of planetary systems. *ArXiv Astrophysics e-prints*, arXiv:astro-ph/0701485v2, 2009.

M. Asplund, N. Grevesse, and A. J. Sauval. The solar chemical composition. In Thomas G. Barnes III and Frank N. Bash, editors, *Cosmic Abundances as Records of Stellar Evolution and Nucleosynthesis*, volume 336, page 25. Astronomical Society of the Pacific, 2005.

S. A. Balbus and J. F. Hawley. A powerful local shear instability in weakly magnetized disks. i - linear analysis. ii - nonlinear evolution. *The Astrophysical Journal*, 376:214–233, 1991.

S. A. Balbus and J. F. Hawley. Instability, turbulence, and enhanced transport in accretion disks. *Reviews of Modern Physics*, 70(1):1–53, 1998.

S. V. W. Beckwith, A. I. Sargent, R. S. Chini, and R. Guesten. A survey for circumstellar disks around young stellar objects. *Astronomical Journal*, 99:924, 1990.

C. Bertout. Occultation of young stellar objects by circumstellar disks. i. theoretical expectations and preliminary comparison with observations. *Astronomy and Astrophysics*, 363:984, 2000.

C. Bertout, L. Siess, and S. Cabrit. The evolution of stars in the taurus-auriga t association. *Astronomy and Astrophysics*, 473L:21, 2007.

M. S. Bessel. Ubvri photometry. ii - the cousins vri system, its temperature and absolute flux calibration, and relevance for two-dimensional photometry. *Astronomical Society of the Pacific, Publications*, 91:589, 1979.

J. E. Bjorkman and K. Wood. Radiative equilibrium and temperature correction procedures for use in monte carlo radiation transfer. *American Astronomical Society*, 29:1227, 1997.

P. Bodenheimer and D. N. C. Lin. Implications of extrasolar planets for understanding planet formation. *Annual Review of Earth and Planetary Sciences*, 30:113–148, 2002.

P. Bodenheimer and J. B. Pollack. Calculations of the accretion and evolution of giant planets the effects of solid cores. *Icarus*, 57:391, 1986.

P. Bodenheimer, O. Hubicky, and J. J. Lissauer. Models of the in situ formation of detected extrasolar giant planets. *Icarus*, 143(2-14), 2000.

R. Van Boekel, M. Güdel, T. Henning, and F. Lahuis. An outflow origin of the [ne ii] emission in the t tauri triplet. *Astronomy and Astrophysics*, 497: 137–144, 2009.

A. P. Boss. Evolution of the solar nebula. iv. giant gaseous protoplanet formation. *Astrophysical Journal*, 503:923, 1998.

J. Bouvier, K. N. Grankin, S. H. P. Alencar, C. Dougados, et al. Eclipses by circumstellar material in the t tauri star aa tau. ii. evidence for non-stationary magnetospheric accretion. *Astronomy and Astrophysics*, 409: 169, 2003.

J. M. Brown, G. A. Blake, C. P. Dullemond, B. Merín, et al. Cold disks: Spitzer spectroscopy of disks around young stars with large gaps. *Astrophysical Journal*, 664:107, 2007.

J. S. Carr and J. R. Najita. Organic molecules and water in the planet formation region of young circumstellar disks. *Science*, 319(5869):1504, 2008.

E. I. Chiang and P. Goldreich. Spectral energy distributions of t tauri stars with passive circumstellar disks. *The Astrophysical Journal*, 490:368, 1997.

E. I. Chiang, M. K. Joung, M. J. Creech-Eakman, C. Qi, et al. Spectral energy distributions of passive t tauri and herbig ae disks: Grain mineralogy, parameter dependences, and comparison with infrared space observatory lws observations. *The Astrophysical Journal*, 547:1077, 2001.

L. Cieza, D. Padgett, K. R. Stapelfeldt, and J. C. Augereau. The spitzer c2d survey of weak-line t tauri stars. ii. new constraints on the timescale for planet building. *Astrophysical Journal*, 667:308, 2007.

L. A. Cieza. The evolution of primordial circumstellar disks. In A. Frebel, J. R. Maund, J. Shen, and M. H. Siegel, editors, *New Horizons in Astronomy*, volume 393 of *Astronomical Society of the Pacific Conference Series*, page 35, 2008.

C. J. Clarke, A. Gendrin, and M. Sotomayor. The dispersal of circumstellar discs: the role of the ultraviolet switch. *Montly Notices of the Royal Astronomical Society*, 328:485, 2001.

L. M. Close, A. Dutrey, F. Roddier, S. Guilloteau, et al. Adaptive optics imaging of the circumbinary disk around the t tauri binary uy aurigae: Estimates of the binary mass and circumbinary dust grain size distribution. *Astrophysical Journal*, 499:883, 1998.

E. Covino, L. Terranegra, M. Franchini, K. C. Chavarria, et al. Ubv(ri)c photometric monitoring of orion population stars in the southern hemisphere. *Astronomy and Astrophysics Supplement*, 94:273, 1992.

E. Covino, J. M. Alcalá, J. Krautter, L. Terranegra, et al. Variable photometry of young stars. In S. V. W. Beckwith, J. Staude, A. Quetz, and A. Natta, editors, *Disks and Outflows Around Young Stars*, volume 465, page 343, 1996.

E. Covino, J. M. Alcalá, S. Allain, J. Bouvier, et al. A study of the chamaeleon star-forming region from the rosat all-sky survey. iii. high resolution spectroscopic study. *Astronomy and Astrophysics*, 328:187, 1997.

P. D'Alessio. Disks around classical t tauri stars. *Revista Mexicana de Astronomía y Astrofísica*, 18:14–20, 2003.

P. D'Alessio, J. Canto, N. Calvet, and S. Lizano. Accretion disks around young objects. i. the detailed vertical structure. *The Astrophysical Journal*, 500:411, 1998.

T. H. Dall, N. C. Santos, T. Arentoft, T. R. Bedding, et al. Bisectors of the cross-correlation function applied to stellar spectra. discriminating stellar activity, oscillations and planets. *Astronomy and Astrophysics*, 454:341, 2006.

M. E. Van den Ancker, P. R. Wesselius, A. G. G. M. Tielens, E. F. van Dishoeck, et al. Iso spectroscopy of shocked gas in the vicinity of t tauri. *Astronomy and Astrophysics*, 348:877–887, 1999.

D.Hollenbach and U. Gorti. Diagnostic line emission from extreme ultraviolet and x-ray-illuminated disks and shocks around low-mass stars. *The Astrophysical Journal*, 703(2):1203–1223, 2009.

Draine. Perspectives on interstellar dust inside and outside of the heliosphere. *Space Science Reviews*, 143:333–345, 2009.

B. T. Draine. Interstellar dust grains. *Annual Review of Astronomy and Astrophysics*, 41:241, 2003.

C. P. Dullemond and C. Dominik. Dust coagulation in protoplanetary disks: A rapid depletion of small grains. *Astronomy and Astrophysics*, 434:971, 2005.

C. P. Dullemond, C. Dominik, and A. Natta. Passive irradiated circumstellar disks with an inner hole. *The Astrophysical Journal*, 560:957–969, 2001.

C. P. Dullemond, M. E. Van den Ancker, B. Acke, and R. Van Boekel. Explaining ux orionis star variability with self-shadowed disks. *Astrophysical Journal*, 588:360, 2003.

C. P. Dullemond, D. Hollenbach, I. Kamp, and P. D'Alessio. Models of the structure and evolution of protoplanetary disks. In B. Reipurth, D. Jewitt, and K. Keil (eds.), editors, *Protostars and Planets V*, pages 555–572. University of Arizona Press: Tucson, 2007.

B. Ercolano, J. J. Drake, J. C. Raymond, and C. C. Clarke. X-ray-irradiated protoplanetary disk atmospheres. i. predicted emission-line spectrum and photoevaporation. *The Astrophysical Journal*, 688:398–407, 2008a.

B. Ercolano, P. R. Young, J. J. Drake, and J. C. Raymond. X-ray enabled mocassin: A three-dimensional code for photoionized media. *The Astrophysical Journal Supplement Series*, 175(2):534–542, 2008b.

B. Ercolano, C. C. Clarke, and J. J. Drake. X-ray irradiated protoplanetary disk atmospheres. ii. predictions from models in hydrostatic equilibrium. *The Astrophysical Journal*, 699:1639–1649, 2009.

C. Espaillat, N. Calvet, P. D'Alessio, E. Bergin, et al. Probing the dust and gas in the transitional disk of cs cha with spitzer. *The Astrophysical Journal*, 664(2):L111–114, 2007.

C. Espaillat, N. Calvet, K. L. Luhman, J. Muzerolle, and other. Confirmation of a gapped primordial disk around lkca 15. *Astrophysical Journal*, 682: L125, 2008.

M. Esposito, E. Covino, J. M. Alcalá, E. Guenther, et al. Mo lup: a hierarchical triple t tauri system. *Montly Notices of the Royal Astronomical Society*, 376:1805, 2007.

E. D. Feigelson, K. Getman, L. Townsley, G. Garmire, et al. Global x-ray properties of the orion nebula region. *The Astrophysical Journal Supplement Series*, 160:379–389, 2005.

M. Franchini, E. Covino, R. Stalio, L. Terranegra, et al. A high-resolution spectroscopic study of southern t tauri stars. *Astronomy and Astrophysics*, 256:525, 1992.

S. Frink, S. Roeser, J. M. Alcalá, E. Covino, et al. Kinematics of t tauri stars in chamaeleon. *Astronomy and Astrophysics*, 338:442, 1998.

S. Fromang, S. A. Balbus, and J. P. de Villiers. Evolution of self-gravitating magnetized disks. i. axisymmetric simulations. *Astrophysical Journal*, 616: 357–363, 2004.

E. Furlan, N. Calvet, P. D'Alessio, L. Hartmann, et al. Colors of classical t tauri stars in taurus derived from spitzer infrared spectrograph spectra: Indication of dust settling. *The Astrophysical Journal*, 628:L65–L68, 2005.

E. Furlan, L. Hartmann, N. Calvet, P. D'Alessio, et al. A survey and analysis of spitzer infrared spectrograph spectra of t tauri stars in taurus. *The Astrophysical Journal Supplement Series*, 165:568, 2006.

E. Furlan, D. B. Watson, et al. Disk evolution in the three nearby star-forming regions of taurus, chamaeleon and ophiuchus. In *Bulletin of the American Astronomical Society*, volume 38 of *Bulletin of the American Astronomical Society*, page 812, 2007.

G. F. Gahm, C. Fischerstrom, K. P Lindroos, and R. Liseau. Long- and short-term variability of the t tauri star ry lupi. *Astronomy and Astrophysics*, 211:115, 1989.

C. F. Gammie. Layered accretion in t tauri disks. *The Astrophysical Journal*, 457:355, 1996.

D. Gandolfi, J. M. Alcalá, S. Leccia, et al. The star formation in the l1615/l1616 cometary cloud. *Astrophysical Journal*, 687:1303, 2008.

V. C. Geers, J. C. Augereau, K. M. Pontoppidan, et al. C2d spitzer-irs spectra of disks around t tauri stars. ii. pah emission features. *Astronomy and Astrophysics*, 459:545, 2006.

A. E. Glassgold and J. R. Najita. The effects of x-rays on the diffuse gas in protoplanetary disks. In R. Jayawardhana & T. Greene, editor, *Young*

Stars Near Earth: Progress and Prospects, volume 244 of *Astronomical Society of the Pacific Conference Series*, page 251, 2001.

A. E. Glassgold, J. Najita, and J. Igea. Heating protoplanetary disk atmospheres. *The Astrophysical Journal*, 615:972–990, 2004.

A. E. Glassgold, J. R. Najita, and J. Igea. Neon fine-structure line emission by x-ray irradiated protoplanetary disks. *The Astrophysical Journal*, 656: 515–523, 2007.

U. Gorti and D. Hollenbach. Models of chemistry, thermal balance, and infrared spectra from intermediate-aged disks around g and k stars. *The Astrophysical Journal*, 613:424–447, 2004.

U. Gorti and D. Hollenbach. Line emission from gas in optically thick dust disks around young stars. *The Astrophysical Journal*, 683:287–303, 2008.

U. Gorti and D. Hollenbach. hotoevaporation of circumstellar disks by far-ultraviolet, extreme-ultraviolet and x-ray radiation from the central star. *The Astrophysical Journal*, 690(2):1539–1552, 2009.

C. A. Grady, E. F. Polomsky, Th. Henning, B. Stecklum, et al. The disk and environment of the herbig be star hd 100546. *Astronomical Journal*, 122: 3396, 2001.

A. Gras-Velazques and T. P. Ray. Weak-line t tauri stars: circumstellar disks and companions. i. spectral energy distributions and infrared excesses. *Astronomy and Astrophysics*, 443:541, 2005.

T. Greene. Protostars. *American Scientist*, 89:316, 2001.

J. Gregorio-Hetem, J. R. D. Lepine, G. R. Quast C. A. O. Torres, et al. A search for t tauri stars based on the iras point source catalog. *Astronomical Journal*, 103:549, 1992.

N. Grevesse and A. J. Sauval. Standard solar composition. *Space Science Reviews*, 85:161–174, 1998.

V. P. Grinin. The origin of the blue emission observed in the deep minima of young irregular variable stars. *Pis'ma v Astronomicheskii Zhurnal*, 14: 65, 1988.

M. Güdel, K. R. Briggs, K. Arzner, M. Audard, et al. The xmm-newton extended survey of the taurus molecular cloud (xest). *Astronomy and Astrophysics*, 468:353–377, 2007.

M. Güdel, R. Van Boekel, F. Lahius, J. Najita, et al. 5th spitzer conference, new light on young stars, 2009. URL `http://www.ipac.caltech.edu/spitzer2008/talks/ManuelGuedel.html`.

M. Güdel, F.Lahuis, K. R. Briggs, J. Carr, et al. On the origin of [neii] 12.81 μm emission from pre-main sequence stars: Disks, jets, and accretion. *Astronomy and Astrophysics*, 519:A113, 2010.

E. W. Guenther, M. Esposito, R. Mundt, E. Covino, et al. Pre-main sequence spectroscopic binaries suitable for vlti observations. *Astronomy and Astrophysics*, 467:1147, 2007.

K. E. Haisch, E. A. Lada, and C. J. Lada. Circumstellar disks in the ic 348 cluster. *Astronomical Journal*, 121:2065, 2001.

P. Hartigan, L. Hartmann, S. Kenyon, R. Hewett, et al. How to unveil a t tauri star. *The Astrophysical Journal Supplement Series*, 70:899–914, 1989.

P. Hartigan, S. Edwards, and L. Ghandour. Disk accretion and mass loss from young stars. *Astrophysical Journal*, 452:736, 1995.

L. Hartmann. *Accretion Processes in Star Formation*. Cambridge Astrophysical Series. Cambridge University Press, 2009.

L. Hartmann, N. Calvet, E. Gullbring, and P. D'Alessio. Accretion and the evolutiion of t tauri disks. *The Astrophysical Journal*, 495:385, 1998.

C. Hayashi. Structure of the solar nebula, growth and decay of magnetic fields and effects of magnetic and turbulent viscosities on the nebula. *Progress of Theoretical Physics Supplement*, 70:35–53, 1981.

T. Henning, W. Pfau, H. Zinnecker, and T. Prousti. A 1.3-millimeter survey of circumstellar dust around young chamaeleon objects. *Astronomy and Astrophysics*, 346:205, 1993.

W. Herbst and V. S. Shevchenko. A photometric catalog of herbig ae/be stars and discussion of the nature and cause of the variations of ux orionis stars. *Astronomical Journal*, 118:1043–1060, 1999.

W. Herbst, D. K. Herbst, E. J. Grossman, and D. Weinstein. Catalogue of ubvri photometry of t tauri stars and analysis of the causes of their variability. *Astronomical Journal*, 108:1906, 1994.

G. J. Herczeg, J. L. Linsky, J. A. Valenti, C. M. Johns-Krull, et al. The far-ultraviolet spectrum of tw hydrae. i. observations of h2 fluorescence. *The Astrophysical Journal*, 572(310-325), 2002.

G. J. Herczeg, F. M. Walter, J. L. Linsky, G. F. Gahm, et al. The loopy ultraviolet line profiles of ru lupi: Accretion, outflows, and fluorescence. *The Astronomical Journal*, 129(6):2777–2791, 2005.

G. J. Herczeg, J. R. Najita, L. A. Hillenbrand, and I. Pascucci. High-resolution spectroscopy of [ne ii] emission from tw hydrae. *The Astrophysical Journal*, 670:509–515, 2007.

J. Hernández, N. Calvet, C. Briceno, L. Hartmann, et al. Spitzer observations of the orion ob1 association: Disk census in the low-mass stars. *Astrophysical Journal*, 671:1784, 2007.

G. A. Hirth, R. Mundt, J. Solf, and Th. P. Ray. Asymmetries in bipolar jets from young stars. *Astrophysical Journal*, 427:99, 1994.

C. Hoffmeister. Ueber das verhalten von drei typischen und sechs atypischen rw aurigae- sterne. *Veroeffentlichungen der Sternwarte Sonneberg*, 3:340–416, 1958.

D. Hollenbach and U. Gorti. Gas heating, chemistry, and infrared spectra in intermediate-aged disks around low mass stars. In G. Garcia-Segura, G. Tenorio-Tagle, J. Franco, and H. W. Yorke, editors, *Revista Mexicana de Astronomia y Astrofisica Conference Series*, volume 22 of *Revista Mexicana de Astronomia y Astrofisica Conference Series*, pages 33–37, 2004.

D. J. Hollenbach, H. W. Yorke, and D. Johnstone. Disk dispersal around young stars. In V. Mannings, A. P. Boss, and S. S. Russell, editors, *Protostars and Planets IV*, page 401, 2000.

N. J. Evans II, M. M. Dunham, J. K. Jørgensen, M. L. Enoch, et al. The spitzer c2d legacy results: Star-formation rates and efficiencies; evolution and lifetimes. *The Astrophysical Journal Supplement Series*, 181(2):321–350, 2009.

M. J. Ireland and A .L. Kraus. The disk around coku tauri/4: Circumbinary, not transitional. *Astrophysical Journal*, 678:59, 2008.

A. Isella, L. Testi, and A. Natta. Large dust grains in the inner region of circumstellar disks. *Astronomy and Astrophysics*, 451:951, 2006.

C. M. Johns and G. Basri. The line profile variability of su aurigae. *Astronomical Journal*, 109:2008, 1995.

B. Jonkheid, F. G. A. Fass, G. J. van Zadelhoff, and E. F. van Dishoeck. The gas temperature in flaring disks around pre-main sequence stars. *Astronomy and Astrophysics*, 428:511–521, 2004.

I. Kamp and F. Sammar. Modeling the gas reservoir of circumstellar disks around young g-type stars. *Astronomy and Astrophysics*, 427:561–566, 2004.

I. Kamp and G. J. van Zadelhoff. On the gas temperature in circumstellar disks around a stars. *Astronomy and Astrophysics*, 373:641–656, 2001.

V. Kashyap and J. J. Drake. Pintofale : Package for the interactive analysis of line emission. *Bulletin of the Astronomical Society of India*, 28:475–476, 2000.

S. J. Kenyon and L. Hartmann. Spectral energy distributions of t tauri stars - disk flaring and limits on accretion. *The Astrophysical Journal*, 323: 714–733, 1987.

S. J. Kenyon and L. Hartmann. Pre-main-sequence evolution in the taurus-auriga molecular cloud. *The Astrophysical Journal Supplement Series*, 101: 117, 1995.

Y. Kitamura, M. Momose, S. Yokogawa, R. Kawabe, M. Tamura, and S. Ida. Investigation of the physical properties of protoplanetary disks around t tauri stars by a 1 arcsecond imaging survey: Evolution and diversity of the disks in their accretion stage. *The Astrophysical Journal*, 581:357–380, 2002.

R. Köhler. Multiplicity of x-ray-selected t tauri stars in chamaeleon. *Astronomical Journal*, 122:3325, 2001.

J. Kominami and S. Ida. The effect of dissipating gas disk on terrestrial planet formation. In *Bulletin of the American Astronomical Society*, volume 34, page 941, 2002.

S. Kraus, K. H. Hoffmann, M. Benisty, et al. Revealing the sub-au asymmetries of the inner dust rim in the disk around the herbig ae star r coronae austrinae. *Astronomy and Astrophysics*, 508:787, 2008.

M. J. Kuchner. A minimum-mass extrasolar nebula. *The Astrophysical Journal*, 612:1147–1151, 2004.

C. J. Lada. Star formation - from ob associations to protostars. In M. Peimbert and J. Jugaku, editors, *Star Forming Regions*, volume 115, pages 1–17, 1987.

C. J. Lada, A. A. Muench, K. L. Luhman, L. Allen, et al. Spitzer observations of ic 348: The disk population at 2-3 million years. *Astronomical Journal*, 131:1574, 2006.

F. Lahuis, E. F. van Dishoeck, A. C. A. Boogert, et al. Hot organic molecules toward a young low-mass star: A look at inner disk chemistry. *The Astrophysical Journal*, 636:L145, 2006.

F. Lahuis, E. F. van Dishoeck, G. A. Blake, N. J. Evans, et al. c2d spitzer irs spectra of disks around t tauri stars. iii. [ne ii], [fe i], and h2 gas-phase lines. *The Astrophysical Journal*, 665:492–511, 2007.

E. Landi and K. K. H. Phillips. Chianti-an atomic database for emission lines. viii. comparison with solar flare spectra from the solar maximum mission flat crystal spectrometer. *The Astrophysical Journal Supplement Series*, 166:421–440, 2006.

A. Laor and B. T. Draine. Spectroscopic constraints on the properties of dust in active galactic nuclei. *Astrophysical Journal*, 402:441, 1993.

D. Lommen, C. M. Wright, S. T. Madison, and J. K. Jørgensen. nvestigating grain growth in disks around southern t tauri stars at millimetre wavelengths. *Astronomy and Astrophysics*, 462:211–220, 2007.

D. Lynden-Bell and J. E. Pringle. The evolution of viscous discs and the origin of the nebular variables. *Montly Notices of the Royal Astronomical Society*, 168:603–637, 1974.

V. Mannings, D. W. Koerner, and A. I. Sargent. A rotating disk of gas and dust around a young counterpart to Îš pictoris. *Nature*, 388:555, 1997.

T. Matsuo, H. Shibai, and T. Ootsubo. Planetary formation scenarios revisited: Core-accretion versus disk instability. *Astrophysical Journal*, 662:1282–1292, 2007.

H. Mauder and F. M. Sosna. Light changes of t tauri stars in the chamaeleon association. *Information Bulletin on Variable Stars*, 1:1049, 1975.

P. Mazzotta, G. Mazzitelli, S. Colafrancesco, and N. Vittorio. Ionization balance for optically thin plasmas: Rate coefficients for all atoms and ions

of the elements h to ni. *Astronomy and Astrophysics Supplement*, 133: 403–409, 1998.

R. Meijerink, A. E. Glassgold, and J. R. Najita. Atomic diagnostics of x-ray-irradiated protoplanetary disks. *The Astrophysical Journal*, 676:518–531, 2008.

F. Menard, K. Stapelfeldt, J. Krist, G. Duvert, et al. The circumbinary disk of uy aurigae: Combining hubble space telescope and adaptive optics images. In *Bulletin of the American Astronomical Society*, volume 31 of *Bulletin of the American Astronomical Society*, page 933, 1999.

B. Merín, J. K. Jørgensen, L. Spezzi, J. M. Alcalá, et al. The spitzer c2d survey of large, nearby, interstellar clouds. xi. lupus observed with irac and mips. *The Astrophysical Journal Supplement Series*, 177:551, 2008.

R. Millan-Gabet, F. Malbet, R. Akeson, C. Leinert, et al. The circumstellar environments of young stars at au scales. In B. Reipurth, D. Jewitt, and K. Keil (eds.), editors, *Protostars and Planets V*, pages 539–554, 2007.

M. Morel and P. Magnenat. Ubvrijklmnh photoelectric photometric catalogue. *Astronomy and Astrophysics Supplement*, 34:477, 1978.

J. Najita, J. S. Carr, and R. D. Mathieu. Gas in the terrestrial planet region of disks: Co fundamental emission from t tauri stars. *The Astrophysical Journal*, 589:931–952, 2003.

J. R. Najita, S. Edwards, G. Barsi, and J. Carr. Spectroscopy of inner protoplanetary disks and the star-disk interface. In V. Mannings, A. P. Boss, and S. S. Russell, editors, *Protostars and Planets IV*, page 457. University of Arizona Press: Tucson, 2000.

J. R. Najita, J. S. Carr, A. E. Glassgold, and J. A. Valenti. Gaseous inner disks. In B. Reipurth, D. Jewitt, and K. Keil (eds.), editors, *Protostars and Planets V*, volume 951, pages 507–522. University of Arizona Press: Tucson, 2007a.

J. R. Najita, E. S. Stephen, and J. Muzerolle. Demographics of transition objects. *Montly Notices of the Royal Astronomical Society*, 378:369, 2007b.

J. R. Najita, G. W. Doppmann, M. A. Bitner, M. J. Ritcher, et al. High-resolution spectroscopy of [ne ii] emission from aa tau and gm aur. *The Astrophysical Journal*, 697:957–963, 2009.

A. Natta, V. Grinin, and V. Mannings. Properties and evolution of disks around pre-main-sequence stars of intermediate mass. In V. Mannings, A. P. Boss, and S. S. Russell, editors, *Protostars and Planets IV*, page 559, 2000.

A. Natta, T. Prousti, R. Neri, et al. A reconsideration of disk properties in herbig ae stars. *Astronomy and Astrophysics*, 371:186, 2001.

A. Natta, L. Testi, J. Muzerolle, S. Randich, et al. Accretion in brown dwarfs: An infrared view. *Astronomy and Astrophysics*, 424:603, 2004.

H. Nomura and T. J. Millar. Molecular hydrogen emission from protoplanetary disks. *Astronomy and Astrophysics*, 438:923–928, 2005.

B. Nordström, M. Mayor, J. Andersen, et al. The geneva-copenhagen survey of the solar neighbourhood. ages, metallicities, and kinematic properties of 14 000 f and g dwarfs. *Astronomy and Astrophysics*, 418:989, 2004.

J. Owen, B. Ercolano, C. C. Clarke, and R. D. Alexander. Radiation-hydrodynamic models of x-ray and euv photoevaporating protoplanetary discs. *Montly Notices of the Royal Astronomical Society*, 401(3):1415–1428, 2010.

F. Palla and S. W. Stahler. Star formation in the orion nebula cluster. *Astrophysical Journal*, 525:772, 1999.

J. C. B. Papaloizou and D. N. C. Lin. Theory of accretion disks i: Angular momentum transport processes. *Annual review of astronomy and astrophysics*, 33:505, 1995.

I. Pascucci and M.Sterzik. Evidence for disk photoevaporation driven by the central star. *The Astrophysical Journal*, 702:724–732, 2009.

I. Pascucci, D. Apai, T. Henning, and C. P. Dullemond. The first detailed look at a brown dwarf disk. *The Astrophysical Journal*, 590:L111–114, 2003.

I. Pascucci, D. Hollenbach, J. R. Najita, J. Muzerolle, et al. Detection of [ne ii] emission from young circumstellar disks. *The Astrophysical Journal*, 663:383–393, 2007.

Y. V. Pavlenko and A. Magazzú. Theoretical lte and non-lte curves of growth for lii lines in g-m dwarfs and subgiants. *Astronomy and Astrophysics*, 311: 961, 1996.

J. B. Pollack, O. Hubickyj, P. Bodenheimer, J. J. Lissauer, et al. Formation of the giant planets by concurrent accretion of solids and gas. *Icarus*, 124: 62–85, 1996.

T. Preibisch, M. J. McCaughrean, N. Grosso, E. D. Feigelson, et al. X-ray emission from young brown dwarfs in the orion nebula cluster. *The Astrophysical Journal Supplement Series,*, 160:582–593, 2005.

J. E. Pringle. Accretion discs in astrophysics. *Annual review of astronomy and astrophysics*, 19:137–162, 1981.

D. Queloz, G. W. Henry, J. P. Sivan, et al. No planet for hd 166435. *Astronomy and Astrophysics*, 379:279, 2001.

T. P. Robitaille, B. A. Whitney, R. Indebetouw, K. Wood, and P. Denzmore. Interpreting spectral energy distributions from young stellar objects. i. a grid of 200,000 yso model seds. *The Astrophysical Journal Supplement Series*, 167:256–285, 2006.

T. P. .Robitaille, B. A. Whitney, R. Indebetouw, and K. Wood. Interpreting spectral energy distributions from young stellar objects. ii. fitting observed seds using a large grid of precomputed models. *The Astrophysical Journal Supplement Series*, 169:328, 2007.

B. Rodgers, D. H. Wooden, V. Grinin, Shakhovsky, et al. Spectroscopic variability of the uxor star rr tauri. *Astrophysical Journal*, 564:405, 2002.

C. Salyk, K. M. Pontoppidan, G. A. Blake, F. Lahius, et al. H2o and oh gas in the terrestrial planet-forming zones of protoplanetary disks. *The Astrophysical Journal*, 676:L49–52, 2008.

N. C. Santos, M. Mayor, D. Naef, et al. The coralie survey for southern extra-solar planets. ix. a 1.3-day period brown dwarf disguised as a planet. *Astronomy and Astrophysics*, 392:215, 2002.

J. Sanz-Forcada, N. S. Brickhouse, and A. K. Dupree. Quiescent and flaring structure in rs canum venaticorum stars. *The Astrophysical Journal*, 570: 799–819, 2002.

B. D. Savage and K. R. Sembach. Interstellar gas-phase abundances and physical conditions toward two distant high-latitude halo stars. *The Astrophysical Journal*, 470:893, 1996.

J. D. Scargle. Studies in astronomical time series analysis. ii - statistical aspects of spectral analysis of unevenly spaced data. *Astrophysical Journal*, 263:835, 1982.

G. Schneider, B. A. Smith, E. E. Becklin, D. W. Koerner, et al. Nicmos imaging of the hr 4796a circumstellar disk. *Astrophysical Journal*, 513: 127, 1999.

G. Schneider, A. S. Cotera, M. D. Silverstone, and A. j. Weinberger. Hst imaging of circumstellar disks. In L. Caroff, L. J. Moon, D. Backman, and E. Praton, editors, *Debris Disks and the Formation of Planets*, Astronomical Society of the Pacific Conference Series, page 247, 2004.

D. Semenov, D. Wiebe, and T. Henning. Reduction of chemical networks. ii. analysis of the fractional ionisation in protoplanetary discs. *Astronomy and Astrophysics*, 417:93–106, 2004.

N. I. Shakura and R. A. Sunyaev. Black holes in binary systems. observational appearance. *Astronomy and Astrophysics*, 24:337, 1973.

A. Sicilia-Aguilar, L. Hartmann, D. Watson, C. Bohac, et al. Silicate dust in evolved protoplanetary disks: Growth, sedimentation, and accretion. *Astrophysical Journal*, 659:1637, 2007.

B. Steltzer, M. Fernández, V. M. Costa, et al. The weak-line t tauri star v410 tau. i. a multi-wavelength study of variability. *Astronomy and Astrophysics*, 411:517, 2003.

A. Telleschi, M. Güdel, K. R. Briggs, M. Audard, and L. Scelsi. High-resolution x-ray spectroscopy of t tauri stars in the taurus-auriga complex. *Astronomy and Astrophysics*, 468:443–462, 2007.

L. Terranegra, F. Morale, A. Spagna, G. Massone, et al. Proper motions of faint rosat wtt stars in the chamaeleon region. *Astronomy and Astrophysics*, 341:L79, 1999.

C. G. Toner and D. F. Gray. The starpatch on the g8 dwarf xi bootis a. *Astrophysical Journal*, 334:1008, 1988.

P. G. Tuthill, J. D. Monnier, and W. C. Dandi. A dusty torus around the luminous young star lkhÎś101. *Nature*, 409:1012, 2001.

D. Vinković and T. Jurkić. Relation between the luminosity of young stellar objects and their circumstellar environment. *Astrophysical Journal*, 658: 462, 2007.

W. R. Ward. Survival of planetary systems. *The Astrophysical Journal Letters*, 482:L211, 1997.

J. C. Weingartner and B. T. Draine. Dust grain-size distributions and extinction in the milky way, large magellanic cloud, and small magellanic cloud. *The Astrophysical Journal*, 548:296–309, 2001.

R. J. White and G. Basri. Very low mass stars and brown dwarfs in taurus-auriga. *Astrophysical Journal*, 582:1109, 2003.

B. A. Whitney, K. Wood, J. E. Bjorkman, and M. Cohen. Two-dimensional radiative transfer in protostellar envelopes. ii. an evolutionary sequence. *The Astrophysical Journal*, 598:1079–1099, 2003a.

B. A. Whitney, K. Wood, J. E. Bjorkman, and M. J. Wolff. Two-dimensional radiative transfer in protostellar envelopes. i. effects of geometry on class i sources. *The Astrophysical Journal*, 591:1049–1063, 2003b.

B. A. Whitney, R. Indebetouw, J. E. Bjorkman, and K. Wood. Two-dimensional radiative transfer in protostellar envelopes. iii. effects of stellar temperature. *The Astrophysical Journal*, 617:1177–1190, 2004.

M. Wolk, E. P. Armstrong, and E. L. Mann. A search for protoplanetary disks around naked t tauri stars. *Astronomical Journal*, 111:2066, 1996.

D. K. Yeomans, P. G. Antreasian, J. P. Parrot, et al. Estimating the mass of asteroid 253 mathilde from tracking data during the near flyby. *Science*, 289:2085, 1997.

H. W. Yorke and P. Bodenheimer. The formation of protostellar disks. iii. the influence of gravitationally induced angular momentum transport on disk structure and appearance. *Astrophysical Journal*, 525:330–342, 1999.

A. N. Youdin and F. H. Shu. Planetesimal formation by gravitational instability. *The Astrophysical Journal*, 580:494–505, 2002.

B. Zuckerman, T. Forveille, and J. H. Kastner. Inhibition of giant-planet formation by rapid gas depletion around young stars. *Nature*, 373(6514): 494–496, 1995.